OPTIMAL DECODING OF PSK AND QAM SIGNALS IN FREQUENCY NONSELECTIVE FADING CHANNELS

by

DIMITRIOS P. BOURAS

Diploma of Electrical Engineering, University of Patras, Patras, Greece, 1989

A THESIS SUBMITTED IN PARTIAL FULFILLMENT OF

THE REQUIREMENTS FOR THE DEGREE OF

MASTER OF APPLIED SCIENCE

in

THE FACULTY OF GRADUATE STUDIES

DEPARTMENT OF ELECTRICAL ENGINEERING

We accept this thesis as conforming

to the required standard

The UNIVERSITY OF BRITISH COLUMBIA

September 1991

In presenting this thesis in partial fulfilment of the requirements for an advanced degree at the University of British Columbia, I agree that the Library shall make it freely available for reference and study. I further agree that permission for extensive copying of this thesis for scholarly purposes may be granted by the head of my department or by his or her representatives. It is understood that copying or publication of this thesis for financial gain shall not be allowed without my written permission.

Department of Electrical Engineering.

The University of British Columbia
Vancouver, Canada

Date Oct 11th, 1991

Abstract

In this thesis, the maximum likelihood sequential decoder for the reception of coded digitally modulated signals with single or multiamplitude constellations transmitted over a multiplicative, frequency nonselective fading (Rayleigh or Rician) channel and corrupted by additive white Gaussian noise (AWGN), is derived. It is shown that its structure consists of a *combination of envelope, multiple differential*[1] and *coherent* detectors. The outputs of each of these detectors are jointly processed by means of an algorithm which is presented in a recursive form. The derivation of this new receiver is general enough to accommodate uncoded as well as trellis coded Phase Shift Keying (PSK) and Quadrature Amplitude Modulated (QAM) schemes. Differentially encoded signals, such as the $\pi/4$-shift DQPSK scheme which has been selected as the new transmission standard for the emerging all-digital North American and Japanese cellular system, can be also incorporated. Furthermore, there is no assumption made on the power spectral density (or equivalently on the autocorrelation function) of the fading process, although it is considered to be known to the receiver. In order to reduce the overall receiver implementation complexity, several reduced complexity, near optimal versions of the algorithm are presented. These reduced complexity receivers are based on the use of only few multiple differential detectors. Performance evaluation results for reduced complexity trellis coded $\pi/4$-shift DQPSK and $\pi/4$-shift 8-DQAM systems have demonstrated that the proposed receivers dramatically reduce the error floor occurring due to fading. For example, for the $\pi/4$-shift DQPSK scheme operated in a fast (B_FT=0.125) Rayleigh flat-fading channel at a Signal-to-Noise ratio (SNR) of about 25 dB, the new reduced complexity receiver structures result in a bit error rate (BER) reduction of more than three orders of magnitude as compared to a conventional Viterbi receiver. For a slower fading channel, these gains are even higher. What is even more interesting, though, is that this performance was achieved by employing only up to third order multiple

[1] As it will be explained later on, a k^{th} order multiple differential detector is a differential detector employing a k^{th} symbol delay element.

differential detectors, thus maintaining reasonable levels of implementation complexity. By further increasing the order of the employed multiple differential detectors, the obtained BER performance improvements were found to be minimal.

To verify experimentally the effectiveness of the proposed receivers and to gain additional insight into some of the real-life implementation problems involved, we designed and realized in hardware a prototype $\pi/4$-shift DQPSK modem. Although its transmitter was designed with off the shelf digital TTL chips, linear analog devices and RF modules, its receiver was implemented by means of a TMS320C30 Digital Signal Processor. Employing this "flexible" receiver, the proposed algorithms could be evaluated very efficiently. The various experimental BER results obtained were in excellent agreement with the equivalent results obtained by means of computer simulation.

Motivated by these very encouraging experimental performance results, it is believed that LSI/VLSI implementation of such a $\pi/4$-shift DQPSK modem would be a very worthwhile task.

Contents

List of Figures

List of Tables

Acknowledgments

I would like to thank my parents, Panos and Toula, for their continuous moral support and constant encouragement. Dr. Vassilios Makios of the University of Patras, Patras Greece, for his positive influence regarding my post-graduate studies abroad. My supervisor, Dr. P. Takis Mathiopoulos, for providing continuous encouragement, moral support and valuable experience throughout this thesis project. Dimitrios Makrakis of the Communications Research Centre, Department of Communications, Government of Canada, for his valuable help and insightful discussions on algorithmic modelling. Finally, I would like to acknowledge the financial assistance provided by NSERC, in the form of operating grant OGPIN 011.

1. Introduction

1.1. The Multipath Fading Environment

It is only well known to all involved with mobile communications, that the major disturbance in the transmission of signals over land-mobile and mobile-satellite links, is the presence of multipath fading (see for example [1–5]).

Since propagation at VHF/UHF frequencies takes place through scattered and/or reflected waves, for a mobile user the fading effect is produced by a multitude of signals arriving at the receiver's antenna through multiple, random propagation paths which vary according to the user's velocity. As a result, the received signal will be characterized by severe envelope fluctuations as well as randomly changing phase shifts [5]. Collectively, the above phenomena create a diffused signal which is referred to as multipath fading (or in short fading). Naturally, the channels in which these phenomena take place are known as multipath fading channels, or in short, fading channels. Depending upon whether or not there is a line-of-sight (LOS) direct path between the transmitter and the mobile receiver, fading channels can have Rayleigh or Ricean characteristics [6].

For the Rayleigh fading channel, in which such a path does not exist, the probability density function (pdf) of the faded envelope r, follows the Rayleigh distribution, i.e.,

$$f(r) = \begin{cases} \frac{r}{\sigma^2} e^{-\frac{r^2}{2\sigma^2}}, & r > 0 \\ 0 & \text{elsewhere} \end{cases} \tag{1.1}$$

whereas its phase θ is uniformly distributed, i.e.,

$$f(\theta) = \begin{cases} \frac{1}{2\pi}, & -\pi \leq \theta < \pi \\ 0 & \text{elsewhere}. \end{cases} \tag{1.2}$$

On the other hand, for the Ricean fading channel, in addition to the diffused signal (Rayleigh fading), there is a direct LOS path. The vector sum of the direct signal with a Rayleigh fading

component results in a composite signal with Ricean statistics. The pdf of the envelope of such a signal is given as [7]

$$f(r) = 2r\sqrt{\frac{(1+K)}{S}}\exp\left[-K-(1+K)r^2\right]I_0\left[2r\sqrt{K(1+K)}\right] \tag{1.3}$$

where K denotes the power ratio between the direct and the diffused signal component, S is the power in the diffused component, and $I_0(\cdot)$ the modified Bessel function of order 0. The phase statistics of the Ricean fading channel are described by [8]

$$f(\theta) = \frac{e^{-K}}{2\pi} + \frac{\sqrt{K}\cos\theta\exp\left(-K\sin^2\theta\right)}{2\sqrt{\pi}} \cdot \left[2 - \mathrm{erfc}\left(\sqrt{K\cos\theta}\right)\right] \tag{1.4}$$

where $\mathrm{erfc}(\cdot)$ denotes the complementary error function. For both Rayleigh and Ricean fading channels, the diffused signal component has a two-sided bandwidth of $2B_F = 2vf_c/c$ where f_c is the carrier frequency, c the propagation velocity and v the velocity of the user. Depending upon the values of v, as well as on the transmitted symbol rate $1/T$, the fading could be characterized as either fast or slow. B_F is also known as the fading bandwidth or maximum Doppler shift. The power spectral density of the faded signal, depends upon the fading spectrum assumed. Examples of several such spectra can be found in [6]; two of them, the uniform and the land-mobile, will be used extensively in this thesis (see Chapter 2).

Depending upon the values of the delay spread, τ_d, of the reflected waves, as compared to the symbol duration T, the fading could be frequency selective or frequency nonselective (or flat). For large values of $\tau_d T$ (typically > 0.1) it is probably fair to state that fading is frequency selective. For smaller values of $\tau_d T$, the fading becomes frequency nonselective, i.e., flat. In practice, frequency flat and frequency selective fading coexist in mobile radio communication channels (e.g., [9]). However, for the purpose of this thesis, the Rayleigh and Ricean frequency nonselective (flat) fading channel model will be adopted.

1.2. PSK and QAM type of Signals

Perhaps the most commonly used bandwidth efficient techniques for transmission of digital signals, are the Phase Shift Keying (PSK) and Quadrature Amplitude Modulation (QAM) techniques [10].

- ☐ ***M*-ary PSK**: This is a technique according to which the transmitted symbols are used to produce M distinct carrier phases, which are traditionally, uniformly distributed over $[0,2\pi)$ [11].
- ☐ ***M*-ary QAM**: According to this technique, the information symbols are transmitted using a combination of M amplitudes and phases of the transmitted carrier, in such a way that the transmitted signal constellation has a rectangular form [10].

Examples of typical PSK and QAM signal constellations are illustrated in Fig. 1.1. A modulation

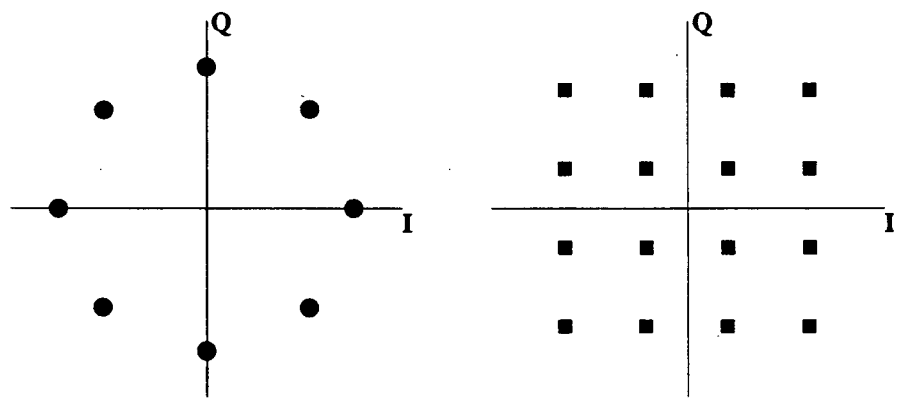

(a) 8-PSK. (b) 16-QAM.

Fig. 1.1. The signal space of 8–PSK (a), and 16–QAM (b).

format which is unique, is Quadrature PSK (QPSK), since it can be viewed both as 4–PSK and 4–QAM. Furthermore, the recent decision by the EIA/TIA [12] to adopt a QPSK type signal, namely the $\pi/4$–shift DQPSK, as the transmission standard for the emerging Northern American digital cellular system, has created a flurry of research activity in systems employing this modulation format [13, 14]. As it can be seen from Fig. 1.2, a pair of input bits are

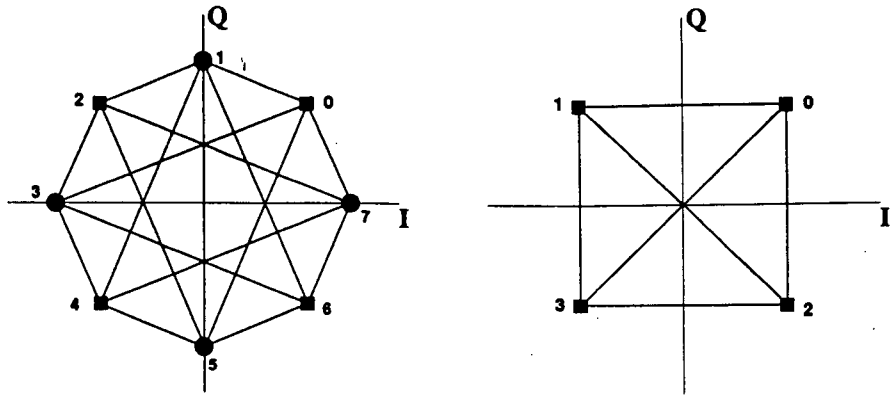

(a) $\pi/4$-shift DQPSK. (b) QPSK.

Fig. 1.2. The signal space of $\pi/4$–shift DPQSK (a), versus the signal space of QPSK (b).

differentially encoding the transmitted carrier phase, so that the carrier phase angle at the i-th symbol interval is given by

$$\theta_i = \theta_{i-1} + \Delta\theta_i \tag{1.5}$$

where $\Delta\theta_i$ is the differential phase, taking values from the alphabet $\{\frac{\pi}{4}, \frac{3\pi}{4}, \frac{5\pi}{4}, \frac{7\pi}{4}\}$. The principal advantages presented by this modulation scheme, as compared to QPSK, are a) reduced envelope fluctuation, rendering it less prone to distortion imposed by non-linear power amplifier stages, and b) the receiver's ability to recover the transmitted information in a noncoherent (i.e., differential) fashion [15]. This second advantage, also leads to considerable system simplification, as the information bearing carrier signal does not have to be recovered at the receiver end.

1.3. Digital Transmission over Fading Channels

The recent trend towards an all digital network (see for example [16]), has led to an increasing need for reliable transmission of digital voice and data in mobile radio applications, i.e., reliable digital transmission over fading channels. However, in such a fading environment, digital transmission schemes, apart from their overall poor performance, exhibit an irreducible error-rate known as "error floor" which is caused by the random phase disturbance (otherwise called random-FM) imposed by the fading [5]. In this respect, over the past few years, a large number

of "fading resistive" techniques for communication systems have been proposed, analyzed and evaluated. Examples include interleaving/deinterleaving [17–19], trellis coded modulation [17, 19, 20], prediction/cancellation techniques [21, 22], or combinations of the above.

The transmission/detection techniques may be further divided into two broad categories. The first one deals with coherent systems. The majority of these techniques involve the transmission of pilot tones (e.g., [23, 24]), or pilot sequences (e.g., [25–27] which are used to extract the channel impairment. At the receiver, after suitable processing, these pilot tones or sequences can be used as coherent reference to cancel the effects of fading on the digital information signal. The problem of optimal carrier recovery for PSK schemes employing symbol-by-symbol receivers, operated in a Rayleigh faded environment, has been addressed in [28, 29], and more recently in [30]. The second category involves techniques which are based on noncoherent detection (e.g., [31–34, 18, 17, 19]). Noncoherent detection can be further subdivided into differential (e.g., [31–34, 19, 35]) and limiter—FM-discriminator detection (e.g., [15, 36]). For the former one, the phase of the carrier corresponding to the previous transmitted data symbol, is used as demodulation reference. For the latter one, the receiver consists of a limiter/discriminator followed by an integrate-and-dump postdetection filter. Performance comparisons for some of these techniques can be found in [37, 38].

Based on the published literature, it is fair to state that there is no "clear-cut winner" between the various coherent and noncoherent detection techniques. Nevertheless, it seems that in a severe fading environment such as the mobile radio channel, the implementation simplicity and robustness of noncoherent detection make it the preferred detection scheme [34, 38, 39].

1.4. Research Objectives of this Thesis

Motivated by the above, this thesis addresses the general problem of optimal detection of both coded and uncoded, differentially encoded or not, PSK and QAM signals in frequency

nonselective Rayleigh or Ricean channels. Its research contributions can be summarized as follows.

1. Theoretical derivation of the maximum likelihood sequence detector for PSK and QAM signals transmitted over such fading channels. It is shown that the detector's structure can be realized as a combination of envelope, multiple differential and coherent detectors. In addition to the optimal detection algorithm, several reduced complexity, as well as recursive algorithms are also proposed.
2. Obtain by means of computer simulation, BER performance evaluation results for the reduced complexity algorithms employing various digital modulation schemes, including coded and uncoded $\pi/4$–shift DPQSK, QPSK, $\pi/4$–shift DQAM and 8–QAM.
3. Design, hardware/software implementation of a prototype $\pi/4$–shift DPQSK modem, employing a Digital Signal Processor (DSP) based receiver, so that the effectiveness of the proposed detector structures could be verified experimentally.

1.5. Thesis organization

Including this introductory chapter, the thesis consists of five chapters and three appendixes. Its organization is as follows

- **Chapter 2** contains all the theoretical derivations. The mathematical model for the communication system under consideration is first presented. Afterwards, the optimal detector for channels corrupted by AWGN and flat Rayleigh and Ricean fading is derived. Reduced complexity and recursive forms of the detection algorithm are also presented.
- In **Chapter 3**, computer simulation software developed for obtaining the BER of a wide variety of digital communication systems is presented. This software is then used to obtain the BER performance of the receiver structures derived in Chapter 2.

- **Chapter 4** includes the implementation details for the hardware design of the prototype $\pi/4$–shift DPQSK system. Firstly, the design and implementation of the DPQSK baseband generator is described. Secondly, the hardware implementation of the RF Modulator/Demodulator (MODEM), as well as the channel, is presented. Thirdly, the DSP-based receiver design and realization is given.
- In **Chapter 5**, the experimental testbed set up to evaluate the developed prototype $\pi/4$–shift DPQSK system is presented. In addition, measurements performed on the experimental setup, including BER performance results obtained for various experimental MODEM configurations, are given. Finally, comparisons between simulated and measured performances are discussed.
- **Chapter 6** contains the conclusions of this thesis, together with suggestions for future work.
- In **Appendix A**, some of the detailed theoretical derivations, for the optimal detector derived, are given.

2. Optimal and Reduced Complexity Detection in Flat Fading Channels

2.1. Introduction

In this chapter, the derivation of the maximum likelihood sequential detector for trellis-coded or uncoded PSK and QAM signals (differentially encoded or not), in channels corrupted by multiplicative frequency nonselective Rayleigh or Ricean fading, as well as additive white Gaussian noise (AWGN), is presented. In addition, various suboptimal, reduced complexity versions of the optimal algorithms are also presented. The organization of the chapter is as follows. After this introduction, in the second section, a detailed description of the communications system under consideration, is given. The derivation of the optimal detector for signals transmitted over fading channels is presented in the third section. Some reduced complexity algorithms are also derived in the same section. The structure of two recursive algorithms is presented in the fourth section, while the conclusions of this chapter can be found in the last section.

2.2. System Model Description

The block diagram of the transmitter is shown in Fig. 2.1. It consists of a Convolutional

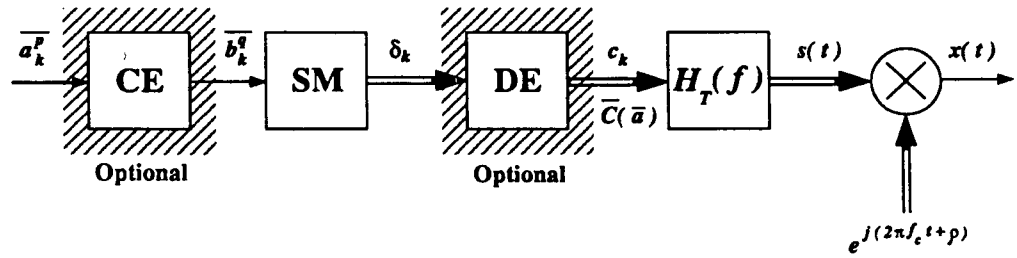

Fig. 2.1. Block diagram of the transmitter model assumed; CE: Convolutional Encoder, SM: Signal Mapper, DE: Differential Encoder, $H_T(f)$: Transmit filter.

Encoder (CE) which is optional, a Signal Mapper (SM), a Differential Encoder (DE) which

is optional also, a transmit filter with transfer function $H_T(f)$ and a modulator. The p-bit information word $\overline{a_k^p} = [a_k^1, a_k^2, ..., a_k^p]$ consists of independent and equiprobable bits, taking values from the alphabet {0,1}. If the CE is used, the output is a q-bit word $\overline{b_k^q} = [b_k^1, b_k^2, ..., b_k^q]$, resulting in a q/p rate convolutional code. The SM converts the binary sequences $\overline{b_k^q}$ into symbols $\delta_k = \gamma_k e^{j\Omega_k}$, where γ_k and Ω_k represent the envelope and phase of δ_k, respectively. The mapping of bit combinations $\overline{b_k^q}$ to symbols δ_k on the signal constellation, can be done according to the set partitioning technique described in [40]. In the special case of PSK signals, γ_k is constant and without loss of generality may be assumed equal to one, while Ω_k can be obtained by the following Eq.

$$\Omega_k = \frac{\pi}{2^q} \sum_{i=1}^{q} 2^{i-1}(2b_k^i - 1) \quad . \tag{2.1}$$

If the optional DE is used, the sequence of δ_k's is translated to a new sequence $\overline{C}(\overline{a})$ of c_k's, i.e., $\overline{C}(\overline{a}) = [c_1, c_2, ..., c_L]$, where

$$c_k = \delta_k c_{k-1} = e^{j(\Phi_{k-1} \oplus \Omega_k)} \tag{2.2}$$

with Φ_k representing the phase of c_k and $\oplus$ modulo 2π addition.

The signal at the output of the transmit filter $H_T(f)$ can be represented as

$$s(t) = \sum_{k=0}^{L} c_k h_T(t - kT) \tag{2.3}$$

where $h_T(t)$ is the impulse response corresponding to $H_T(f)$, T the symbol duration and L the number of symbols to be transmitted. After the modulator, the transmitted signal can be expressed as

$$x(t) = \mathrm{Re}\Big\{ s(t) e^{j(2\pi f_c t + \rho)} \Big\} \tag{2.4}$$

where $\mathrm{Re}\{\cdot\}$ denotes real part, f_c is the carrier frequency and ρ the initial phase of the modulator.

It is assumed that $x(t)$ is corrupted by multiplicative, frequency nonselective fading $f(t)$ and AWGN $n(t)$ with one sided power spectral density N_0. Following [5], and as illustrated

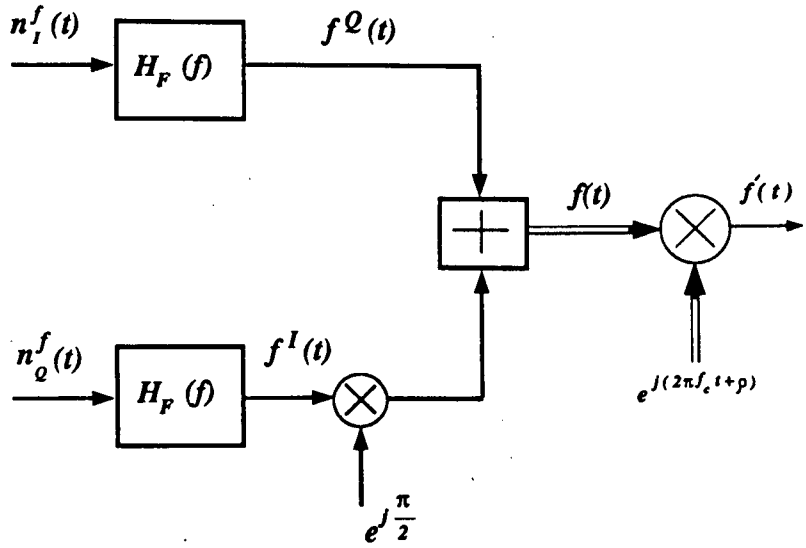

Fig. 2.2. Block diagram of the frequency nonselective fading model.

in Fig. 2.2, $f(t)$ is modelled as a complex summation of two white and independent Gaussian noise processes, $n_I^f(t)$ and $n_Q^f(t)$, filtered by two identical filters, $H_F(f)$. $f'(t)$ is the fading signal modulated by f_c. $f(t)$ can be expressed mathematically as

$$f(t) = f^I(t) + jf^Q(t) \tag{2.5}$$

with both $f^I(t)$ and $f^Q(t)$ having the same autocorrelation function given by

$$\begin{aligned} R_f(\tau) =& E\left\{\left[f^I(t) - \overline{f^I}\right]\left[f^I(t-\tau) - \overline{f^I}\right]\right\} = \\ & E\left\{\left[f^Q(t) - \overline{f^Q}\right]\left[f^Q(t-\tau) - \overline{f^Q}\right]\right\} = \\ & N_F \int_{-\infty}^{\infty} |H_F(f)|^2 e^{j2\pi f\tau} d\tau \end{aligned} \tag{2.6}$$

where $E\{\cdot\}$ denotes the expected value, $\overline{f^I} = E\{f^I(t)\}$, $\overline{f^Q} = E\{f^Q(t)\}$ and N_F is the power spectral density of $n_I^f(t)$ or $n_Q^f(t)$. The cross-correlation of $f^I(t)$ and $f^Q(t)$ is zero since they are independent. Without any loss of generality, from this point and on, it will be assumed for mathematical convenience that $\overline{f^Q} = E\{f^Q(t)\} = 0$. This by no means compromises

the generality of the theoretical analysis, as it amounts to assuming that the transmitted signal carrier has phase equal to 0. In other words, as $\overline{f^I}$ is varied in order to accommodate the Ricean fading channel, the probability density function (pdf) of the faded carrier phase, will present a maximum at zero degrees. The transfer function of the employed fading filters specifies the spectral characteristics of the fading model considered, e.g., rectangular [41], Gaussian (aeronautical channel) [42–44] and land mobile [5]. In this thesis, two fading models were considered, the rectangular (or uniform) for mathematical convenience in the initial theoretical derivations, and the land mobile. It is well known that the autocorrelation function for the rectangular fading model is given by [6]

$$R_f(\tau) = \frac{\sin(2\pi B_F \tau)}{2\pi B_F \tau} \tag{2.7}$$

whereas for the land mobile by [5]

$$R_f(\tau) = J_0(2\pi B_F \tau) \tag{2.8}$$

where $J_0(\cdot)$ is the zero order Bessel function of the first kind and B_F is the fading bandwidth. Normalizing B_F to the symbol rate $1/T$, the higher the $B_F T$ product, the faster the fading interference changes with respect to the symbol duration. As well known, the $B_F T$ product is an important parameter when evaluating the performance of digital modulation schemes transmitted over a fading channel. The main reason for this is that the occurrence of "error floors" is directly related to the $B_F T$, i.e., when $B_F T$ is increased, the error floor will occur at a higher bit error rate (BER). For example, for a conventional differentially detected $\pi/4$–shift DQPSK system, a $B_F T$=0.0041 will result in an error floor at approximately 2×10^{-4}, whereas a $B_F T$=0.026 will produce an error floor at approximately 9×10^{-3}. It should be noted that from the open technical literature there exists no clear definition as to which $B_F T$ product results in fast fading. For the purpose of this thesis, however, it will be assumed that for $B_F T > 0.1$ we have fast fading. As previously mentioned, $f(t)$ will be assumed to have both Rayleigh and Ricean characteristics.

characteristics. For the Ricean fading channel, the K factor, defined as the ratio of the direct signal component to the multipath power [6], will be used in comparing system performance. Following the notation used so far, K can be expressed in deciBells (dB) as

$$K_{\text{dB}} = 10 \log_{10} \left[\frac{\left(\overline{f^I}\right)^2}{\sigma_{f^I}^2 + \sigma_{f^Q}^2} \right] \tag{2.9}$$

where $\sigma_{f^I}^2$ and $\sigma_{f^Q}^2$ are the squared variances of $f^I(t)$ and $f^Q(t)$, respectively. Clearly, from Eq. 2.9, as $\overline{f^I} \to 0$, $K \to -\infty$ effectively changing the type of fading from Ricean to Rayleigh.

The block diagram of the receiver is depicted in Fig. 2.3. The received signal $x_r(t)$, after

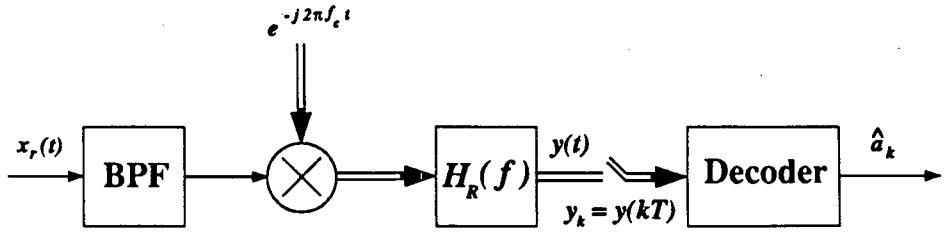

Fig. 2.3. Block diagram of the receiver; BPF: Band Pass Filter, $H_R(f)$: Receiver filter.

corruption from fading and AWGN, can be expressed as

$$x_r(t) = x(t)f'(t) + n(t) \, . \tag{2.10}$$

$x_r(t)$ is passed through a wideband (roofing) Band Pass Filter (BPF) which limits the Gaussian noise input to the receiver, without distorting the information signal. After being downconverted[2], it is passed through a pre-detection low-pass filter $H_R(f)$, which is assumed to be matched to $H_T(f)$.

From Fig. 2.3, the signal at the output of $H_R(f)$ can be expressed mathematically as

$$y(t) = f(t) \sum_{k=0}^{L} c_k e^{j\rho} h(t - kT) + n_s(t) - j n_c(t) \tag{2.11}$$

[2] This was assumed for mathematical convenience in order to carry out the theoretical derivations in the complex baseband domain. Furthermore, this is the worst-case approach, since the fading present will be entirely transformed into the equivalent baseband process, whereas in a conventional differential detector, for example, the fading correlation between adjacent signal samples will result in partial fading interference cancellation.

where $h(t)$ represents the impulse response corresponding to the product $H_T(f) \cdot H_R(f)$, $n_s(t)$ and $n_c(t)$ represent the inphase and quadrature baseband components of the narrowband Gaussian noise, respectively. Both $n_s(t)$ and $n_c(t)$ have the same variance, equal to $\sigma_G^2 = \frac{N_0}{2T}$, which is the received noise power as well, since both have mean equal to 0. In deriving Eq. 2.11, it has been assumed that $H_R(f)$ is significantly wider than the bandwidth of the fading process, as this is the case for almost any practical application. However, it should be pointed out that for the computer simulations, the performance evaluation results which are presented in Chapter 3, any effects of this filter on the fading process will be included. Furthermore, if $H_T(f)$ and $H_R(f)$ are chosen so that $h(t)$ satisfies Nyquist's first criterion, we obtain [2]

$$h(kT_s) = \begin{cases} 1 & \text{if } k = 0 \\ 0 & \text{otherwise.} \end{cases} \tag{2.12}$$

Hence, the sampled at $t = kT$ signal $y_k = y(kT)$ is given by

$$y_k = \left(f_k^I + j f_k^Q\right) c_k e^{j\rho} + n_s(kT) - j n_c(kT) \tag{2.13}$$

where $f_k^I = f^I(kT)$, $f_k^Q = f^Q(kT)$. The samples y_k $(0 \leq k \leq L)$ are then fed into a decoder for further processing in order to recover the transmitted symbols c_k and subsequently the transmitted information sequence $\overline{a_k^p}$.

2.3. Derivation of the Optimal Decoder Structure

The optimal, in the maximum likelihood sense, decoder must choose the data sequence $\overline{a} = \left[\overline{a_1^p}, \overline{a_2^p}, ..., \overline{a_L^p}\right]$ which maximizes the probability density function (pdf) $\mathbf{f}\left[\overline{y} \mid \overline{C}(\overline{a}), \rho\right]$ with $\overline{y} = [y_1, y_2, ..., y_L]$. Using well known probabilistic identities, $\mathbf{f}\left[\overline{y} \mid \overline{C}(\overline{a}), \rho\right]$ can be expressed as [8]

$$\mathbf{f}\left[\overline{y} \mid \overline{C}(\overline{a}), \rho\right] = \prod_{i=1}^{L} \mathbf{f}\left[y_i \mid y_{i-1}, y_{i-2}, ...y_0, \overline{C}(\overline{a}), \rho\right] . \tag{2.14}$$

For mathematical convenience, we will define the variables e_k^I and e_k^Q as

$$e_k^I = f_k^I + n_e^I = \frac{\mathrm{Re}\left(y_k c_k^* e^{-j\rho}\right)}{|c_k|^2} \; ; \quad e_k^Q = f_k^Q + n_e^Q = \frac{\mathrm{Im}\left(y_k c_k^* e^{-j\rho}\right)}{|c_k|^2} \; . \tag{2.15}$$

where $\mathrm{Re}(\cdot)$ and $\mathrm{Im}(\cdot)$ denote real and imaginary part, respectively, and * complex conjugate. From Eq. 2.12 it follows that, $n_e^I(k)$ and $n_e^Q(k)$ are given by

$$n_e^I(k) = \frac{n_s(kT)\mathrm{Re}\left(c_k^* e^{-j\rho}\right) + n_c(kT)\mathrm{Im}\left(c_k^* e^{-j\rho}\right)}{|c_k|^2} \tag{2.16}$$

and

$$n_e^Q(k) = \frac{n_s(kT)\mathrm{Im}\left(c_k^* e^{-j\rho}\right) - n_c(kT)\mathrm{Re}\left(c_k^* e^{-j\rho}\right)}{|c_k|^2}. \tag{2.17}$$

Since $n_c(kT)$, $n_s(kT)$, f_k^I and f_k^Q are Gaussian random variables, from Eq. 2.15 it follows that e_k^I and e_k^Q are also Gaussian random variables. Furthermore, as it is shown in Appendix A.1, they have the same autocorrelation function, given by

$$\begin{aligned} R_e\left[\overline{C}(\overline{a}), (k-i)T\right] &= E\left\{e_k^I e_i^I\right\} = E\left\{e_k^Q e_i^Q\right\} \\ &= R_f(k-i) + \frac{\sigma_G^2 \delta(k-i)}{|c_k|^2} \end{aligned} \tag{2.18}$$

where $\delta(\cdot)$ is the Kronecker δ-function. From Eq. 2.18, it can be seen that for multi-amplitude signal constellations, e.g., QAM, the autocorrelation properties of e_k^I and e_k^Q depend upon the transmitted sequence. For one single amplitude constellations however, e.g. M-PSK and $\pi/4$–shift DQPSK, where $|c_k|^2$ is constant, e_k^I and e_k^Q are independent from the transmitted sequence $\overline{C}(\overline{a})$. The derivation of the optimal detector, is based on the following theorem from probability theory [8].

Theorem: For the zero mean Gaussian random variables $n_l, n_{l-1}, n_{l-2}, ..., n_0$ with covariance $R_{i-j} = E\{n_i n_j\}$, the conditional pdf of n_l given $n_{l-1}, n_{l-2}, ..., n_0$, is given by

$$\zeta(n_l \mid n_{l-1}, n_{l-2}, ..., n_0) = \frac{1}{\sqrt{2\pi\xi_{p,l}^2}} \exp\left[\frac{-(n_l - \widehat{n_l})^2}{\xi_{p,l}^2}\right]. \tag{2.19}$$

In Eq. 2.19, $\xi_{p,l}^2$ is the minimum mean square prediction error (MMSPE), while $\widehat{n_l}$ represents the prediction of n_l based on the previous samples $n_{l-1}, n_{l-2}, ..., n_0$ and is given by

$$\widehat{n_l} = \sum_{j=1}^{l} p_{l,j} n_{l-j} \tag{2.20}$$

where $p_{l,j}$ are the linear prediction coefficients, with l being the order of prediction. The MMSPE can be calculated from the following Eq.

$$\xi_{p,l}^2 = R_0 - \sum_{j=1}^{l} p_{l,j} R_j \ . \tag{2.21}$$

Based on the above theorem, the pdf which the optimum detector must maximize, can be rewritten as follows

$$\begin{aligned} \mathrm{f}[\overline{y} \mid \overline{C}(\overline{a}), \rho] = \prod_{k=1}^{L} \frac{1}{2\pi\sigma_k^2} \exp\left[-\frac{1}{2\sigma_k^2} \left\{ \frac{\mathrm{Re}\left(y_k c_k^* e^{-j\rho}\right)}{|c_k|^2} - \overline{fI} - \sum_{i=1}^{k} p_{k,i} \left[\frac{\mathrm{Re}\left(y_{k-i} c_{k-i}^* e^{-j\rho}\right)}{|c_{k-i}|^2} - \overline{fI} \right] \right\}^2 \right] \\ \exp\left[-\frac{1}{2\sigma_k^2} \left\{ \frac{\mathrm{Im}\left(y_k c_k^* e^{-j\rho}\right)}{|c_k|^2} - \sum_{i=1}^{k} p_{k,i} \frac{\mathrm{Re}\left(y_{k-i} c_{k-i}^* e^{-j\rho}\right)}{|c_{k-i}|^2} \right\}^2 \right] . \end{aligned} \tag{2.22}$$

In the above equation, $\sigma_k^2 = \sigma_k^2\left[\overline{C}(\overline{a})\right]$ represents the minimum mean square prediction error of order k, and $p_{k,i} = p_{k,i}\left[\overline{C}(\overline{a})\right]$ $(0 \le k \le L;\ 0 \le i \le k)$ the linear prediction coefficients. The values of these coefficients, depend upon both the $B_F T$ product, the fading model assumed, the operating Signal-to-Noise ratio (SNR)[3], the ratio of powers of the fading signal and the Gaussian noise, i.e., $R_f(0)/\sigma_G^2\left[\overline{C}(\overline{a})\right]$, and for multiamplitude signal constellations, on the transmitted sequence. Maximization of the pdf in Eq. 2.22 is equivalent to minimizing the function

$$\begin{aligned} \sum_{k=1}^{L} \frac{1}{\sigma_k^2} \Bigg\{ \left[\frac{\mathrm{Re}\left\{y_k c_k^* e^{-j\rho}\right\}}{|c_k|^2} - \sum_{i=1}^{k} p_{k,i} \left(\frac{\mathrm{Re}\left\{y_{k-i} c_{k-i}^* e^{-j\rho}\right\}}{|c_{k-i}|^2} - \overline{fI} \right) - \overline{fI} \left(1 - \sum_{i=1}^{k} p_{k,i} \right) \right]^2 + \\ + \left[\frac{\mathrm{Im}\left\{y_k c_k^* e^{-j\rho}\right\}}{|c_k|^2} - \sum_{i=1}^{k} p_{k,i} \frac{\mathrm{Im}\left\{y_{k-i} c_{k-i}^* e^{-j\rho}\right\}}{|c_{k-i}|^2} \right]^2 \Bigg\} . \end{aligned} \tag{2.23}$$

The prediction coefficients can be calculated by solving the following set of equations [8]

$$\widetilde{P_k}\left[\overline{C}(\overline{a})\right] = \widetilde{D_k}\left[\widetilde{R_k}\left[\overline{C}(\overline{a})\right]\right]^{-1} \tag{2.24}$$

where $\widetilde{P_k}\left[\overline{C}(\overline{a})\right]$ is a $[k \times 1]$ matrix, $\widetilde{D_k}$ is a $[k \times 1]$ matrix and $\widetilde{R_{kj}}\left[\overline{C}(\overline{a})\right]$ is $[k \times k]$ matrix with

$$\begin{aligned} \widetilde{P_k}\left[\overline{C}(\overline{a})\right] &= \left[p_{k,1}\left[\overline{C}(\overline{a})\right], p_{k,2}\left[\overline{C}(\overline{a})\right], ..., p_{k,k}\left[\overline{C}(\overline{a})\right]\right]^{\mathrm{T}} \\ \widetilde{D_k} &= \left[R_f(1), R_f(2), ..., R_f(k)\right]^{\mathrm{T}} \end{aligned} \tag{2.25}$$

---

[3] Note that SNR=E_s/N_0, where E_s is the energy per transmitted symbol.

with T denoting transpose and

$$\widetilde{R_k}\left[\overline{C}(\overline{a})\right] = \begin{bmatrix} R_f(0)+\frac{\sigma_G^2}{|c_k|^2} & R_f(1) & \cdots & R_f(k) \\ R_f(1) & R_f(0)+\frac{\sigma_G^2}{|c_{k-1}|^2} & \cdots & R_f(k-1) \\ \vdots & \vdots & \ddots & \vdots \\ R_f(k) & R_f(k-1) & \cdots & R_f(0)+\frac{\sigma_G^2}{|c_0|^2} \end{bmatrix}. \tag{2.26}$$

From the above, it is clear that as the SNR increases, the fading autocorrelation terms in the matrix of Eq. 2.26 become dominant over the noise terms $\sigma_G^2/|c_i|^2$, and hence, the values of the prediction coefficients will eventually converge to asymptotic values. These values obtained for SNR $\rightarrow \infty$, will depend only upon the fading process. Furthermore, from the matrix shown in Eq. 2.26, it is evident that for single amplitude signals such as M-PSK for which $|c_k|^2$ is constant, the prediction coefficient values will not depend on the transmitted sequence.

As numerical examples, for prediction order up to four, the prediction coefficients, as well as the MMSPE, for $B_FT = 0.125$ and $B_FT = 0.0125$ are plotted in Fig. 2.4 and 2.5. Evident from both figures are the asymptotic (as SNR $\rightarrow \infty$) values for all prediction coefficients shown, as well as the constant values of the MMSPE for high SNR. Furthermore, as it was expected, the MMSPE values decrease as the order of prediction increases. This clearly indicates that a system employing a higher order of prediction will perform better than the same system utilizing a lower prediction order. One more interesting observation is the quantizing effect on the prediction coefficient values for decreasing B_FT. This behavior could be important for practical implementation of the detection algorithm, as the same coefficient values can be used over a relatively wide SNR range.

Returning back to Eq. 2.23, it is shown in Appendix A.2, that maximization of $\mathrm{f}\left[\overline{y} \mid \overline{C}(\overline{a}), \rho\right]$, with respect to the transmitted information sequence $\overline{C}(\overline{a})$, is shown to be equivalent to

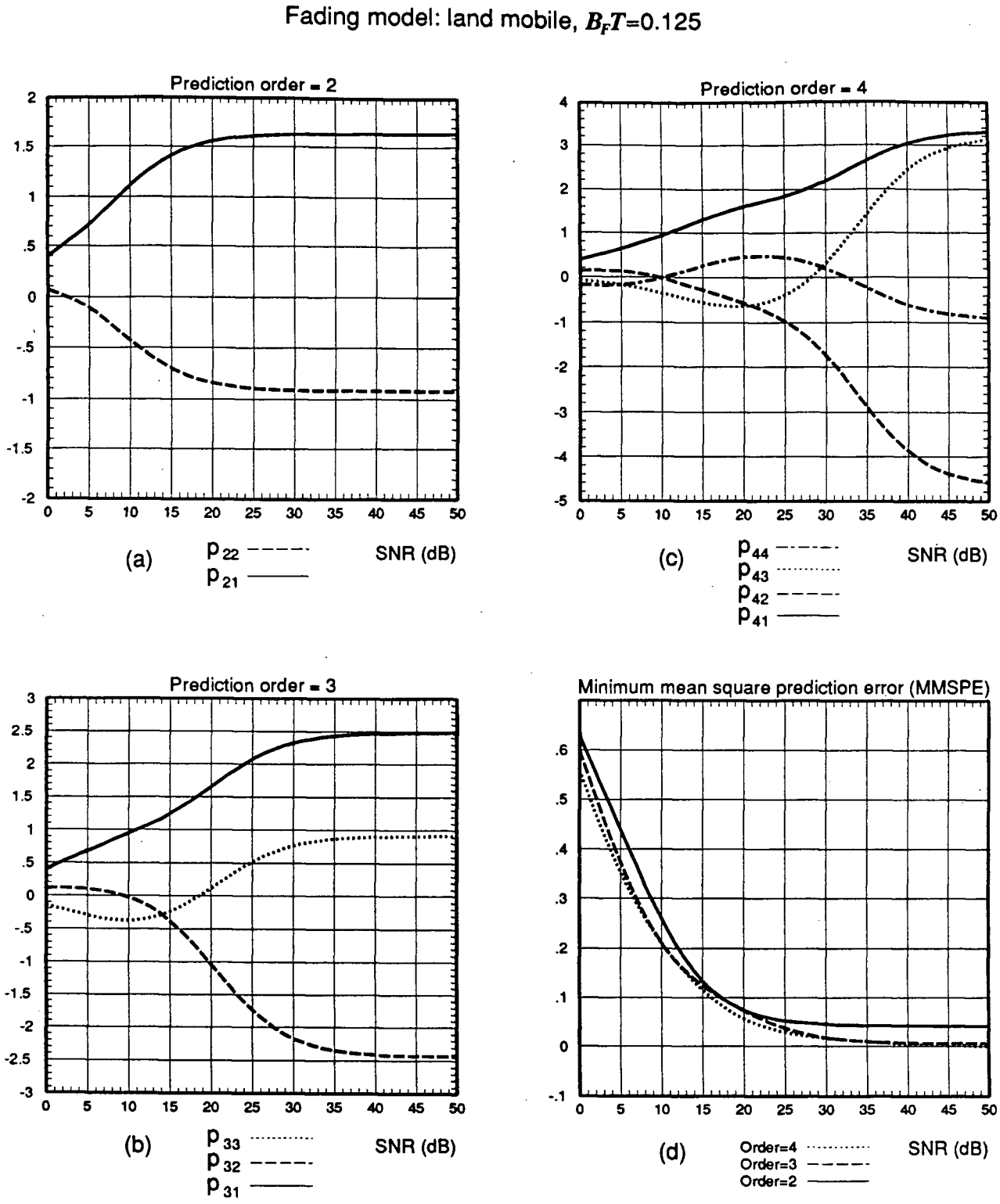

Fig. 2.4. Prediction coefficients and MMSPE for land mobile channel with $B_FT = 0.125$; (a): 2nd order prediction, (b): 3rd order prediction, (c): 4th order prediction, (d): MMSPE.

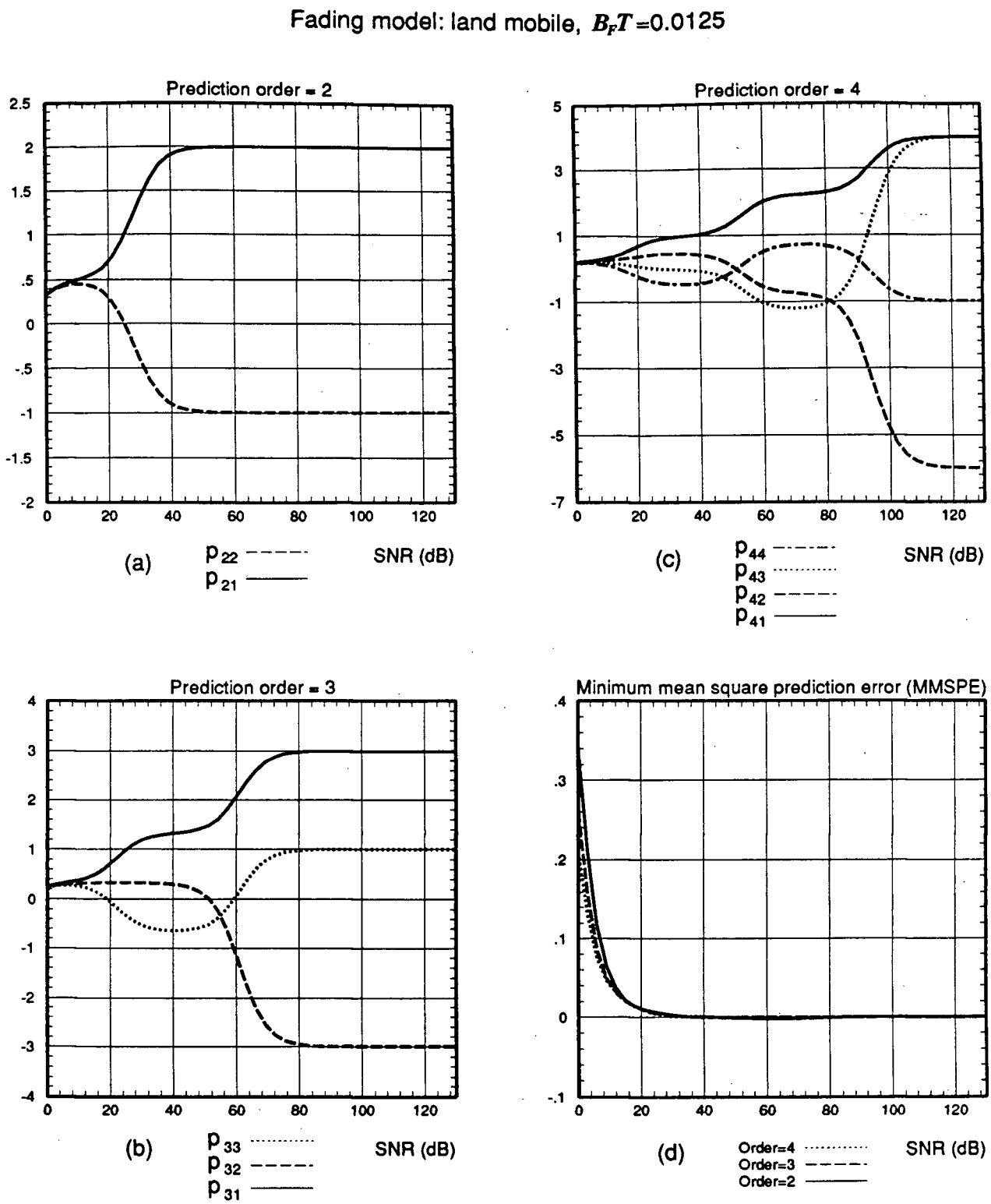

Fig. 2.5. Prediction coefficients and MMSPE for land mobile channel with $B_FT = 0.0125$; (a): 2nd order prediction, (b): 3rd order prediction, (c): 4th order prediction, (d): MMSPE.

minimizing the following function

$$
\begin{aligned}
&2\sum_{k=1}^{L}\sum_{i=1}^{k}\frac{\mathrm{Re}(y_k y_{k-i}^*)\mathrm{Re}(c_k c_{k-i}^*)+\mathrm{Im}(y_k y_{k-i}^*)\mathrm{Im}(c_k c_{k-i}^*)}{|c_k|^2|c_{k-i}|^2}\left[\sum_{j=0}^{L-k}\frac{p_{k+j,j}[\overline{C}(\overline{a})]\,p_{k+j,i+j}[\overline{C}(\overline{a})]}{\sigma_{k+j}^2[\overline{C}(\overline{a})]}\right]+\\
&+\sum_{k=1}^{L}\frac{|y_k|^2}{|c_k|^2}\left[\sum_{i=0}^{L-k}\frac{p_{k+i,i}^2[\overline{C}(\overline{a})]}{\sigma_{k+i}^2[\overline{C}(\overline{a})]}\right]+\\
&+2\overline{f^I}\sum_{k=1}^{L}\frac{\mathrm{Re}(y_k c_k^* e^{-j\rho})}{|c_k|^2}\left[\sum_{i=0}^{L-k}\frac{p_{k+i,i}[\overline{C}(\overline{a})]}{\sigma_{k+i}^2[\overline{C}(\overline{a})]}\left(\sum_{j=0}^{k+i}p_{k+i,j}[\overline{C}(\overline{a})]\right)\right]+\\
&+\sum_{k=1}^{L}\frac{1}{\sigma_k^2[\overline{C}(\overline{a})]}\left[\overline{f^I}\sum_{i=0}^{k}p_{k,i}[\overline{C}(\overline{a})]\right]^2
\end{aligned}
\tag{2.27}
$$

with the terms $p_{k,0}$ defined as $p_{k,0}=-1,\ \ \forall\, 0\le k\le L$. Several interesting observations can be made with reference to the quantities given in Eq. 2.27

- In a Rayleigh fading environment, where $\overline{f^I}=0$, the last two terms become zero, and the expression to be minimized becomes considerably simpler. Furthermore, the last term is independent of the encoded symbols c_k and can be removed from the minimization process.
- In the first term, $\mathrm{Re}(y_k y_{k-i}^*)$ and $\mathrm{Im}(y_k y_{k-i}^*)$ represent the real and imaginary parts of the product between the received sampled signal y_k, and the complex conjugated iT seconds delayed version of y_k. Clearly, this operation represents differential detection with a delay element of iT. It can be seen, that differential detectors with delay elements up to kT are involved. Since the detection of y_k involves all the terms $y_{k-1}, y_{k-2}, ..., y_0$, this corresponds to multiple differential detection, where differential detectors with delay elements $T, 2T, ...$ up to kT are employed. From now on, we will be referring to a differential detector with delay element kT, a k^{th} order differential detector.
- The second term represents, essentially, squared envelope detection $\left(|y_k|^2\right)$. This term contributes to the detection process when multiamplitude signal constellations —such as QAM or multiamplitude PSK— are used. However, for single amplitude signals, where $|c_k|^2$ is constant, this term can be removed from the decoding process, since it's clearly independent of any transmitted information sequence $\overline{C}(\overline{a})$.

- Finally, the third term represents the coherent detection component and requires an estimate of the initial phase ρ of the modulator. This requirement is very different from the carrier recovery requirements of a (conventional) coherent receiver for the fading channel. These receivers require an estimate of this initial phase *in addition to the phase jitter introduced by fading*. This is far from being a trivial task, considering the dynamic behavior of the phase jittering, especially when dealing with fast fading. Due to practical limitations, these estimates are usually very inaccurate and result in poor performance. Note that this coherent detection term, is present for Ricean fading channels, while for Rayleigh fading where $\overline{f^I} = 0$, it is removed from the decoding process. However, even for Ricean fading, elimination of the coherent term from the algorithm results in minimal performance degradation.

Based on the above observations, a more detailed block diagram for the realization of the detector derived is illustrated in Fig. 2.6, where $d_i(k) = y_k y_{k-i}^*$, i.e., it represents the output of the differential detector with delay element equal to iT. Clearly, the three detection subsystems of this optimal decoder are the *Multiple Differential*, *Envelope* and *Coherent* detectors.

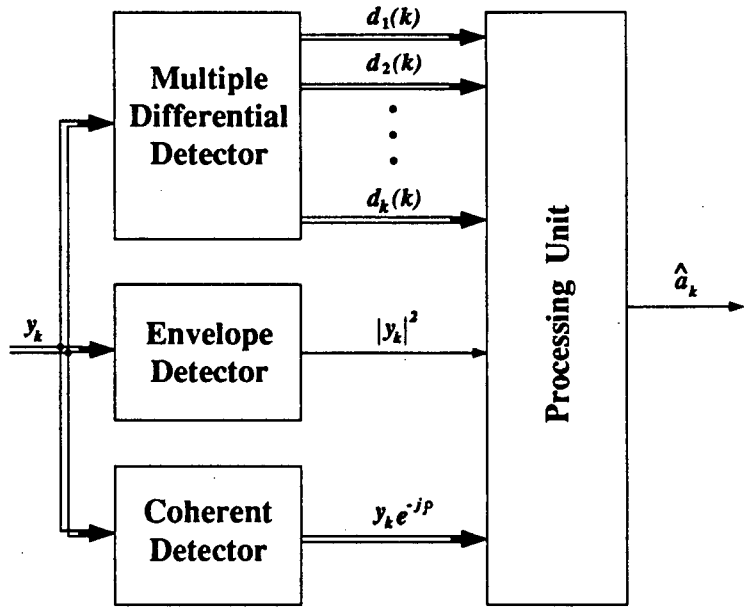

Fig. 2.6. Detailed block diagram of the optimal decoder.

The decoding algorithm described by Eq. 2.27, requires the calculation of coefficients involving the terms $p_{k,i}[\overline{C}(\overline{a})]$ and $\sigma_k^2[\overline{C}(\overline{a})]$ $(1 \leq k \leq L)$. In total there are $\frac{L(L+1)}{2}$ terms for $p_{k,i}$, and L terms for σ_k^2 to be computed. For long sequences, i.e., large values of L, the processing load (computational complexity) required for the calculation of these parameters, as well as the memory storage necessary to store all terms, becomes impractically high. Although the use of more computationally efficient and less memory dependent recursive algorithms, such as the Levinson algorithm [45], can reduce the processing load, the overall complexity will still be high for long sequences[4]. However, this complexity problem can be resolved, by adopting the following approach

- The maximum order of prediction used can be fixed and equal to a relatively small integer z. If z is appropriately chosen, it is expected that this truncation will not result in any significant loss of performance improvement presented by the maximum likelihood form of the algorithm. This expectation stems from the fact that strong correlation usually exists between samples of the fading process with distance of only few symbols. Consequently, terms with greater distance will not contribute significantly to the prediction process, and thus can be dropped. The value chosen for the maximum prediction order z will depend more on the value of the $B_F T$ product and less on the type of fading model assumed.
- The decoding algorithm can be assumed to have been initialized just prior to normal operation, by a known information sequence of length z, e.g., the all zero sequence.

Following the above approach, it is shown in Appendix A.3 that maximization of Eq. 2.27,

---

[4] Especially with regards to the computational complexity, a sequence of more that about 10 symbols is considered to be long.

is equivalent to minimizing the following function

$$\Omega^F_{(\overline{y},\overline{C}(\overline{a}),\rho)} = 2\sum_{k=1}^{L}\sum_{i=1}^{z} \frac{\mathrm{Re}(y_k y^*_{k-i})\mathrm{Re}(c_k c^*_{k-i}) + \mathrm{Im}(y_k y^*_{k-i})\mathrm{Im}(c_k c^*_{k-i})}{|c_k|^2 |c_{k-i}|^2} \mathrm{B}_{z,i}[\overline{C}(\overline{a})] + \\ + \sum_{k=1}^{L} \frac{|y_k|^2}{|c_k|^2} \mathbf{\Gamma}_{z,k}[\overline{C}(\overline{a})] + \\ + \sum_{k=1}^{L} \frac{\mathrm{Re}(y_k c^*_k e^{-j\rho})}{|c_k|^2} \mathbf{\Delta}_{z,k}[\overline{C}(\overline{a})] \tag{2.28}$$

where

$$\mathbf{B}_{z,i} = \sum_{j=0}^{z-i} \frac{p_{z,i}[\overline{C}(\overline{a})]\, p_{z,i+j}[\overline{C}(\overline{a})]}{\sigma_z^2[\overline{C}(\overline{a})]}$$

$$\mathbf{\Gamma}_{z,i} = \frac{1}{\sigma_z^2[\overline{C}(\overline{a})]} \sum_{j=0}^{m} p^2_{z,j}[\overline{C}(\overline{a})] \tag{2.29}$$

$$\mathbf{\Delta}_{z,i} = \frac{2\overline{f^I}}{\sigma_z^2[\overline{C}(\overline{a})]} \sum_{j=0}^{m} p_{z,j}[\overline{C}(\overline{a})] \sum_{l=0}^{z} p_{z,l}[\overline{C}(\overline{a})]$$

and

$$m = \begin{cases} z, & k \le L - z \\ L - k, & k > L - z\,. \end{cases} \tag{2.30}$$

The quantity to be minimized, as it is given by Eq. 2.28, is general enough to accommodate multiamplitude signal constellations, such as M-ary QAM. Furthermore, for single amplitude signals, such as M-ary PSK, the second term is constant, so it can be eliminated. Thus, in this case, the expression to be minimized simplifies to

$$\Theta^F_{(\overline{y},\overline{C}(\overline{a}),\rho)} = 2\sum_{k=1}^{L}\sum_{i=1}^{z} \frac{\mathrm{Re}(y_k y^*_{k-i})\mathrm{Re}(c_k c^*_{k-i}) + \mathrm{Im}(y_k y^*_{k-i})\mathrm{Im}(c_k c^*_{k-i})}{|c_k|^2 |c_{k-i}|^2} \mathrm{B}_{z,i}[\overline{C}(\overline{a})] + \\ + \sum_{k=1}^{L} \frac{\mathrm{Re}(y_k c^*_k e^{-j\rho})}{|c_k|^2} \mathbf{\Delta}_{z,k}[\overline{C}(\overline{a})]\,. \tag{2.31}$$

2.4. Recursive Algorithms

The algorithm can be implemented recursively by keeping an accumulated sum, which will be called **accumulated metric**, and updating it as every new signal sample is fed in.

The incremental quantity added to the accumulated metric will be referred to as **metric**. Two possible forms for this metric can be derived from Eq. 2.23 and 2.28. Limiting the prediction order in Eq. 2.23, to a maximum equal to z, and removing the outer summation operator, we obtain the following metric expression

$$\frac{1}{\sigma_z^2[\overline{C}(\overline{a})]}\left\{\left[\frac{\mathrm{Re}\{y_k c_k^* e^{-j\rho}\}}{|c_k|^2}-\sum_{i=1}^{z}p_{z,i}[\overline{C}(\overline{a})]\left(\frac{\mathrm{Re}\{y_{k-i}c_{k-i}^* e^{-j\rho}\}}{|c_{k-i}|^2}-\overline{f^I}\right)-\overline{f^I}\left(1-\sum_{i=1}^{z}p_{z,i}[\overline{C}(\overline{a})]\right)\right]^2+\right.$$
$$\left.+\left[\frac{\mathrm{Im}\{y_k c_k^* e^{-j\rho}\}}{|c_k|^2}-\sum_{i=1}^{z}p_{z,i}[\overline{C}(\overline{a})]\frac{\mathrm{Im}\{y_{k-i}c_{k-i}^* e^{-j\rho}\}}{|c_{k-i}|^2}\right]^2\right\}. \tag{2.32}$$

Furthermore, from Eq. 2.28, it is fairly easy to see that a second metric form is the function

$$\Delta\Xi^F_{(\overline{y},\overline{C}(\overline{a}),\rho)}=2\sum_{i=1}^{z}\frac{\mathrm{Re}(y_k y_{k-i}^*)\mathrm{Re}(c_k c_{k-i}^*)+\mathrm{Im}(y_k y_{k-i}^*)\mathrm{Im}(c_k c_{k-i}^*)}{|c_k|^2|c_{k-i}|^2}\mathrm{B}_{z,i}[\overline{C}(\overline{a})]+$$
$$+\frac{|y_k|^2}{|c_k|^2}\mathbf{\Gamma}_{z,k}[\overline{C}(\overline{a})]+\frac{\mathrm{Re}(y_k c_k^* e^{-j\rho})}{|c_k|^2}\mathbf{\Delta}_{z,k}[\overline{C}(\overline{a})] \tag{2.33}$$

which is simplified to yield the following for single amplitude signals

$$\Delta\Upsilon^F_{(\overline{y},\overline{C}(\overline{a}),\rho)}=2\sum_{i=1}^{z}\frac{\mathrm{Re}(y_k y_{k-i}^*)\mathrm{Re}(c_k c_{k-i}^*)+\mathrm{Im}(y_k y_{k-i}^*)\mathrm{Im}(c_k c_{k-i}^*)}{|c_k|^2|c_{k-i}|^2}\mathrm{B}_{z,i}[\overline{C}(\overline{a})]+$$
$$+\frac{\mathrm{Re}(y_k c_k^* e^{-j\rho})}{|c_k|^2}\mathbf{\Delta}_{z,k}[\overline{C}(\overline{a})]\ . \tag{2.34}$$

The recursive process has to be initialized before normal detection operation is possible. This can be done during the receiver initialization time, by feeding the algorithm with a number of signal samples corresponding to a known sequence, such as the all-zero sequence. For uncoded systems, the number of samples needed for initialization equal to z, the maximum prediction order used, whereas for systems employing convolutional coding, it also depends on the constraint length of the code used.

2.5. Conclusions

In this chapter, the optimal decoder was presented, for trellis-coded or uncoded PSK and QAM systems, possibly employing differential phase encoding, operating in channels corrupted by multiplicative frequency nonselective Rayleigh or Ricean fading, as well as AWGN. It was

shown, by using maximum likelihood detection arguments, that its structure can be realized by employing *multiple differential detectors*, an *envelope* detector, a *coherent* detector and a sequential algorithm. Finally various reduced complexity versions of the optimal detection algorithm were derived, in order to facilitate practical implementation, and recursive formulas for metric computation, used in receivers employing sequential decoding, were presented.

3. Computer Simulation Performance Evaluation: Software System Description and BER results

3.1. Introduction

The purpose of this chapter is twofold. Firstly (in Section 3.2), it presents a somewhat detailed description of computer simulation software which can be used to evaluate the BER performance of a great deal of digital communication systems, under various channel conditions. All programs used, were developed by the author of this thesis, since no communication systems simulation software was provided with BloSim. This library of programs is currently being used by several graduate students in the Department of Electrical Engineering at UBC. Secondly (in Section 3.3), it presents the BER performance evaluation of various modulation schemes, operated in fading channels, employing the receiver structures derived in the previous chapter. The conclusions of this chapter can be found in Section 3.4.

3.2. Software Simulation Model Description

The software needed for the system evaluation was implemented using the **BloSim** general simulation software package. BloSim was written in C by Dr. D. G. Messerschmitt of the Department of Electrical Engineering and Computer Science, at the University of California Berkeley [46]. This software package integrates simulation blocks written in the C programming language, providing only a kernel which supervises the input to and output from such blocks. Use of the C language not only frees the programmer from the constraints imposed by any special simulation language, but also provides great versatility in the implementation of complex algorithms. BloSim version 2.0 and 3.0, released on November 1988, was provided to the Communications Lab with a few examples of simulation blocks, but without any communication systems software. Such software is now available as a product of the research work reported in

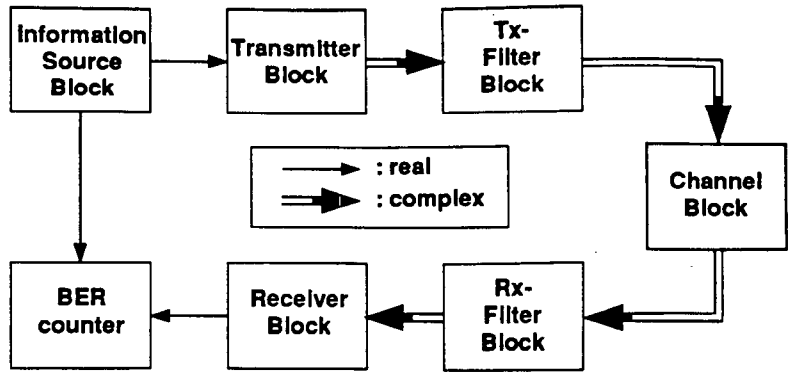

Fig. 3.1. Functional block-diagram of the communication system in software.

this thesis, covering a large number of modulation formats, filters, channel models and receiver structures.

Using BloSim terminology [46], the simulation blocks are referred to as "stars". They make use of BloSim macro definitions which provide versatile and easy to use input/output functions in the form of FIFO (First In First Out) buffers. Connections between blocks are described in a text file called the "universe file". Through this file and the use of macros for parameter entry, numerical values for specific block-parameters (model parameters of interest) can be entered at run-time, thus considerably minimizing the need for re-compilation between simulation runs. The algorithmic modeling of the digital communication system discussed in the previous chapter is described in the following list of functional blocks, an illustration of which is presented in Fig. 3.1. Sources for the BloSim "stars" implementing these blocks can be found in Appendix C.

- The **information source** block providing a random bit-stream of 0's and 1's to the transmitter input.
- The **transmitter** block transforms the incoming bit stream to two outgoing streams of samples/symbol, one for the inphase channel (I-channel) and one for the quadrature channel (Q-channel).
- The **shaping transmit (Tx-) and receive (Rx-) filters** perform the filtering of the signal samples according to a desired spectrum shape. Nyquist $\sqrt{\alpha}$ raised-cosine filters are used

both at the transmitter output and at the receiver input.

- The **channel** block simulates the distortion imposed by the type of channel chosen. AWGN, as well as frequency nonselective Rayleigh and Ricean fading channel models were considered.
- The **noncoherent receiver** block implements an "integrate and dump" FM-discriminator based or a sampling-differential type of receiver, operating on signal samples from the channel output.
- The **receiver** block implements various detection algorithms using the receiver structures presented in Chapter 2.

It should be pointed out that, as is customary in computer simulation, in the system modeling in software, the baseband equivalent was used for all signals. According to this transformation, a modulated signal

$$s(t) = A\cos(2\pi f_c t + \phi) \tag{3.1}$$

with A denoting the amplitude of the signal, f_c the carrier frequency and ϕ carrier phase, has the baseband equivalent signal [2]

$$u(t) = A[\cos\phi + j\sin\phi] = Ae^{j\phi}\ . \tag{3.2}$$

The implementation details for the above functional blocks are presented next.

3.2.1. The Information Source Block

The source output is used as the input to the transmitter. Desirable features are the highest possible randomness in generating bits 0 and 1, i.e., getting a 0 or a 1 with probability as close as possible to 0.5. To implement this bit stream generator, a pseudo-random number generator existing in the system's C function library was used. This function returns numbers uniformly distributed in the interval [0,1.0). It uses the well known linear congruential formula

$$X_{n+1} = (aX_n + c) \bmod m\ , \quad n \geq 0 \tag{3.3}$$

with a and c constants defined in [47]. Using this formula, the generator's period is for all practical purposes "infinite"[5]. The modulus constant m is simply 2^{48}, providing a 48–bit result, treated as a double precision floating point number. The bit stream generator maps the two desired alphabet symbols, namely 0 and 1, on the two intervals resulting from the division of the initial output interval [0,1) to two equal subintervals: [0,0.5) and [0.5,1.0). Bit frequency tests performed demonstrated a probability ratio very close to the desired 0.5 even for small samples, e.g., for 4096 bits, 2045 0's and 2051 1's is quite typical.

3.2.2. The Transmitter Block

The baseband transmitters implemented fall into two general categories: a) uncoded and b) trellis-encoded, single- and multi-amplitude QPSK, using absolute phases or differential phase shifts ($\pi/4$–shift DQPSK). The signal phase of transmitters from the first category always conveys two information bits (one out of four possible phase changes) while the amplitude levels the rest. For the second, encoding is performed using a convolutional encoder with pre-compiled lookup tables. The tables provide a one-to-one mapping of convolutional encoder outputs to points on the two dimensional signal space. Examples of two codes, which are also used in this research, are the 4–state rate-1/2 $\pi/4$–shift DQPSK and the 8–state rate–2/3 $\pi/4$–shift 8–DQAM. Their corresponding signal-space and signal number assignment is illustrated in Fig. 3.2. Both convolutional codes shown were chosen since they are the best, i.e., give the best performance in AWGN, since they provide the maximum free Euclidean distance, for the code complexity considered [40].

---

[5] Strictly speaking, this formula using the constants defined in [47], provides pseudo-random numbers. Nevertheless, for all practical purposes, the period of the sequence of numbers produced can be regarded to be "infinite". For this reason, from now on, the uniformly distributed samples generated by this equation will be considered to be "random".

3.2.3. The Shaping Filters and the Filtering Operations

3.2.3.1. Transmit (Tx-) and Receive (Rx-) filters

In the context of software simulation modeling, the following two types of pulse shaping filters were employed [10]

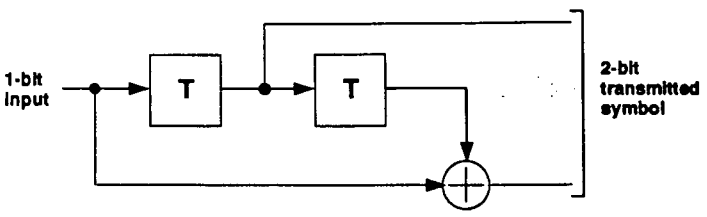

4-state convolutional encoder.

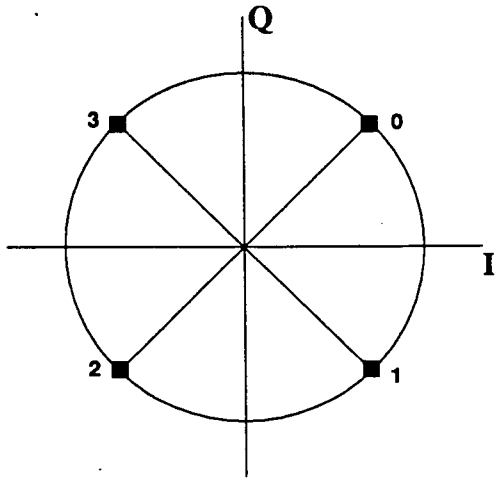

Mapping of transmitted symbols to differential phases.

(a) $\pi/4$-shift DQPSK.

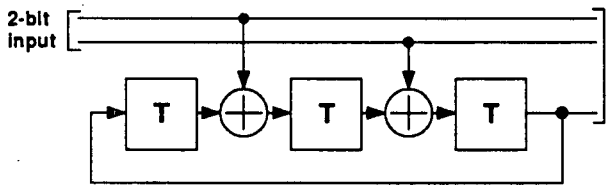

8-state convolutional encoder.

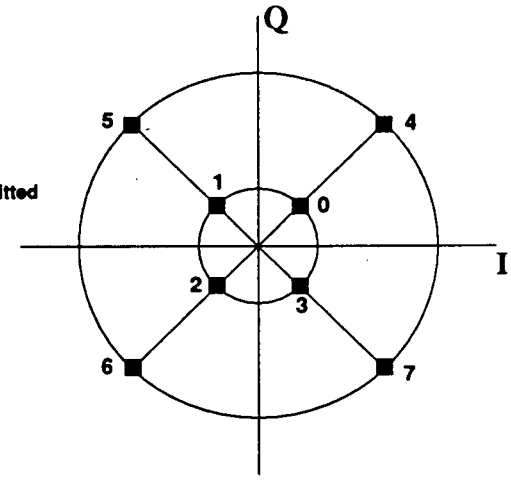

Mapping of transmitted symbols to differential phases & amplitudes.

(b) $\pi/4$-shift 8-DQAM.

Fig. 3.2. Signal mapping and constellation for (a) 4–state rate-1/2 $\pi/4$–shift DQPSK and (b) 8–state rate–2/3 $\pi/4$–shift 8–DQAM.

- The Transmit (Tx-) Filter $H_T(f)$, with

$$H(f) = \begin{cases} \frac{\pi T_s f}{\sin(\pi T_s f)} & 0 < |f| < (1-\alpha) f_N \\ \frac{\pi T_s f}{\sin(\pi T_s f)} \sqrt{\frac{1}{2}\left[1 - \sin\left\{\frac{\pi}{2\alpha}\left(\frac{f}{f_N} - 1\right)\right\}\right]} & (1-\alpha) f_N < |f| < (1+\alpha) f_N \\ 0 & \text{elsewhere.} \end{cases} \quad (3.4)$$

- The Receive (Rx-) Filter $H_R(f)$, with

$$H_T(f) = \begin{cases} 1 & 0 < |f| < (1-\alpha) f_N \\ \sqrt{\frac{1}{2}\left[1 - \sin\left\{\frac{\pi}{2\alpha}\left(\frac{f}{f_N} - 1\right)\right\}\right]} & (1-\alpha) f_N < |f| < (1+\alpha) f_N \\ 0 & \text{elsewhere.} \end{cases} \quad (3.5)$$

where $f_N = \frac{f_S}{2} = \frac{1}{2T_s}$ is the Nyquist frequency and α the filter roll-off factor taking values between 0 and 1.0.

Both filters are $\sqrt{\alpha}$ raised cosine filters with the Tx-filter having an amplitude equalizer so that their overall transfer function $H_T(f)H_R(f)$ satisfies Nyquist's first criterion for pulse transmission. This assumption was also used in Eq. 2.12. In addition, as well known, this split is optimum in the sense that, in an AWGN channel, it provides maximum signal-to-noise (SNR) ratio at the output of the Rx-filter [48].

3.2.3.2. The Filtering Operations

When computer simulation is employed, it is easier to realize the signal filtering operation in the frequency domain, rather than in the time domain. Furthermore, all signals and transfer functions must be represented by their discrete time domain and discrete frequency domain equivalents. If such a signal has a period, or equivalently for our purposes here symbol duration T, the parameter of interest is the number of samples per symbol duration, n_s. A continuous-time signal s(t) which is, say, a series of pulses, will be represented in the discrete-time domain, by the signal s$'(kT/n_s)$. Figure 3.3 is an example showing an unfiltered BPSK signal produced by the sequence 1011, in the discrete time domain, with $n_s = 4$.

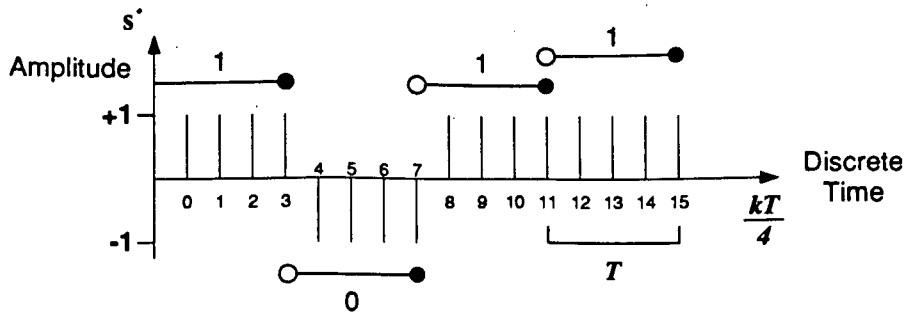

Fig. 3.3. Example of BPSK signal in the discrete time domain for the sequence 1011. The number of samples/symbol is 4.

The complex Fast Fourier Transform (FFT) [49] was used as the transformation algorithm between the discrete time domain and the discrete frequency domain. The FFT, as it is well known, is a discrete form of the Fourier series expansion and not the Fourier transform. However, if the sample size is sufficiently large, the results obtained are very close to the output from a Discrete Fourier Transform (DFT). The advantage presented by the FFT, as compared to the DFT, is that it is much faster due to its lower computational complexity.

The signal $s'(kT/n_s)$ is therefore transformed by means of an FFT, to $S'(kn_s/T)$ in the discrete frequency domain. Then, both real and imaginary parts of $S'(kn_s/T)$ are multiplied by the discrete-frequency equivalent of the desired filter transfer function, e.g., for $H_T(f)$, this is $H'(kn_s/T)$. Alternatively, an inverse FFT transformation yields the filtered discrete-time signal $s'(kT/n_s)$. In this process, the discrete frequency equivalents of the filter transfer functions (Eq. 3.4,3.5), i.e., $H'_T(kn_s/T)$ and $H'_R(kn_s/T)$ must be constructed. In doing so, the Nyquist frequency f_N must be calculated for the discrete frequency sample available. From Nyquist's sampling theorem it is well known that for a signal having spectral components up to frequency W, the sampling frequency must be at least 2W for no aliasing; note that this factor of 2 also implies 2 samples/(signal period) [2]. However, NRZ type of signals like the BPSK example of Fig. 3.3 do not have a finite bandwidth, making aliasing inevitable. Nevertheless, spectral components of the NRZ signal decrease rapidly in amplitude for higher frequencies [10]. This

in turn implies, that as n_s increases, the errors caused by aliasing will decrease. In order to perform the filtering operation in the discrete frequency domain, we have to calculate the index k_N into the array of discrete frequency components, corresponding to the Nyquist frequency f_N. For this purpose we define the **simulation bandwidth** as

$$\mathbf{B_s} \triangleq \frac{n_s}{T} = n_s f_s \tag{3.6}$$

where $T = \frac{1}{f_s}$ is the symbol duration and f_s denotes the Baudrate (or symbol rate). The simulation bandwidth corresponds to the entire discrete frequency sample provided by the FFT, so k_N is easily calculated by the following equation

$$k_N = \frac{f_N}{\mathbf{B}_s} N_s = \frac{f_s}{2\mathbf{B}_s} N_s = \frac{N_s}{2n_s} \tag{3.7}$$

with N_s denoting the total number of discrete frequency samples. Then, knowing that $N_s = n_s \mathrm{N}$, where N is the number of symbols transmitted, substituting in Eq. 3.7 we obtain:

$$k_N = \frac{\mathbf{N}}{2} \ . \tag{3.8}$$

Using this value which corresponds to the minimum Nyquist frequency f_N, the index of any other frequency desired can be easily calculated. As for a practical value for n_s, 16 was found to be a very satisfactory compromise between desired accuracy and required memory.

3.2.3.3. Examples of Typical Simulation Graphs

This subsection, presents the following three typical examples of plots generated by the developed computer simulation programs: 1) Filter transfer function, 2) eye-diagram and 3) state-space diagram.

In Fig. 3.4 the full raised cosine filter transfer function $H(f)$ is given for various values of α.

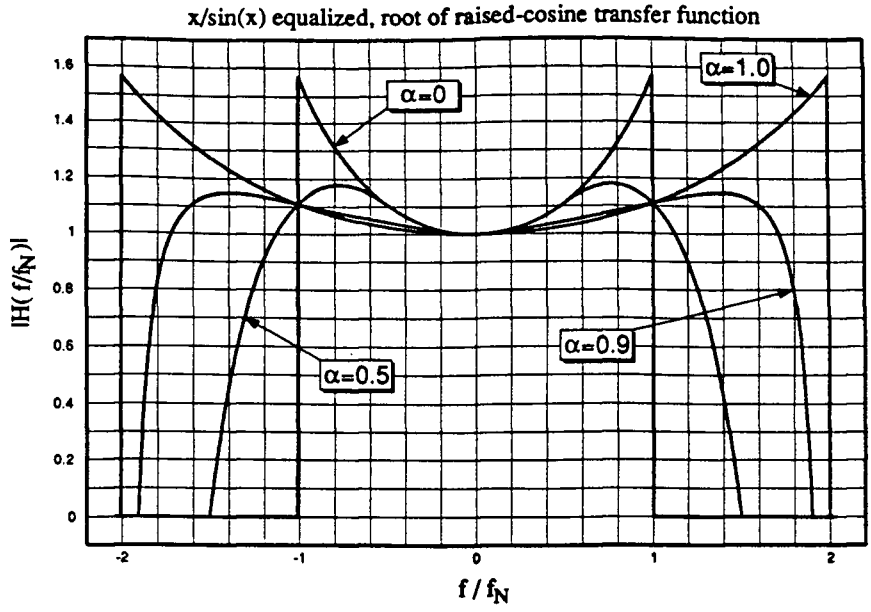

Fig. 3.4. Transfer function of cascaded transmit and receive filters for different values of the roll-off factor α.

In Fig. 3.5, the 2–symbol duration (i.e., $2T$) eye-diagram of a QPSK signal simulated by using the discrete-frequency filtering method described, is shown. The value used for the roll-off factor is 0.5. The two sampling instants are revealed by the points through which all signal trajectories pass. Notice that no inter-symbol interference (ISI) exists at the ideal sampling instant.

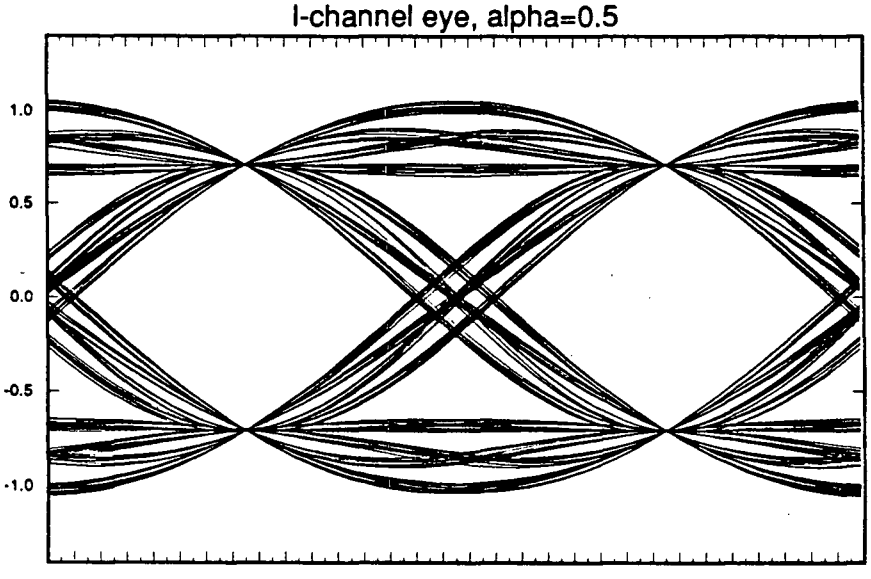

Fig. 3.5. The simulated 2–symbol eye-diagram for QPSK using roll-off factor $\alpha = 0.5$.

Finally, in Fig. 3.6, the baseband signal trajectories (state-space diagram) of a $\pi/4$–shift DQPSK system employing raised cosine filters of $\alpha = 0.5$ and $\alpha = 1.0$, are presented.

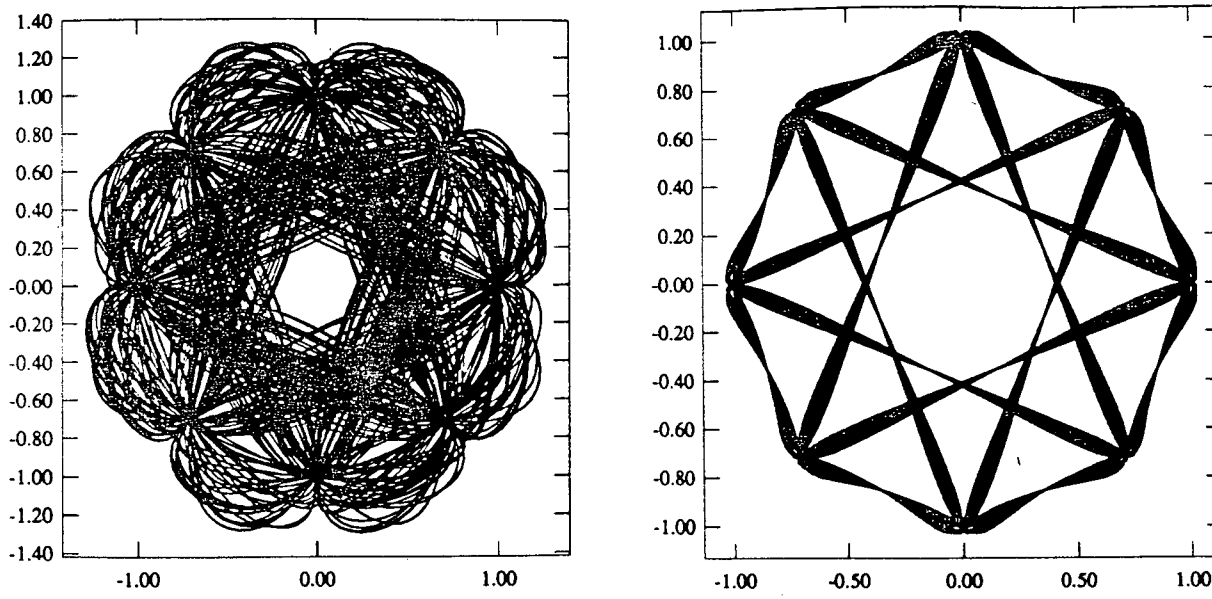

Fig. 3.6. Baseband signal trajectories of $\pi/4$–shift DQPSK for $\alpha = 0.5$ and $\alpha = 1.0$.

3.2.4. The Channel Block

As previously mentioned, the channel considered in this thesis is assumed to impose two types of interference: a) AWGN and b) multiplicative frequency nonselective Rayleigh or Ricean fading.

a) The white, i.e., uncorrelated, and Gaussian noise, which is also needed for simulating the fading interference, is generated by making use of the same C-library "random" number generator as in the case of the "random" information source. The uniformly distributed (i.e. "random") numbers are fed as input to a second routine which transforms their probability density function (PDF) into a Gaussian PDF. A commonly used method of performing this transformation, is by taking advantage of the Central Limit Theorem [8]. According to this theorem, a sufficiently large number of uniformly distributed samples (e.g., 12), can be added up in order to produce one Gaussian sample. This is quite straight forward to realize, but almost 10 times slower than another method which uses the Box-Muller method for producing

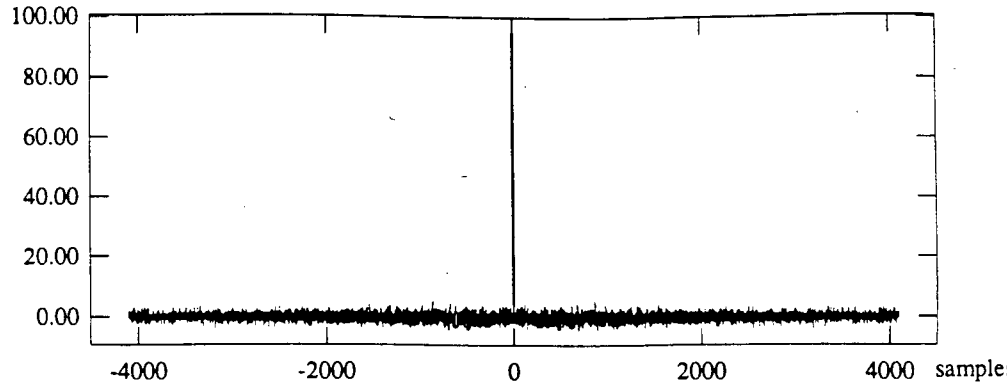

Fig. 3.7. Autocorrelation of 4096 Gaussian white noise samples; variance = 100.

2 Gaussian samples from 2 uniformly distributed numbers [49]. Both methods were first tested via the autocorrelation of the sequences they produced and yielded statistically identical results. A typical autocorrelation function showing the sufficiently high degree of randomness obtained even for small samples, is presented in Fig. 3.7. The noise samples were found to follow faithfully the Gaussian distribution function. This is clearly demonstrated in Fig. 3.8, where the cumulative probability distribution function (CPDF) of the computer simulated Gaussian noise is compared to the theoretical Gaussian CPDF. Verification of the software model for the Gaussian noise generator was also possible from the simulation of modulation schemes like QPSK, the

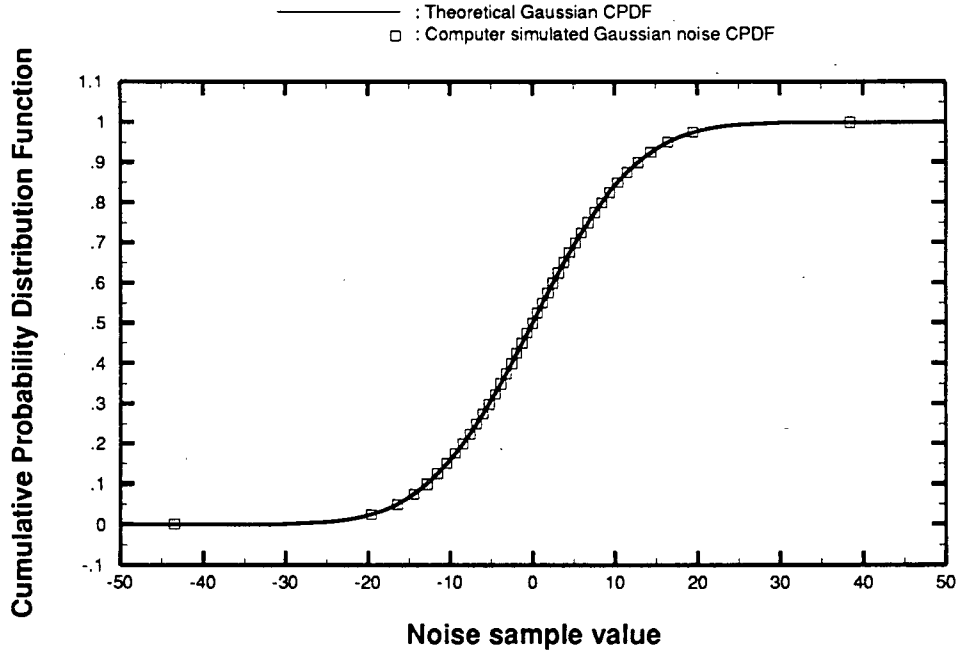

Fig. 3.8. Comparison of computer simulated noise CPDF to the Gaussian theoretical; variance = 100.

performance of which is well known in the AWGN channel. An excellent match of the simulated results to the theoretical curves expected (e.g., 0.6% away from the theoretical value for QPSK at E_b/N_0 = 7dB[6]), demonstrated that the simulated noise model presented the desired accuracy for all practical purposes. In the complex baseband model, AWGN interference corresponds to having two independent streams of noise samples added to corresponding transmitted inphase and quadrature signal components.

b) The frequency nonselective fading was modeled in baseband as a filtered complex Gaussian noise process. Following [5], a process with Rayleigh distributed envelope and uniformly distributed phase in $[-\pi,\pi)$ can be produced if we assume Gaussian samples for the inphase and quadrature signals in the two dimensional signal space. This complex noise process, which can be mathematically expressed as

$$f(t) = f^I(t) + jf^Q(t) \tag{3.9}$$

is essentially the baseband equivalent of a Rayleigh faded carrier signal. The real and imaginary part are generated by filtering two independent Gaussian noise processes $n^I(t)$ and $n^Q(t)$ with identical filters. The transfer function chosen for the filters determines the type of fading assumed. A table of several filter transfer functions together with corresponding fading autocorrelation functions can be found in [6]. As in Chapter 2, in the computer simulation, the uniform and land mobile fading models were also employed. Using the methodology described in [2], it is shown in Appendix A.4 that the baseband model for the faded signal is the complex multiplication of the baseband information signal

$$x(t) = x^I(t) + jx^Q(t) \tag{3.10}$$

---

[6] Here E_b denotes the energy per transmitted bit and N_0 the one-sided power spectral density (PSD) of the white Gaussian noise.

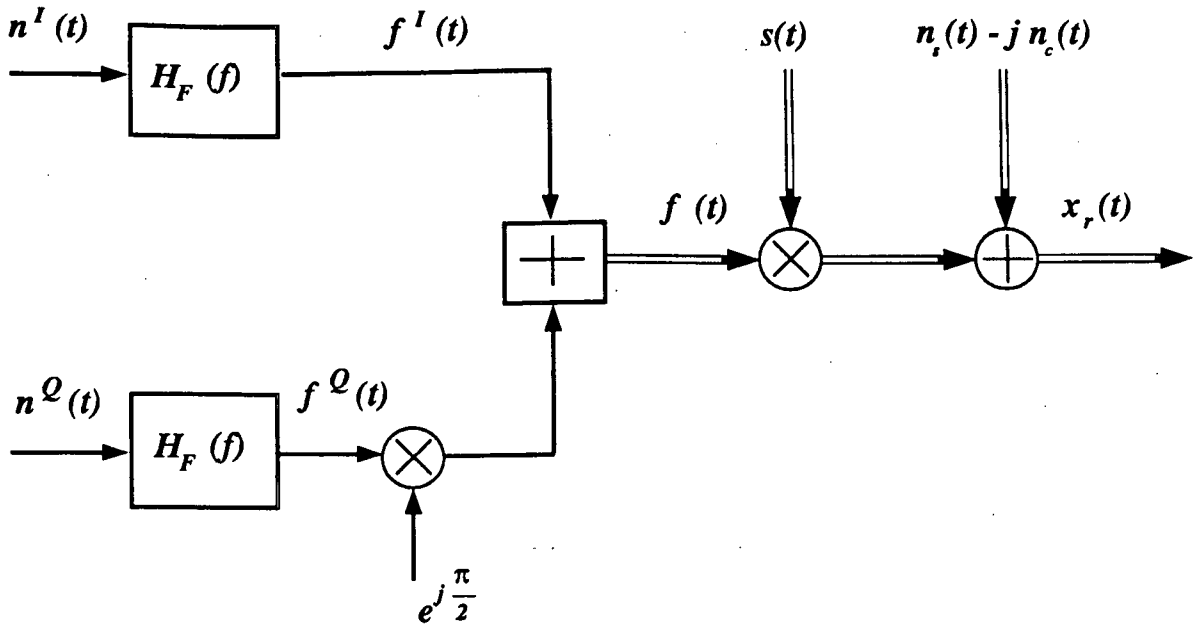

Fig. 3.9. The baseband Rayleigh fading and AWGN channel model; $s(t)$ represents the transmitted signal.

with the complex fading process $f(t)$. In other words, the received signal, corrupted by fading and AWGN can be expressed as

$$x_r(t) = s(t)f(t) + n_s(t) - jn_c(t) \tag{3.11}$$

which is illustrated in block diagram form in Fig. 3.9.

For the uniform fading model, the fading filter transfer function is

$$|H_F(f)|^2 = \begin{cases} \frac{1}{2B_F} & \text{for } 0 \le |f| \le B_F \\ 0 & \text{elsewhere} \end{cases} \tag{3.12}$$

whereas for the land mobile fading model

$$|H_F(f)|^2 = \begin{cases} \frac{1}{\sqrt{1-\left(\frac{f}{B_F}\right)^2}} & \text{for } 0 \le |f| \le B_F \\ 0 & \text{elsewhere .} \end{cases} \tag{3.13}$$

$B_F = v/\lambda$ is the maximum Doppler frequency (or fading bandwidth), with v denoting the vehicle speed and $\lambda = c/f_c$ the wavelength corresponding to the carrier frequency f_c used. Eq. 3.12 and 3.13 give the general form of the filter transfer function. The filter gain, which is not indicated, can be varied according to the desired filter output power, i.e., the desired power of the fading signal.

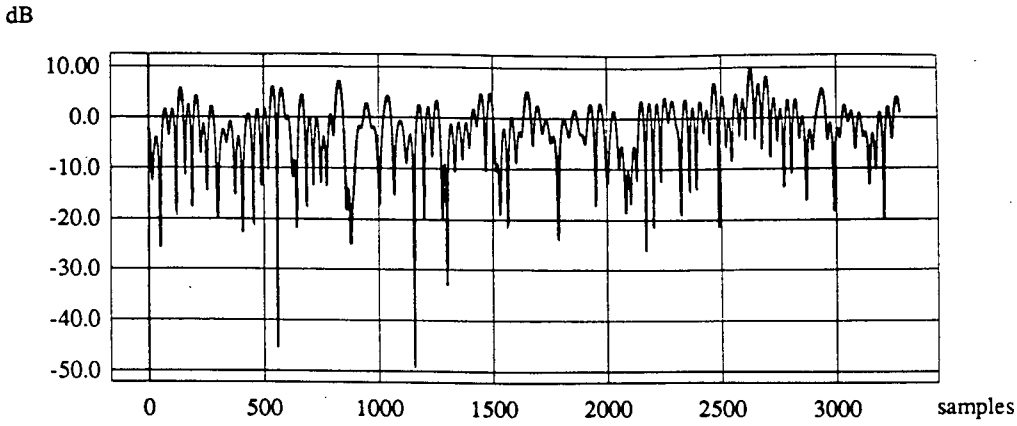

Fig. 3.10. Computer simulated amplitude of a faded carrier for the land mobile fading model.

The envelope $R(t)$ and phase $\theta(t)$ of $f(t)$ are given by

$$\begin{aligned} R(t) &= \sqrt{(f^I(t))^2 + (f^Q(t))^2} \quad , \\ \theta(t) &= \arctan\left(\frac{f^Q(t)}{f^I(t)}\right) \quad . \end{aligned} \tag{3.14}$$

A typical faded carrier amplitude, obtained by means of computer simulation is shown in Fig. 3.10. The model used to produce the data for this plot is that of land-mobile fading.

The statistical properties of the faded carrier samples produced by the computer simulation were verified by plotting the amplitude and phase CPDF's obtained, together with the theoretically expected. The results are depicted in Figs. 3.11 and 3.12. In Fig. 3.11, the curve plotted indicates the probability of the signal amplitude (envelope) being above the RMS value by as many dB as indicated on the x-axis. In the same figure, the Rayleigh theoretical CPDF is compared to the faded carrier envelope CPDF. The simulated faded carrier phase together with the theoretical CPDF for the uniform CPDF in the interval [$-\pi$,π) are plotted in Fig. 3.12.

The small deviation of the simulated values shown in Figs. 3.11 and 3.12, from the theoretical CPDFs, is due to the small number of signal samples used to generate these two plots. In the actual simulation runs the number of samples were typically 16 to 32 times more than the 8192 symbols $\times$ 16 samples/symbol used here.

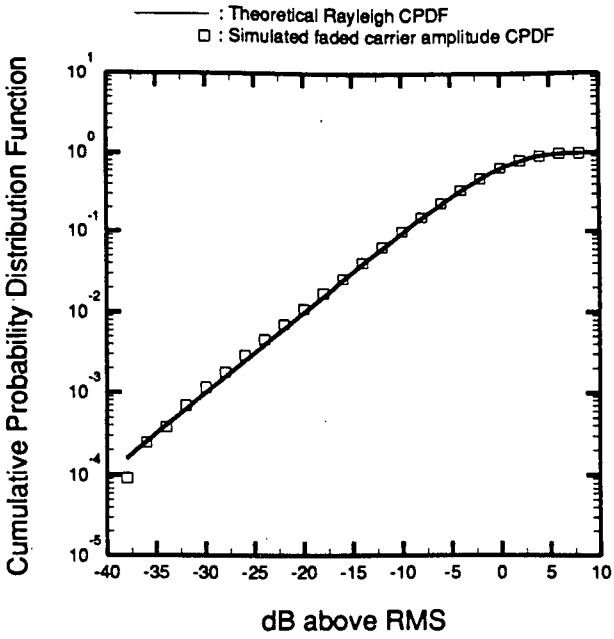

Fig. 3.11. The CPDF for the envelope of the computer simulated complex fading process $f(t)$. For comparison purposes, the theoretical curve has also been included.

As it is well known, the Ricean fading channel model is realized by simply adding the original undistorted signal to the Rayleigh faded signal [6]. This simulates the direct signal path between base station and mobile. A block diagram of the Ricean fading model is shown in Fig.

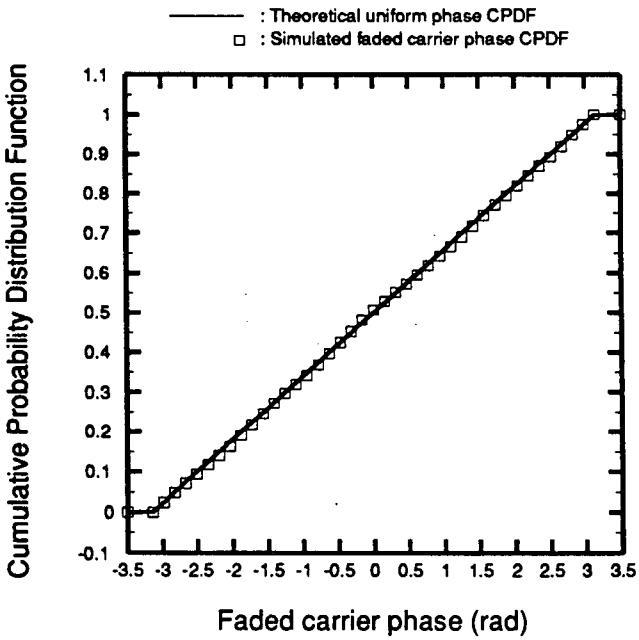

Fig. 3.12. Comparison of the simulated faded carrier phase CPDF to the theoretical curve.

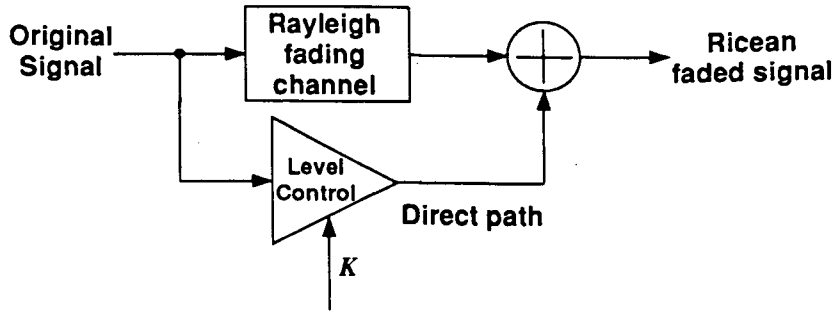

Fig. 3.13. The generalized block diagram of the Ricean fading channel.

3.13. The additional parameter for this type of fading is the ratio of the direct signal power to the power of the Rayleigh faded carrier, which is the previously discussed K–factor.

We conclude this subsection by mentioning that in the actual computer simulation, the Tx-filter, the channel and the Rx-filter were all coded into one BloSim star. The reason for this is the fact that a large number of signal samples had to be accumulated in the block implementing the filters before they could be processed. This in turn caused BloSim to grow it's FIFO Input/Output queues between blocks in such a way as to limit the memory available for processing large numbers of transmitted symbols. By lumping the three blocks together, memory space was saved and the overall execution speed was reduced.

3.2.5. The Noncoherent Receiver Block

As well known, noncoherent receivers can be classified into two major groups: a) the FM limiter/discriminator type, followed by an integrate-and-dump filter, and b) the differential detector type. The two techniques have been shown to be equivalent for the $\pi/4$–shift DQPSK system, in terms of BER performance [50]. For both types of receivers, an amplitude (envelope) limiter is employed before any phase operations so that the computation will not be affected by the fluctuating envelope. In the computer simulation, the operation of the limiter was realized in software by dividing the complex sample by it's magnitude, effectively limiting the signal envelope to a constant value, which without loss of generality, was assumed to be equal to 1.

3.2.5.1. The FM Limiter/Discriminator Receiver

The **FM-discriminator**–based noncoherent receiver uses a discriminator to obtain the instantaneous phase change of the carrier. This carrier phase derivative, is the input to the integrate-and-dump filter which computes the carrier phase change between two symbol intervals. Assuming perfect symbol timing recovery[7], the timing signal will cause a "dump" of the integrator output at the appropriate sampling instant, and will clear it to zero before the integration for the next symbol interval begins. As shown in Appendix A.5, the discriminator is modelled mathematically by the following equation [50]

$$\frac{\partial \phi(t)}{\partial t} = \frac{\partial y}{\partial t}x - \frac{\partial x}{\partial t}y \tag{3.15}$$

where x denotes the inphase signal and y the quadrature signal. However, in order to use it in the discrete-time computer simulation, an equivalent discrete-time model must be obtained. The two time derivatives can be approximated by using any one of the well known formulas from numerical analysis. In our case, the forward reference formula [51] was used

$$\frac{\partial \phi(t)}{\partial t} \simeq \frac{\phi(t+h) - \phi(t)}{h} \quad . \tag{3.16}$$

The smaller the step h the better the approximation. Using this approximation, Eq. 3.15 becomes

$$\Delta\phi(k) = \Delta y(k) \cdot x(k-1) - \Delta x(k) \cdot y(k-1) \tag{3.17}$$

where k denotes the discrete time variable. Since $\Delta\phi(k) = \phi(k) - \phi(k-1)$, $\Delta y(k) = y(k) - y(k-1)$ and $\Delta x(k) = x(k) - x(k-1)$, Eq. 3.17 yields

$$\phi(k) = \phi(k-1) + [y(k) - y(k-1)] \cdot x(k-1) - [x(k) - x(k-1)] \cdot y(k-1) \tag{3.18}$$

---

[7] As previously mentioned, the problem of obtaining symbol synchronization in a fading channel is not addressed by the research work reported in this thesis.

The discrete time step h which determines the approximation accuracy, depends on the number of samples/(symbol interval) n_s. A typical output, for the $\pi/4$–shift DQPSK system, from the simulated integrate-and-dump receiver block is shown in Fig. 3.14, clearly demonstrating the four possible carrier phase changes. During the simulation runs it was observed that less than 32 samples per symbol yield great inaccuracy at BER levels below 10^{-3}. This relatively large number of samples required limits the maximum number of transmitted symbols filtered in an FFT window due to limited computer memory. This is the most serious disadvantage of this model and it is why the second type — the differential detector — was used instead.

3.2.5.2. The Differential Detector Receiver

The **differential detector** computes the phase change between symbols by operating on samples from the inphase and quadrature channels. Using the same notation as in Eq. 3.17 and 3.18, we can write the output from the envelope limiter as

$$x(n) = \cos[\phi(n) + \theta] \text{ and } y(n) = \sin[\phi(n) + \theta] \tag{3.19}$$

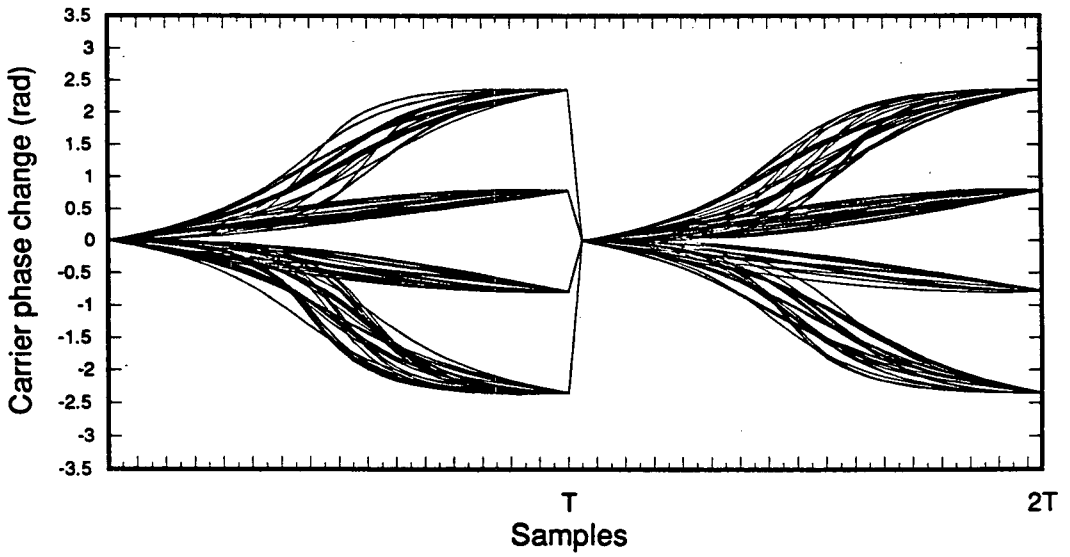

Fig. 3.14. Integrate-and-dump output for 256 symbols transmitted.

where θ is the carrier initial phase. Then, the phase change between two symbol interval can be calculated by the following two formulas

$$W(n) = x(n)x(n-1) + y(n)y(n-1) = \cos[\phi(n) - \phi(n-1)]$$
$$Z(n) = y(n)x(n-1) - x(n)y(n-1) = \sin[\phi(n) - \phi(n-1)] \ . \tag{3.20}$$

Clearly, $W(n)$ and $Z(n)$ are equivalent to the baseband inphase and quadrature components of a coherently demodulated QPSK signal. This implementation of noncoherent detection does not present the inaccuracies inherent to the approximation of the phase derivative found in the model for the FM-discriminator, and thus it was employed in our computer simulation model.

3.2.5.3. BER Computer Simulation Results

Actual computer simulation data obtained for both receiver models demonstrated their equivalence in terms of BER performance. The computer simulated BER performance of the uncoded QPSK modulation scheme, using a coherent maximum likelihood detector, for different values of the Nyquist filter roll-off factor α, is presented in Fig. 3.15. As it is evident from this figure, the match of the simulation data to the theoretical values is excellent, presenting only minor deviations (up to approx. 5% in the worst case) at an E_b/N_0 of 10 dB. The reason for this is that the number of bits in error counted at these values of E_b/N_0, is considerably smaller (e.g., less than 10) than that counted for lower E_b/N_0 (e.g., more than 100). However, the minimum acceptable number of error occurrences during all computer simulation runs was kept at least 100. At a BER equal to 10^{-4} this translates into a confidence interval of a factor of about 20% on the BER [52], which results in negligible uncertainty on the E_b/N_0 scale.

The simulation results for the noncoherent $\pi/4$–shift DQPSK scheme, using the differential detector described previously, for the same values of α as in Fig. 3.15, are presented in Fig 3.16. Theoretical values used for comparison were obtained from [53]. As in the case for QPSK, the maximum deviation from the theoretically expected appears at the high E_b/N_0 end, being again in the worst case around 5%. The computer simulation results presented both in Fig. 3.15 and

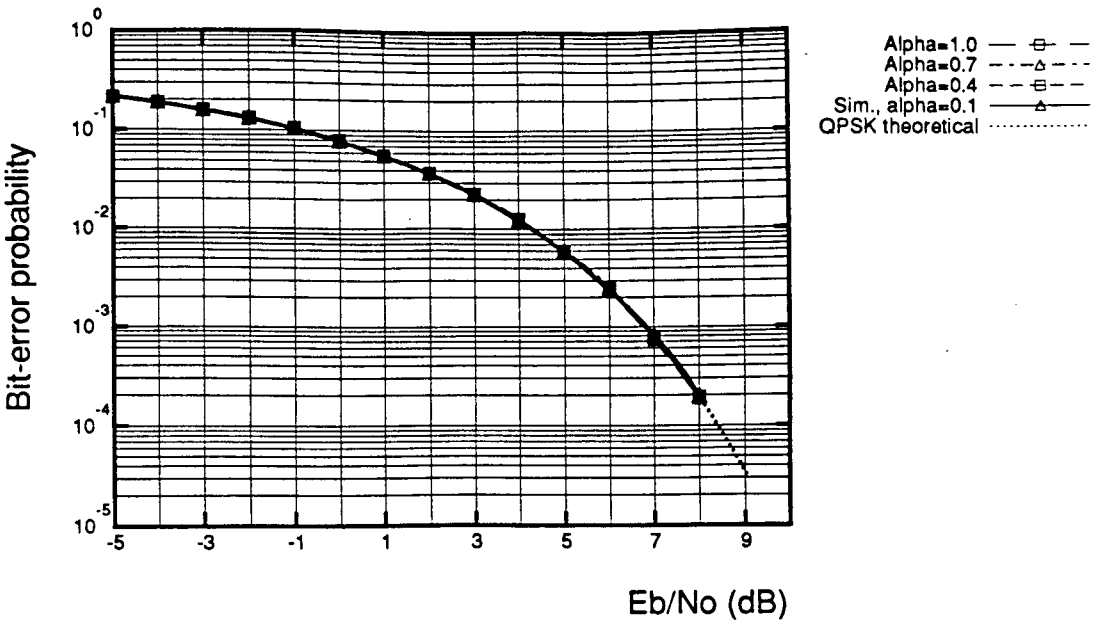

Fig. 3.15. Theoretical and simulated BER performance of coherently detected QPSK in AWGN. Nyquist filters with $\alpha = 0.1, 0.4, 0.7, 1.0$ are employed.

Fig 3.16 also prove the accuracy of the software model of the AWGN channel, and especially that of the white Gaussian noise generator block.

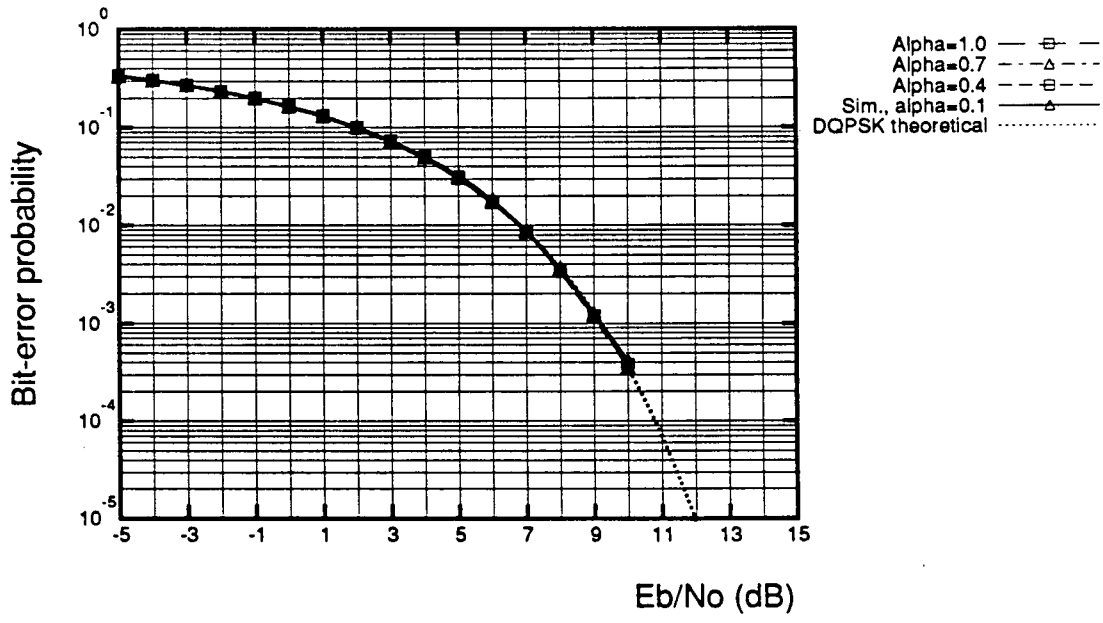

Fig. 3.16. Theoretical and simulated BER performance of $\pi/4$–shift DQPSK in AWGN. Nyquist filters with $\alpha = 0.1, 0.4, 0.7, 1.0$ are employed.

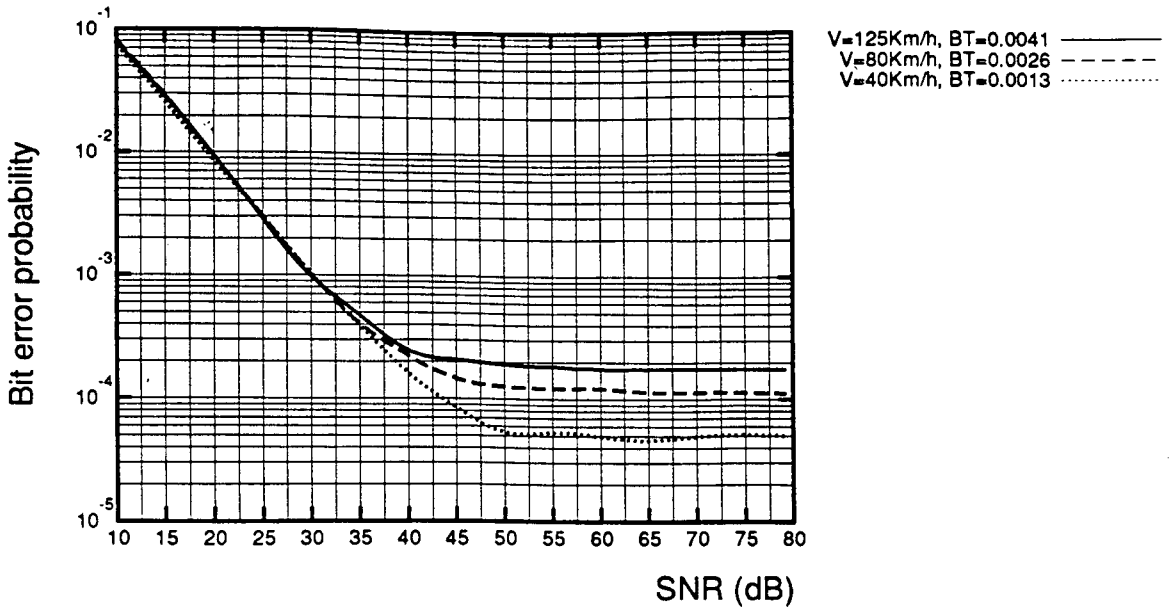

Fig. 3.17. BER of differentially detected $\pi/4$–shift DQPSK in flat Rayleigh fading. Nyquist filter $\alpha = 0.2$, BT = $B_F T$.

The BER performance of the noncoherent $\pi/4$–shift DQPSK scheme employing the differential detector receiver, as a function of the signal to noise ratio (SNR), in frequency-flat Rayleigh and Ricean fading channel conditions was also obtained via computer simulation. The obtained BER results with $B_F T$ and α as parameters, are summarized in Fig. 3.17 – 3.20.

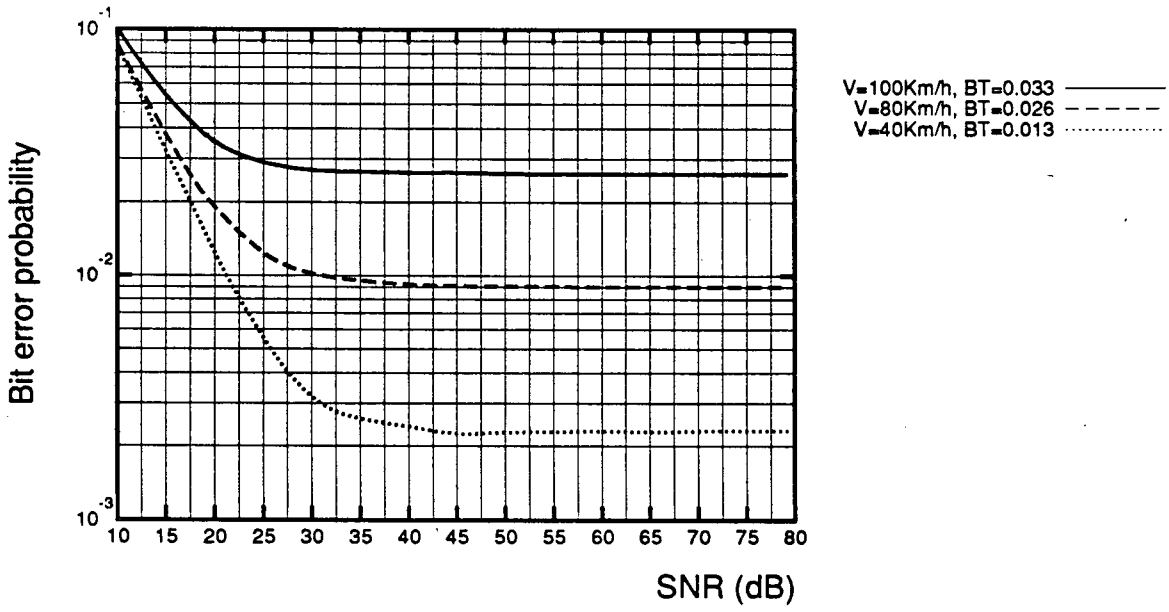

Fig. 3.18. Differential detector in flat Rayleigh fading. Nyquist filter $\alpha = 0.2$, BT = $B_F T$.

In Fig. 3.17, the performance of a $\pi/4$–shift DQPSK system employing raised cosine filters of $\alpha = 0.2$ and for $B_F T$ products of 0.0013, 0.0026 and 0.0041 is presented. The presence of error floors is evident. Theoretical results in [54] verify the accuracy of our computer simulation results.

From Fig.3.18, it can be seen clearly, that higher $B_F T$ products will result in higher error floors. On the other hand, different values of α do not seem to have any significant impact on the overall system performance. For example, by comparing Fig. 3.18 ($a = 0.2$) and 3.19 ($a = 0.35$), the BER results are almost identical for the same $B_F T$ product. The explanation for this is that the considered fading signal bandwidth B_F is much smaller than the filter's Nyquist frequency and thus the fading characteristic does not change.

Finally, in Fig. 3.20, the performance of an $\alpha = 0.2$ $\pi/4$–shift DQPSK system with differential detector, operated in a Ricean fading channel is illustrated. As expected, the BER performance for $K_{\mathrm{dB}} = 10$ dB is significantly better than that for $K_{\mathrm{dB}} = 0$ dB.

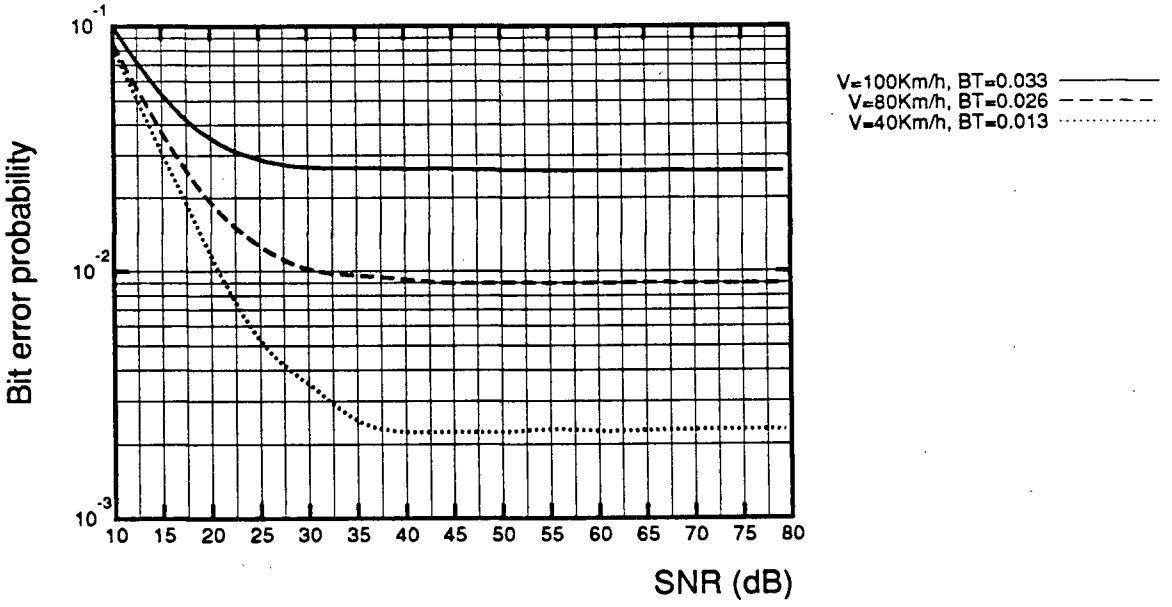

Fig. 3.19. Differential detector in flat Rayleigh fading. Nyquist filter $\alpha = 0.35$, BT = $B_F T$.

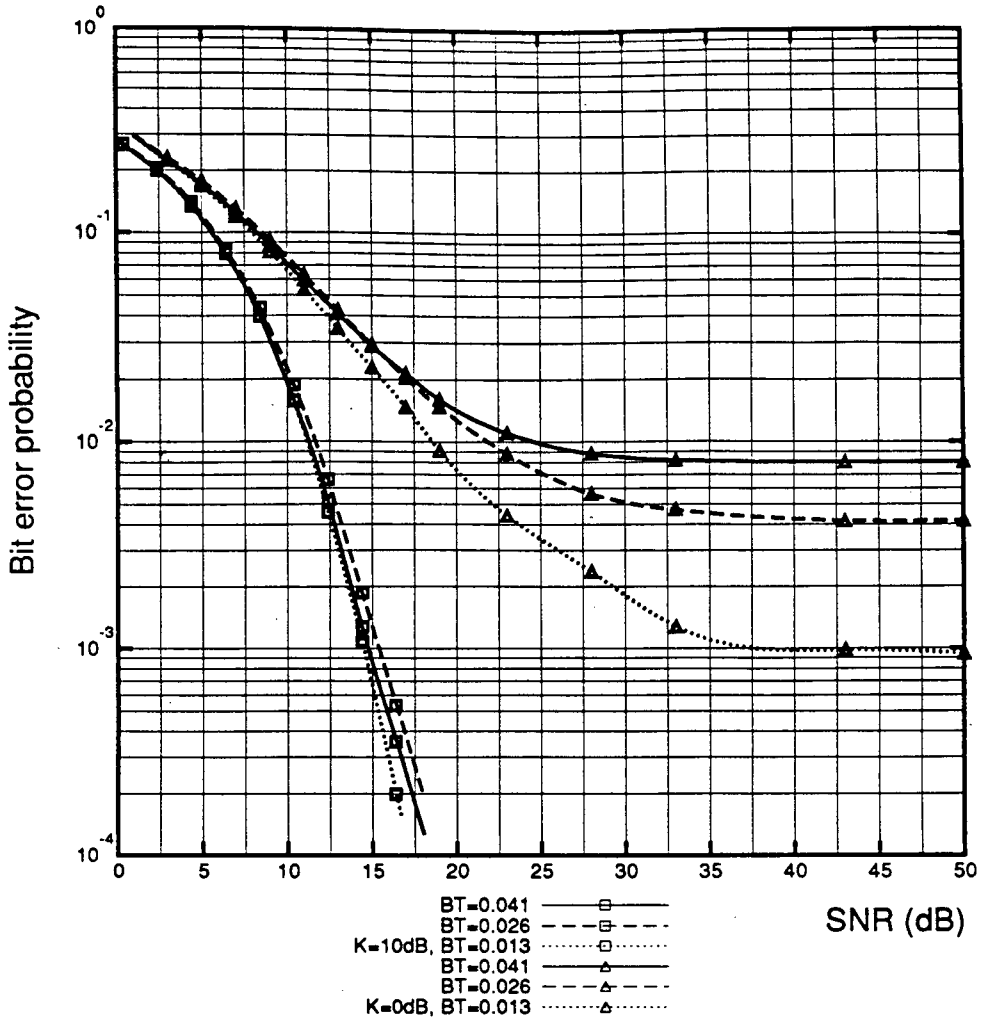

Fig. 3.20. BER of differentially detected $\pi/4$–shift DQPSK in flat Ricean fading. Nyquist filter $\alpha = 0.2$, BT = $B_F T$.

3.2.6. The Receiver Block

The receiver structures derived in Chapter 2 were used in both coded and uncoded digital modulation schemes. The following is a detailed description for the application of the proposed algorithms, implemented in a way that any coded or uncoded PSK or QAM signal constellation can be accommodated. It should be pointed out that the algorithms derived for simulating this particular receiver, were used almost without any alteration for the digital modem implemented in hardware.

3.2.6.1. Coded Version of the Receiver

As presented in Chapter 2, the general form of the quantity to be minimized by the derived optimal algorithm, was given in Eq. 2.23 and for the reader's convenience is repeated here

$$\sum_{k=1}^{L} \frac{1}{\sigma_k^2} \left\{ \left[\frac{\mathrm{Re}\{y_k c_k^* e^{-j\rho}\}}{|c_k|^2} - \sum_{i=1}^{k} p_{k,i} \left(\frac{\mathrm{Re}\{y_{k-i} c_{k-i}^* e^{-j\rho}\}}{|c_{k-i}|^2} - \overline{f^I} \right) - \overline{f^I} \left(1 - \sum_{i=1}^{k} p_{k,i} \right) \right]^2 + \right. \\ \left. + \left[\frac{\mathrm{Im}\{y_k c_k^* e^{-j\rho}\}}{|c_k|^2} - \sum_{i=1}^{k} p_{k,i} \frac{\mathrm{Im}\{y_{k-i} c_{k-i}^* e^{-j\rho}\}}{|c_{k-i}|^2} \right]^2 \right\} \quad (3.21)$$

where L represents the number of symbols transmitted, σ_k^2 the minimum mean square prediction error of order k, y_k the complex received signal sample at $t = kT$, c_k the complex signal being transmitted, ρ the initial phase of the transmitter carrier and $p_{k,i}$ the prediction coefficients of order k. In a receiver implementing sequential decoding, a decoded symbol is output at every symbol interval[8]. However, a delay of several symbols exists in the decoder which is primarily a function of the constraint length of the convolutional code used. No beginning and end exists for the information stream, since no packetization is performed at this low system level. Consequently, the outer sum from 0 to L in Eq. 3.21 has no practical meaning for the implementation of the algorithm. In practice, the metric can be kept minimum by maintaining an **accumulated metric** which is updated as every new signal sample is received. This is the same technique used by Viterbi sequential decoders. Furthermore, the prediction order used, typically does not have to be greater that 4, since it turns out that increasing it further, results in negligible performance improvement. Hence, the truncated version of the algorithm, as derived in Eq. 2.32, should be used for calculating the accumulated metric. Again for the reader's convenience, it is repeated here

---

[8] It should be pointed out that there is a fixed decoding delay of 5–6 times the code constraint length.

$$\frac{1}{\sigma_z^2}\left\{\left[\frac{\mathrm{Re}\{y_k c_k^* e^{-j\rho}\}}{|c_k|^2} - \sum_{i=1}^{z} p_{z,i}\left(\frac{\mathrm{Re}\{y_{k-i} c_{k-i}^* e^{-j\rho}\}}{|c_{k-i}|^2} - \overline{f^I}\right) - \overline{f^I}\left(1 - \sum_{i=1}^{z} p_{z,i}\right)\right]^2 + \right.$$
$$\left. + \left[\frac{\mathrm{Im}\{y_k c_k^* e^{-j\rho}\}}{|c_k|^2} - \sum_{i=1}^{z} p_{z,i}\frac{\mathrm{Im}\{y_{k-i} c_{k-i}^* e^{-j\rho}\}}{|c_{k-i}|^2}\right]^2\right\} \qquad (3.22)$$

where z is the prediction order used.

The metric described by Eq. 3.22 has to be minimized over all possible combinations of the transmitted symbols c_k. As it will be explained shortly, this can be accomplished by constructing a trellis structure on the receiver end, different from the one used by the convolutional encoder at the transmitter. From now on, this special trellis decoder will be referred to as **super-trellis**, it's states as **super-states** and the signals associated to it's branches **super-signals**[9]. Clearly, the number of combinations of trellis transitions and associated signals depends on the number of states in the original trellis, as well as it's structure in terms of state connectivity.

It is not difficult to recognize from the bracketed portion of Eq. 3.22 that the decoder operates on a sliding window of z past samples plus the current one. This implies that all combinations of possible transmitted symbols $c_k, c_{k-1}, ..., c_{k-z}$ must be tested. Each combination yields a branch (or transition) metric which added to the accumulated metric of every originating super-state, will yield the surviving transition to every merging super-state. The state presenting the minimum accumulated metric will be the origin for the decoding trace-back, as in the well known Viterbi decoding algorithm. Furthermore, it can be seen that the super trellis is generated from the branches of the original trellis code that exist between $z+2$ trellis nodes. The following example describes the steps involved in the derivation of the super-trellis structure for the simple 4–state trellis code illustrated in Fig. 3.21, for a prediction order of 1, i.e., $z = 1$. The code and signal phase assignment shown were used to test trellis coded 1/2–rate $\pi/4$–shift DQPSK using the proposed algorithm. For $z = 1$, the number of nodes required from the original

[9] For simplicity purposes, only trellis codes with no parallel branches are considered here. However, the super-trellis generation procedure can be extended to accommodate trellis codes with multiple branch transitions.

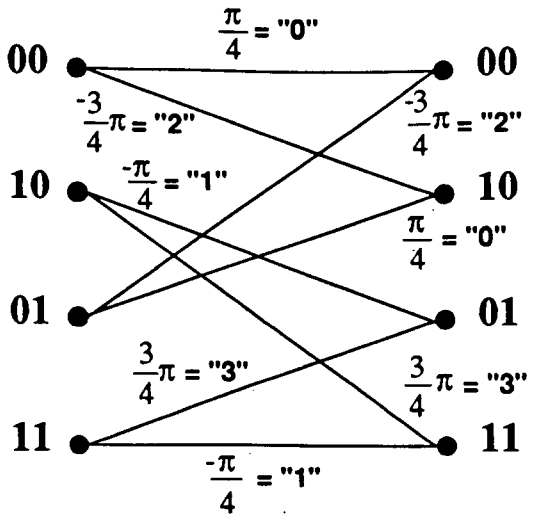

Fig. 3.21. Original 4–state trellis with signal numbers used as branch labels.

trellis structure is 3. The trellis with signal numbers assigned on each branch is presented in Fig. 3.22. The transition from state 0 to state 0 and then state 2 shown in Fig. 3.22, will yield the following on the super-trellis

- an originating super-state described by the combination of states on the first and second node, i.e., state 0 and state 0. A very convenient way to represent this combination is by regarding the two state numbers as the two digits of a base-4 integer (because of the 4 possible states). The convention that will be followed with regards to digit significance is the same for state and signal combinations: least significant digit to most significant digit, as

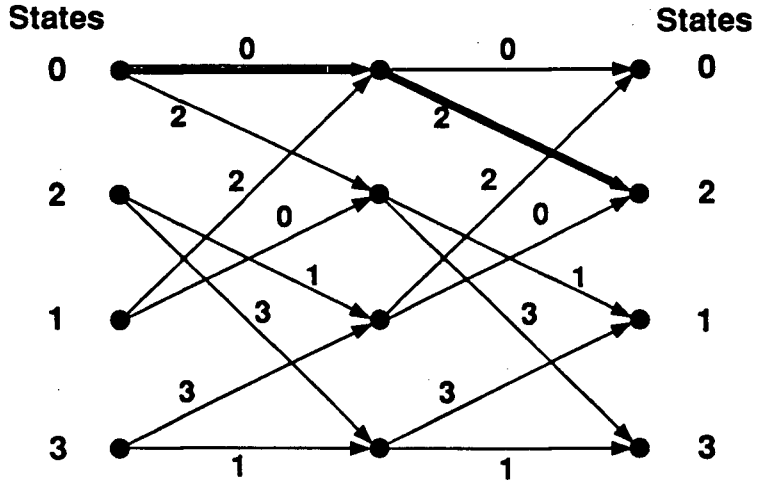

Fig. 3.22. Super-trellis generation for the 4–state code of Fig. 3.21 and $z = 1$.

we go from the left side of the trellis in Fig. 3.22, to the right side. Hence the originating state will have the number $(00)_4$.

- a merging super-state, described by the combination of states on the second and third node of the original trellis, having the number $(20)_4$ and
- a branch pseudo-signal (super signal) having the number $(20)_4$. The base is 4 because of 4 possible signals (actually signal phases) on the constellation used.

The rest of the super-trellis transitions with accompanying super-signals are constructed by following exactly the same procedure, yielding the trellis structure shown in Fig. 3.23.

It should be pointed out here, that the only difference between noncoherent schemes and coherent schemes, is that for the former, the signals assigned to the trellis branches represent *phase changes* (and possibly amplitudes), while for the latter the signals correspond to *absolute phases* (and possibly amplitudes). Hence, for example, the code of Fig. 3.21 together with the associated super-trellis of Fig. 3.23, can also be used for rate–1/2 coherent QPSK, in this particular case with the same signal assignment and numbering convention. As demonstrated by this relatively simple example, construction of the super-trellis can be very complicated, especially for higher complexity codes, constellations with large number of signals and/or large numbers for the z parameter (e.g., 3 or 4). For this reason, a recursive algorithm was derived and implemented in software, which constructs the super-trellis by tracing possible paths on the original trellis for z symbol intervals in the past. Connections between super-trellis nodes and super-signals associated to branches, are stored in tables. This recursive algorithm, given an original trellis code and a maximum prediction order, constructs all necessary tables at initialization time.

The notation used for the super-signals, i.e., numbering by using as base the number of signals on the constellation, is of particular importance when dealing with multi-amplitude schemes. As pointed out in Chapter 2 (see Eq. 2.26), when the signal mapping uses multi-

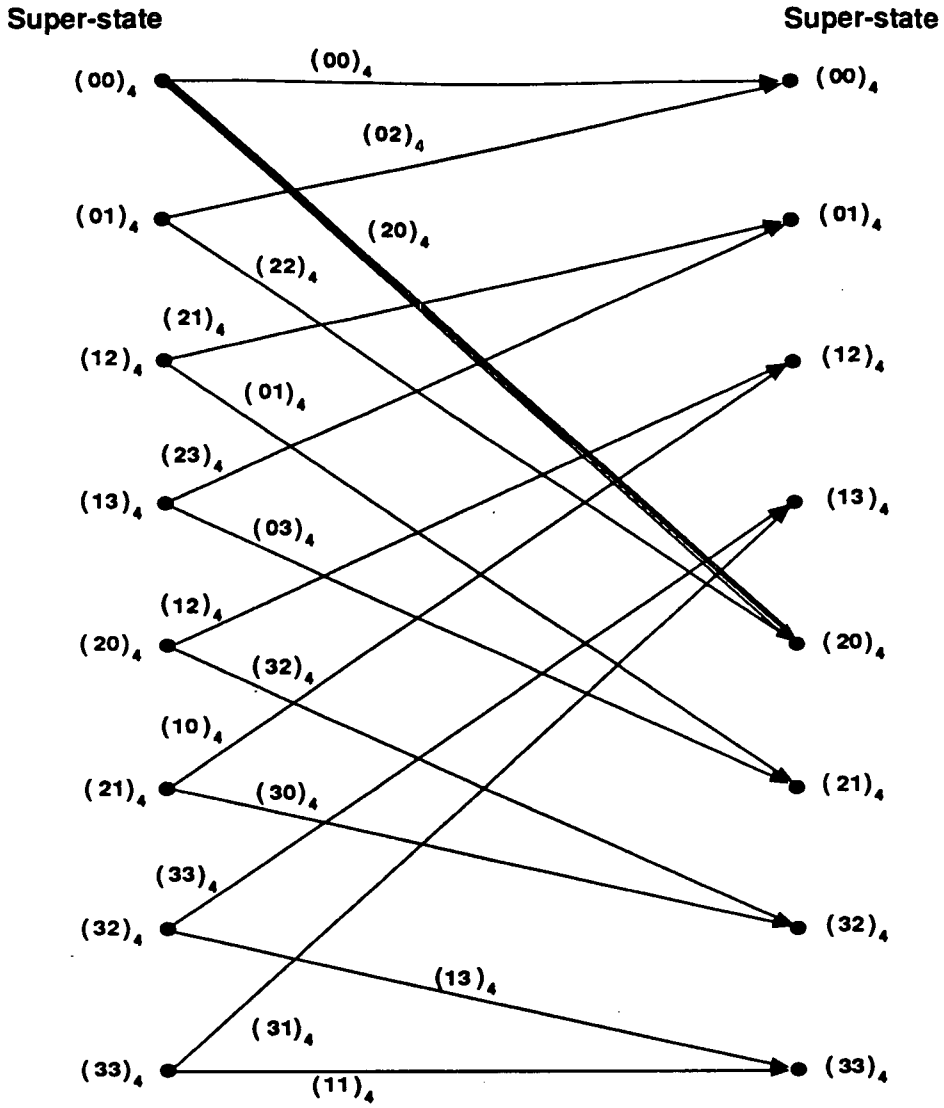

Fig. 3.23. The super-trellis for the 4–state code described in Fig. 3.21, for the case of $z = 1$. Note that both super-state and super-signal numbers are integers of base 4.

amplitude signals, the prediction coefficients become dependent on the transmitted sequence. In fact, it is not difficult to realize that, the number of transmitted symbol combinations used for this computation is equal to (Number of signals)^z. The prediction coefficients for every one of these combinations can be calculated at initialization time and tabulated in such a way that the super-signal number can be used directly as a row-index into the table. A column index can then return any one of z required coefficients. The C-language code has been implemented in such a general way, that any signal mapping using any convolutional code can be readily

accommodated by simply initializing constellation- and trellis-specific tables.

3.2.6.2. Uncoded Version of the Receiver

From the branch metric used for trellis decoding, defined by Eq. 3.22, we can see that the algorithm itself does not necessarily imply the use of a convolutional code. This observation inspired the application of this fading-resistive technique to the uncoded, single-level $\pi/4$–shift DQPSK. Clearly, without coding and associated trellis, any signal becomes a possibility for the next symbol interval. Thus, all combinations of phase transitions for z symbol intervals in the past, namely $c_k, c_{k-1}, ..., c_{k-z}$, must be tested. The accumulated metrics now are not associated to any super-states but to the signal combinations themselves, and the decoding delay is z symbols, the maximum order of prediction used.

3.3. BER Performance Evaluation Results

In this section, BER performance evaluation results for both trellis-coded and uncoded modulation schemes using the proposed algorithms will be presented. All the results are obtained by means of computer simulation software, which was described in Section 3.2.

3.3.1. Coded Schemes

The codes and signal constellations used for both coherent and noncoherent coded schemes are the ones appearing in Fig. 3.2. For the coherent schemes, the absolute phases shown in Fig. 3.2 are transmitted instead of phase differences, as is the case for the noncoherent schemes. Fig. 3.24 shows the BER performance of 4–state trellis-coded QPSK, and Fig. 3.25 the performance of 4–state $\pi/4$–shift DQPSK, both operated in a Rayleigh fast-fading ($B_F T = 0.125$) channel, with prediction orders $z = 2, 3$ and 4. The fading model assumed is the uniform fading model described by Eq. 3.12. The employed filters were raised cosine filters with $\alpha = 1.0$. The BER results for both systems, clearly indicate that even for $z = 2$, the error floor caused by fading

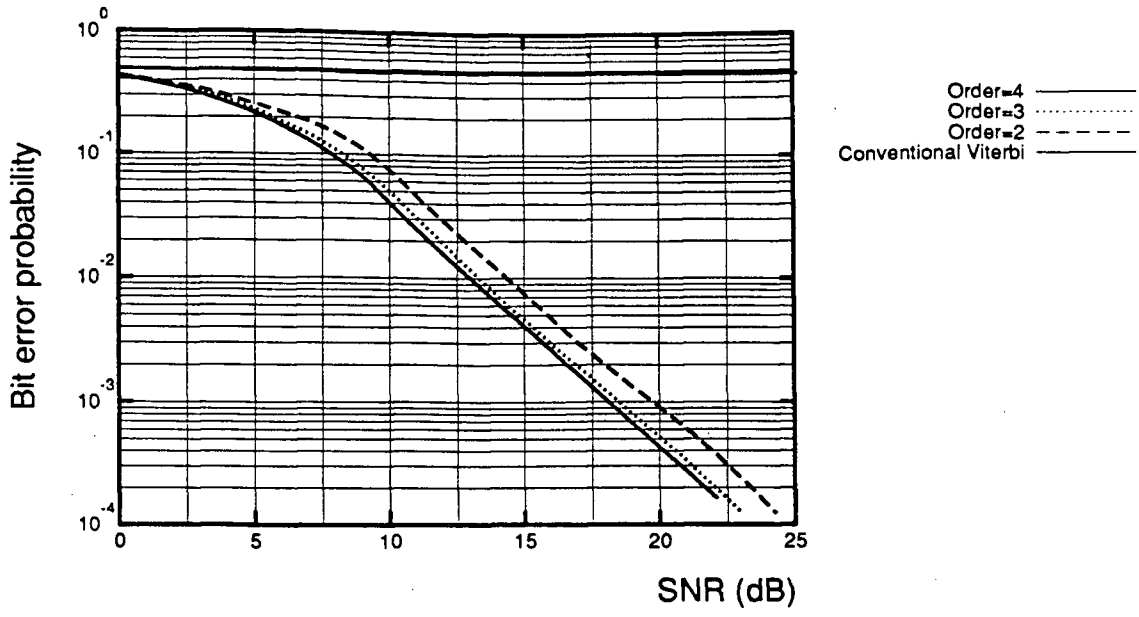

Fig. 3.24. BER of 4–state QPSK in flat Rayleigh fading (uniform model). Nyquist filter $\alpha = 0.35$, $B_F T = 0.125$.

is below 10^{-4}. Furthermore, it can be seen that, the improvement in performance is very small, beyond some value of the prediction order z (in this case beyond $z = 4$).

Fig. 3.24 also demonstrates the complete failure of the Viterbi decoder using Euclidean distances as a metric. Figs. 3.26 and 3.27 present the BER performance of rate–1/2 4–state

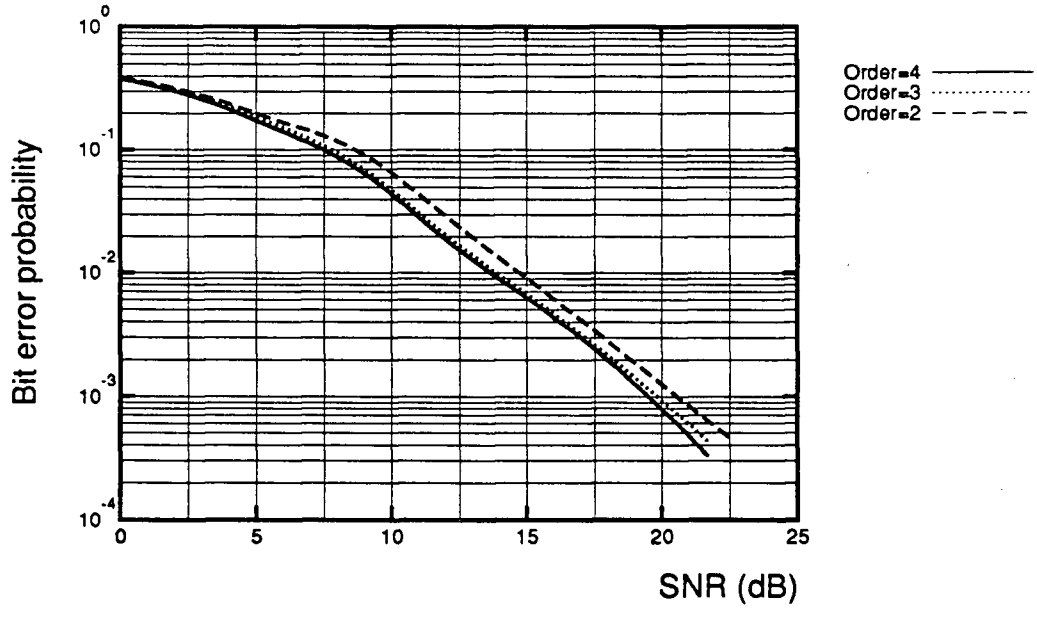

Fig. 3.25. BER of 4–state $\pi/4$–shift DQPSK in flat Rayleigh fading (uniform model). Nyquist filter $\alpha = 0.35$, $B_F T = 0.125$.

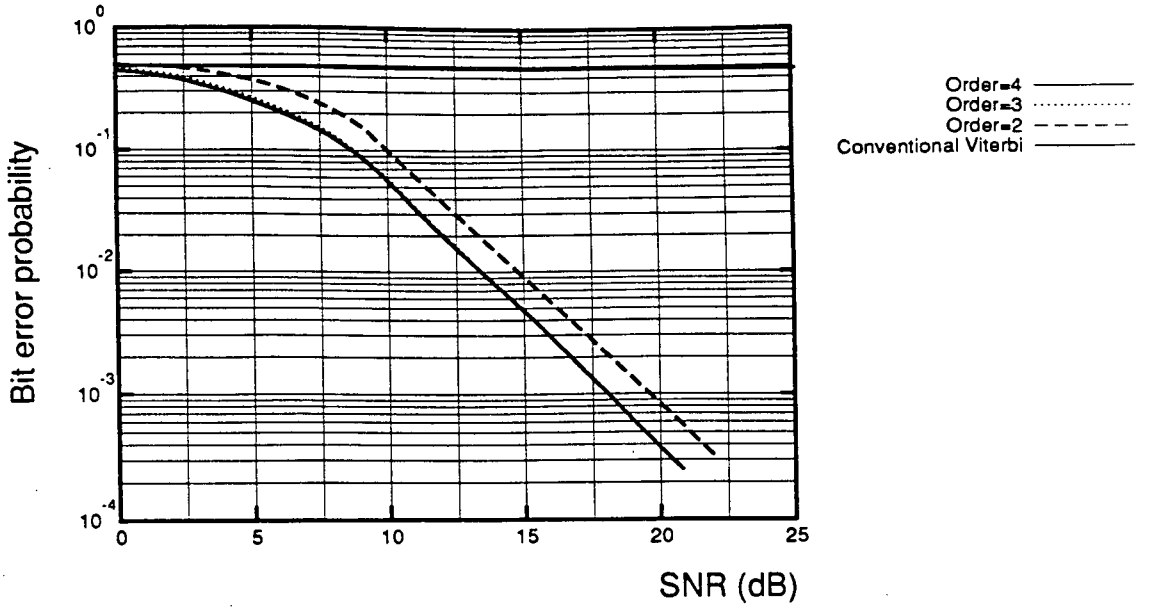

Fig. 3.26. BER of 4–state QPSK in flat Rayleigh fading (land mobile model). Nyquist filter $\alpha = 1.0$, $B_F T = 0.125$.

QPSK employing raised cosine filters of $\alpha = 1.0$ and 0.35. Here, the land mobile fading channel was used, with $B_F T = 0.125$. Comparing the results of Figs. Figs. 3.26 and 3.27, it can be seen that the system with $\alpha = 1.0$ performs marginally better (at higher SNR) as compared to

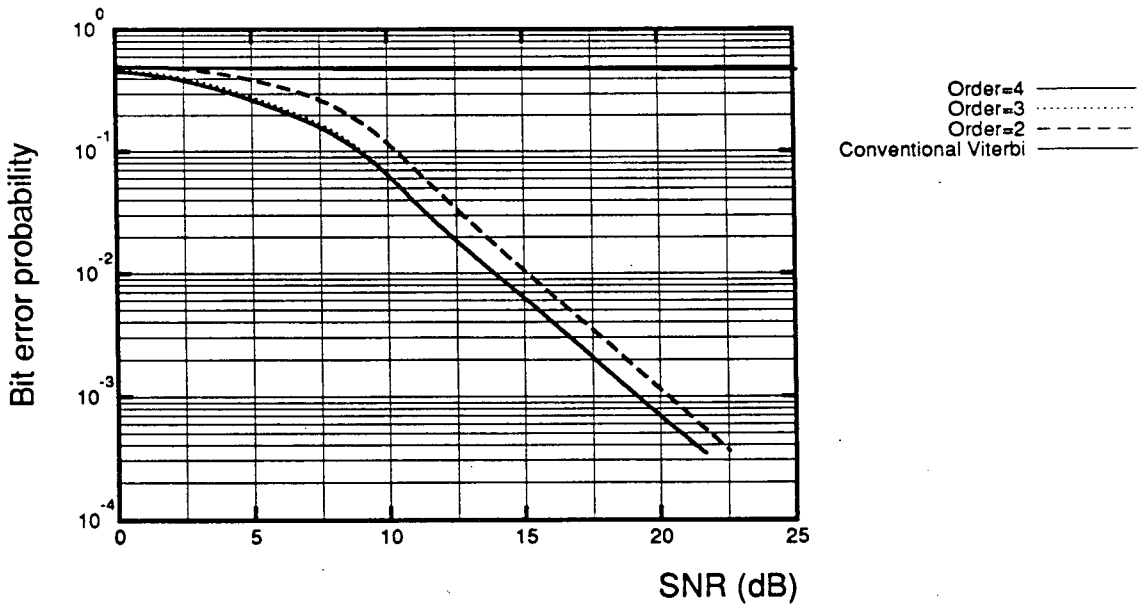

Fig. 3.27. BER of 4–state QPSK in flat Rayleigh fading (land mobile model). Nyquist filter $\alpha = 0.35$, $B_F T = 0.125$.

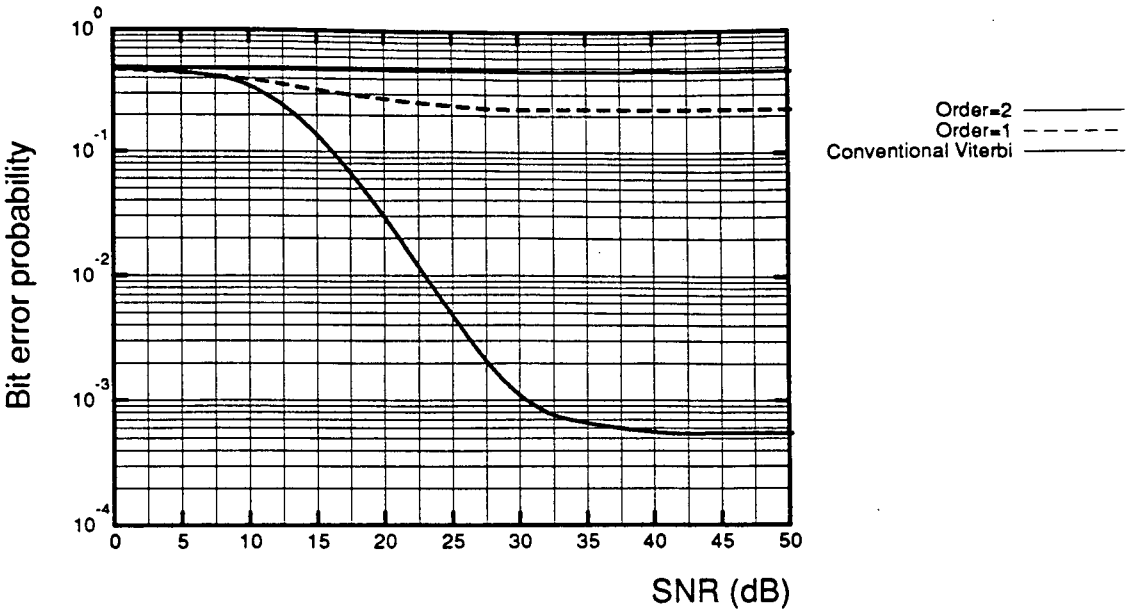

Fig. 3.28. BER of 8–state 8–QAM in flat Rayleigh fading (land mobile model). Nyquist filter $\alpha = 0.35$, $B_F T = 0.125$.

the system with $\alpha = 0.35$. This happens because the higher frequencies of the fading spectrum are attenuated more by the receiver filter.

The next two figures present performance evaluation results for 8–QAM type of signals. In particular, Fig. 3.28 illustrates the performance of an 8–state trellis coded 8–QAM system, employing $\alpha = 0.35$ filters in a land mobile Rayleigh fading channel, with $B_F T = 0.125$. It is clear that from the figure that with $z = 2$, the error floor has been reduced to below 10^{-3}. In Fig. 3.29, the performance of an equivalent (i.e., same channel conditions and filters) trellis coded $\pi/4$–shift 8–DQAM system, is presented. For a fair comparison, we have included the performance of a conventional differentially detected $\pi/4$–shift DQPSK system. Clearly, the $\pi/4$–shift 8–DQAM outperforms the conventional system, even for $z = 2$.

In Fig. 3.30, the performance of a 4–state coded QPSK ($\alpha = 0.35$), operated in a Ricean fading channel, with $K_{\text{dB}} = 10$ dB, is presented. For comparison purposes, the performance of the same system in a Rayleigh fading channel is also included. Notice how the performance curves of all these receivers (i.e., z=2, 3 and 4) almost coincide for the Ricean fading channel.

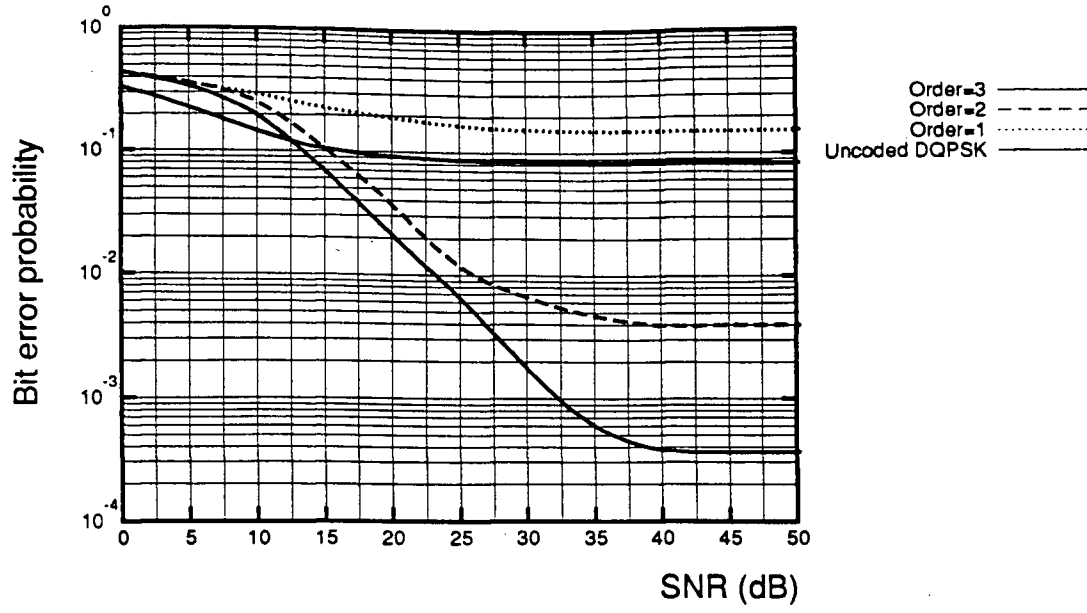

Fig. 3.29. BER of 8–state $\pi/4$–shift 8–DQAM in flat Rayleigh fading (land mobile model). Nyquist filter $\alpha = 0.35$, $B_F T = 0.125$.

Finally, Fig. 3.31 presents some BER performance results for a 4–state coded QPSK system, employing a $z = 3$ receiver and operated in a Ricean fading channel, with $K_{\text{dB}} = 0$ dB, 5 dB and 10 dB. In the same figure, the two limiting curves for Rayleigh fading and AWGN channels,

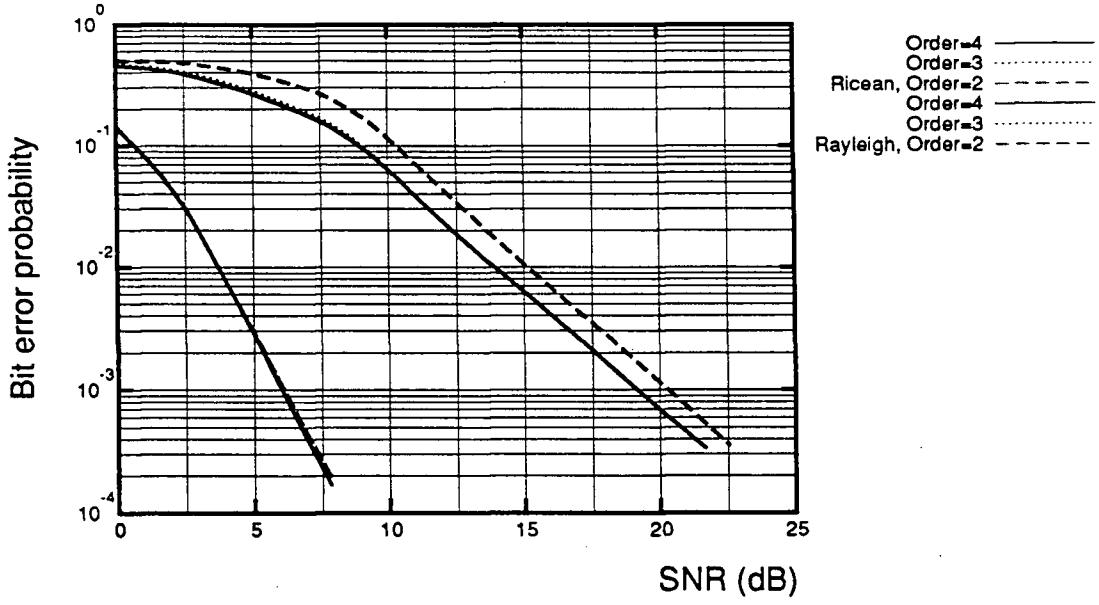

Fig. 3.30. BER of 4–state QPSK in Ricean versus Rayleigh flat fading (land mobile model). Nyquist filter $\alpha = 0.35$, $B_F T = 0.125$.

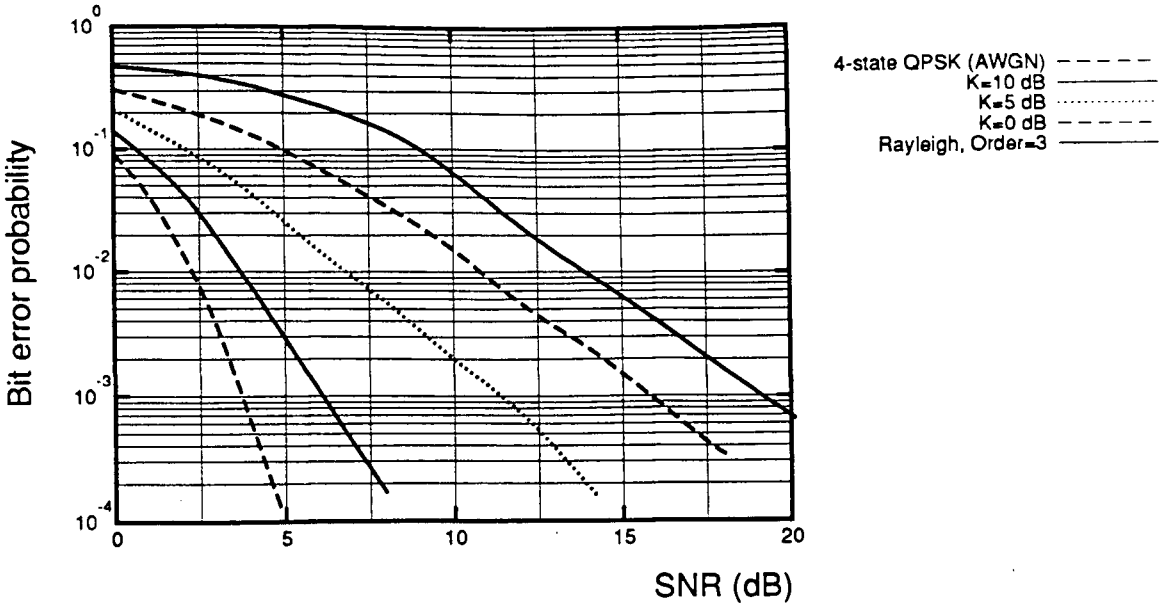

Fig. 3.31. BER of 4–state QPSK employing $z = 3$, in flat Ricean fading (land mobile model). Nyquist filter $\alpha = 0.35$, $B_F T = 0.125$.

are also included. As expected, with increasing values of the K–factor, the performance of the simulated $z = 3$ system systems, moves towards the performance in the AWGN channel.

3.3.2. Uncoded schemes

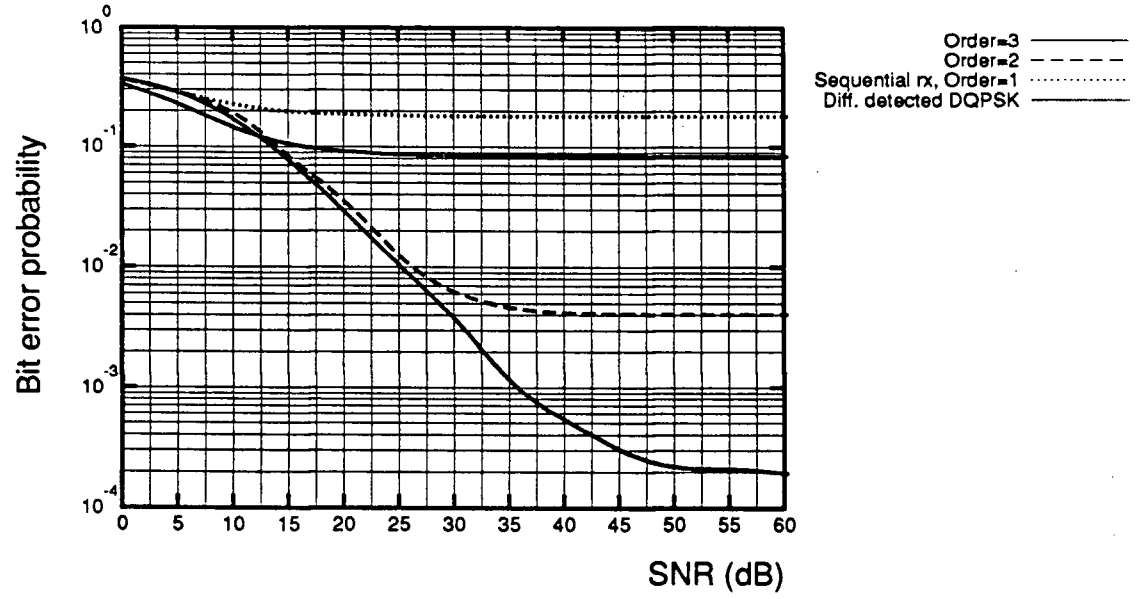

Fig. 3.32. BER of $\pi/4$–shift DQPSK in flat Rayleigh fading (land mobile model). Nyquist filter $\alpha = 1.0$, $B_F T = 0.125$.

The BER performance of $\pi/4$–shift DQPSK was obtained for the Rayleigh fading channel. The simulation results for $B_FT = 0.125$ and $B_FT = 0.0125$ are shown in Fig. 3.32 and Fig. 3.33 respectively. The Nyquist filter roll-off factor is $\alpha = 1.0$ and the fading model used is the land mobile. The reduction of the error floors is evident here also, especially for the fast fading ($B_FT = 0.125$) channel. These BER results will be compared later on, in Chapter 5, with experimental BER measurements of an equivalent $\pi/4$–shift DQPSK system implemented in hardware.

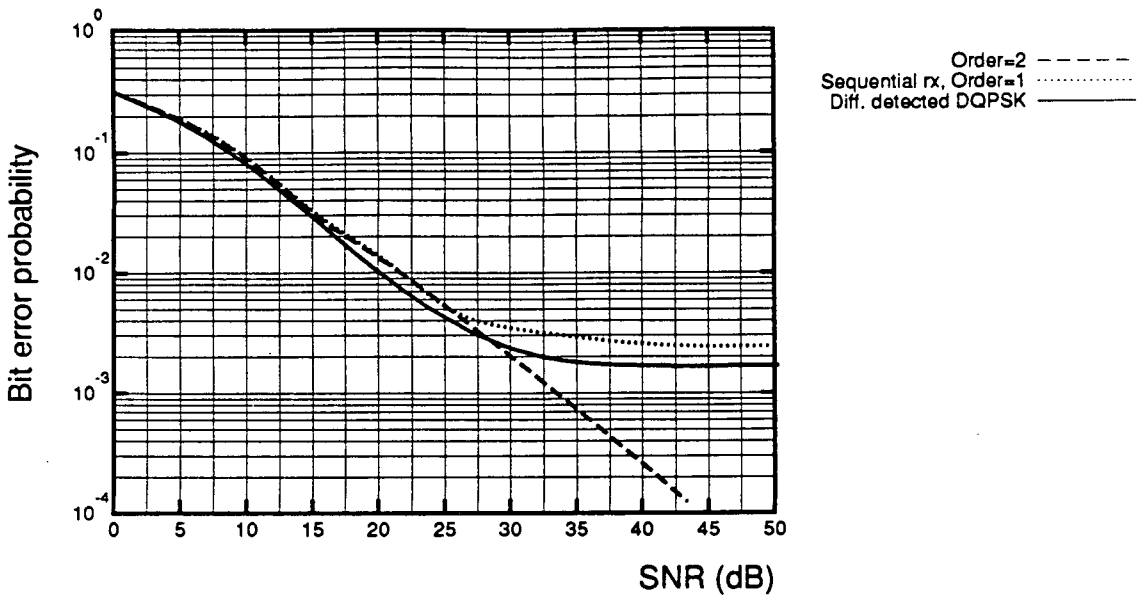

Fig. 3.33. BER of $\pi/4$–shift DQPSK in flat Rayleigh fading (land mobile model). Nyquist filter $\alpha = 1.0$, $B_FT = 0.0125$.

3.4. Conclusions

In this chapter, the development of a computer simulation software library which evaluates the BER performance of a wide variety of digital communication systems was described. Furthermore, by employing the developed software, the BER performance of various PSK and QAM systems operated in fading channels, employing the receivers proposed in Chapter 2, was evaluated. The obtained BER results have indicated that these receivers achieve significant

performance improvements, including large error-floor reduction, as compared to equivalent systems employing conventional detectors.

4. Design and Implementation of a Prototype $\pi/4$–shift DQPSK System

4.1. Introduction

In this chapter, the design and implementation of a prototype $\pi/4$–shift DQPSK system will be presented. As illustrated in Fig. 4.1, the overall system consists of a $\pi/4$–shift DQPSK baseband generator, an RF modulator, the channel, an RF demodulator and digital-signal-processor (DSP) based baseband receiver.

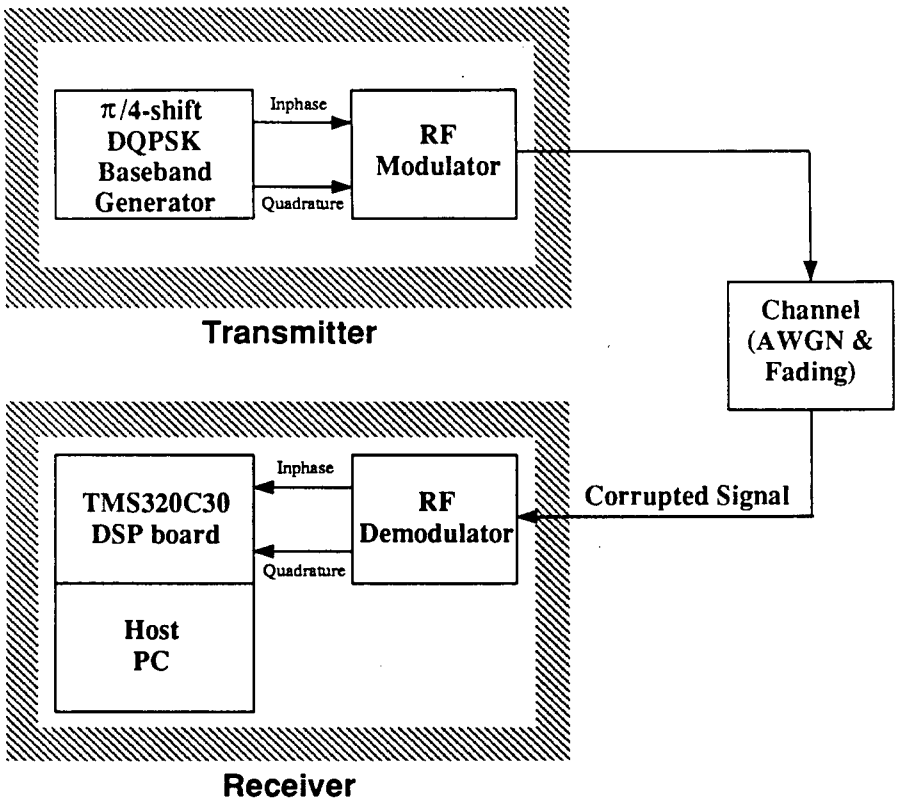

Fig. 4.1. Block diagram of the implemented prototype $\pi/4$–shift DQPSK system.

The main function of the baseband generator is to generate in baseband, a raised cosine filtered $\pi/4$–shift DQPSK signal. The design was realized using widely available off-the-shelf

digital TTL chips and linear analog devices. Using a prototype RF modulator, the baseband signal is modulated in quadrature, so that it can be transmitted through the communication channel. In the channel, AWGN as well as multiplicative Rayleigh fading are corrupting the transmitted signal.

At the receiver, after coherent demodulation[10] which is achieved by an in-house designed and implemented RF demodulator. The received signal is sampled and processed by the DSP which acts as the receiver. Due to availability, we used a TMS320C30 development platform which consists of a PC plug-in card and software development tools for this processor. The big advantage of having a DSP based receiver, is that the algorithms evaluated in Chapter 3, can be directly adapted from the software used for computer simulation.

After this introduction, the organization of this chapter is as follows. The second section analyzes the design of the $\pi/4$–shift DQPSK Baseband Generator, describing the circuitry on a functional block level. The third section describes the RF modulator, demodulator and channel simulator design, while the fourth section of the chapter, deals with the DSP-based implementation of the baseband receiver. Schematics for all hardware blocks analyzed in this chapter, can be found in Appendix B. Finally, the last section contains the conclusions of the chapter.

4.2. The Synthesized $\pi/4$–shift DQPSK Baseband Generator

A transmitter design for a light-weight portable unit cannot incorporate heavy, bulky Nyquist filters for baseband pulse-shaping. This obvious necessity directed us towards a different approach to pulse shaping, namely pulse synthesis instead of the more traditionally employed pulse filtering. More specifically, a method similar to the one for M-PSK baseband pulse synthesis presented in [55] was adopted in our design. Pulse synthesis is performed through

[10] As mentioned previously, this was assumed for mathematical convenience in the complex baseband derivation. It was replicated in hardware for consistency purposes.

the outputs of which provide the analog waveforms for the inphase (I) and quadrature (Q) modulating channels.

It is well known, that in theory a Nyquist-shaped pulse in the time domain, extends from $-\infty$ to ∞. However, a table of samples cannot have infinite length and furthermore it is well known that the pulse amplitude before and after the sampling instant "dies out" quite fast, e.g., the first maximum after $t = 3T_s$ is down to 1.6% from the pulse amplitude at $t = 0$. An example illustrating this is the x/sin(x) equalized raised cosine Nyquist pulse shown in Fig. 4.2. From

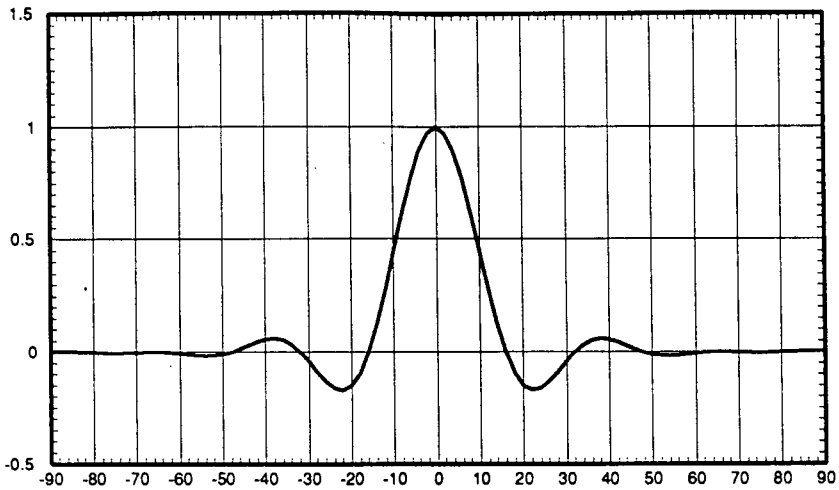

Fig. 4.2. x/sin(x) equalized raised cosine Nyquist pulse with roll-off factor $\alpha = 0.35$; the number of samples/(symbol interval) is equal to 16. The sampling instant is at 0.

this figure it is clear that truncation of the pulse beyond a certain point will not introduce large inaccuracies. The truncation method described in [55] for M-PSK signals, makes use of this observation to limit the number of symbol pulses interfering with each other at any time instant. Once a convenient truncation point has been chosen, the number of overlapping pulses can be determined. The sample tables are then constructed by considering all symbol combinations for the given number of pulses, and generating the samples for the combined output of the pulses in each case. The implementation specific parameters for the $\pi/4$–shift DQPSK baseband generator implemented, are listed in Table 4.2.1. The two tables for the I and Q channels were stored in

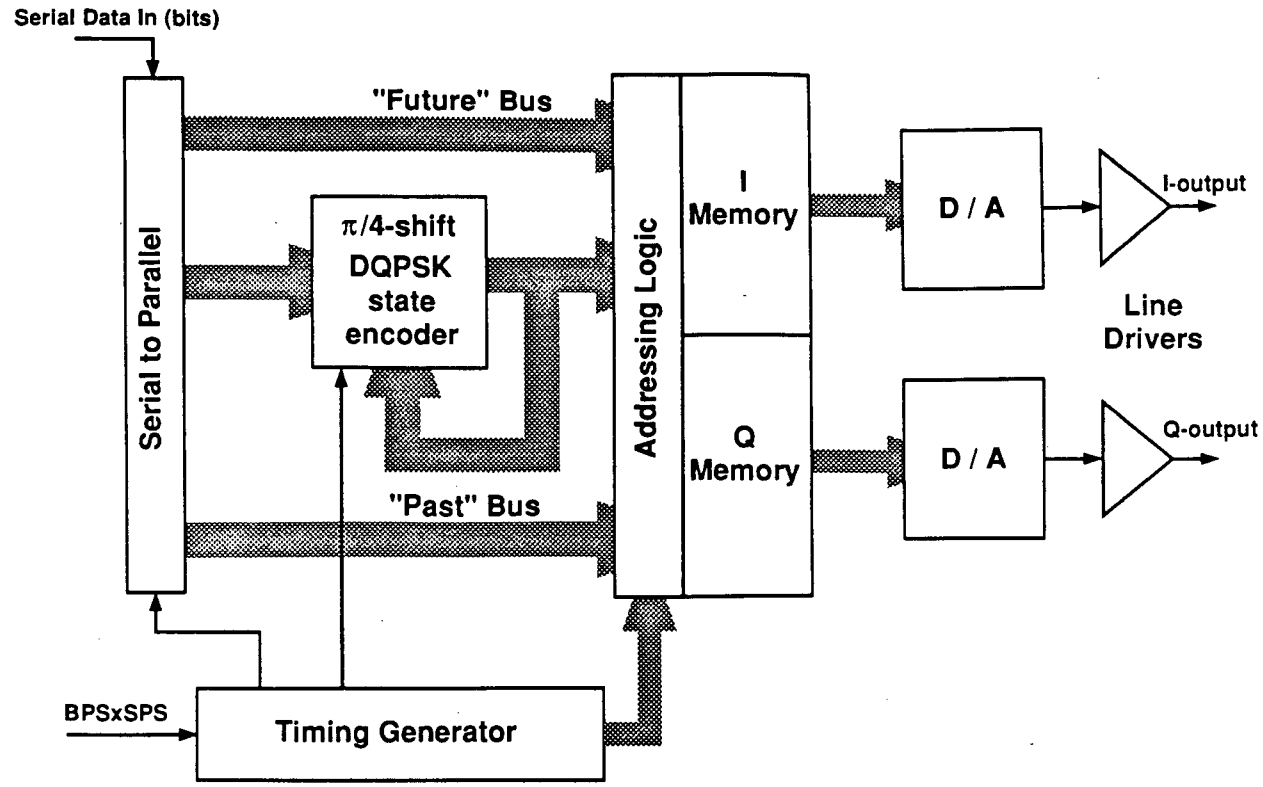

Fig. 4.3. Functional block diagram of the $\pi/4$–shift DQPSK baseband transmitter.

implemented, are listed in Table 4.2.1. The two tables for the I and Q channels were stored in

Table 4.2.1. Pulse-sample synthesis implementation specific parameters.

Integral number of symbol periods:	J = 2 (2 past and 2 future symbols used)
Total number of symbol periods:	2×J+ 1 (the symbol being transmitted) = 5
Number of samples / symbol interval:	8 (or 16)
"Present" signal combinations:	8 (possible $\pi/4$-shift DQPSK absolute phases)
"Past" and "Future" symbol combinations:	$4^J = 4^2 = 16$ (4 possibilities/symbol)
Total number of samples in table:	$(8 \times 16 \times 16) \times 8 = 16384$ (16k samples)
D/A resolution:	256 levels (8-bit words)
Binary storage requirement for I or Q ch.:	16kbytes

EPROMs. The hardware design also supports 2 selections for the number of samples/symbol, namely 8 and 16. For the latter, the binary storage requirement for each I and Q sample table is 32K bytes. The functional block diagram of the baseband $\pi/4$–shift DQPSK experimental transmitter is depicted in Fig. 4.3.

The following is a fairly detailed description of each individual block.

- The **Serial to Parallel** transforms the stream of serial input data bits to parallel form (see Table 4.2.1). Since the integral number of symbol periods used is 2, both the **"Future" Bus** and the **"Past" Bus** provide 2×(2 bits/symbol) = 4 bits. The bus feeding the **$\pi/4$–shift DQPSK state encoder** has two lines providing the 2 bits for the "present" symbol to be sent.
- The **$\pi/4$–shift DQPSK state encoder** is the "heart" of the transmitter, providing at every symbol interval the sequence number of the signal to be transmitted from the $\pi/4$–shift DQPSK signal space. This number depends on the previous signal number and the 2–bit symbol input. A more detailed functional block diagram of the encoder is depicted in Fig. 4.4. The signal numbering convention as well as the phase encoding used are shown in Fig.

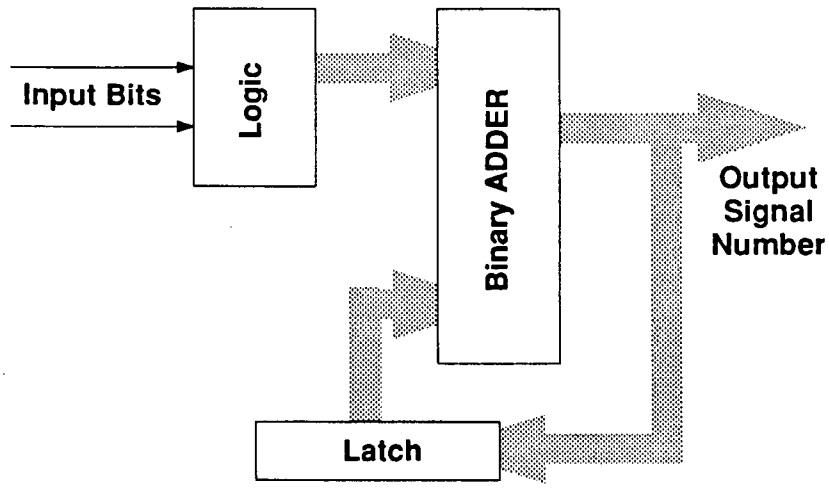

Fig. 4.4. The functional block diagram of the $\pi/4$–shift DQPSK state encoder.

4.5. Essentially, this is a differential encoder (see Eq. 2.2) implemented in digital form. The number assignment of the signal states was done in such a way as to render the recursive implementation of the encoder shown in Fig. 4.4 possible.

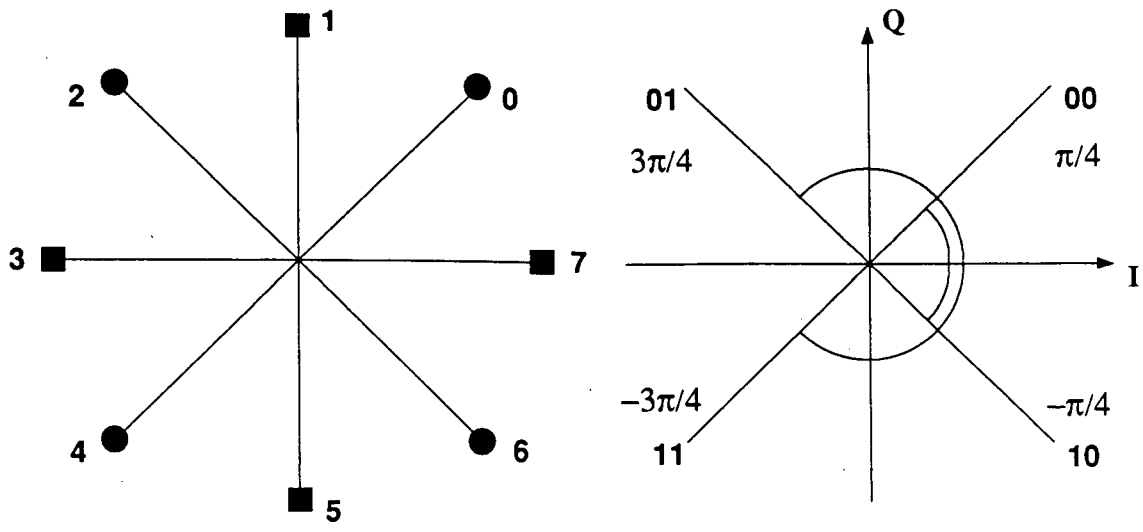

Fig. 4.5. The signal numbering convention and mapping of input information symbols to transmitted differential phases.

The structure and logic of the recursive $\pi/4$–shift DQPSK state encoder reveals itself if one observes the previous-signal — next-signal pairs and input symbols listed in Table 4.2.2. The

Table 4.2.2 Next-signal transmitted as a function of the previous-signal and the input.

		Previous signal transmitted (i.e., previous encoder state) - binary							
		000	001	010	011	100	101	110	111
Input	00	001	010	011	100	101	110	111	000
	01	011	100	101	110	111	000	001	010
	10	111	000	001	010	011	100	101	110
	11	101	110	111	000	001	010	011	100

signal numbers and input dibits are given in binary form. From the bit patterns shown, it can be easily observed that the next signal number can be calculated from the previous signal number and the input dibit through the binary addition of a constant to the previous signal number. This constant depends, as it is expected, on the input dibit, while the addition discards the carry bit. The constants for the four possible input dibits are listed in Table 4.2.3. The two most significant

Table 4.2.3 The constants used for the generation of the next signal number.

		Additive constant
Input Dibit	00	001
	01	011
	10	111
	11	101

bits of any constant can be generated easily by a simple logic circuit receiving as input the input symbol (dibit), while the least significant bit is always 1. The previous signal number is saved in a latch and fed into the binary adder together with the corresponding constant.

- The **I and Q Memory** and accompanying **Addressing Logic** blocks implement the lookup tables for the shaped baseband pulse samples. Each channel (I or Q) memory is a 16kbyte EPROM when using 8 samples/symbol interval and a 32kbyte EPROM when using 16 samples/symbol interval. An example pulse for J=2, 8 samples/symbol and roll-off factor $\alpha = 0.35$ is shown in Fig. 4.6 with the sampled values marked by square blocks. The

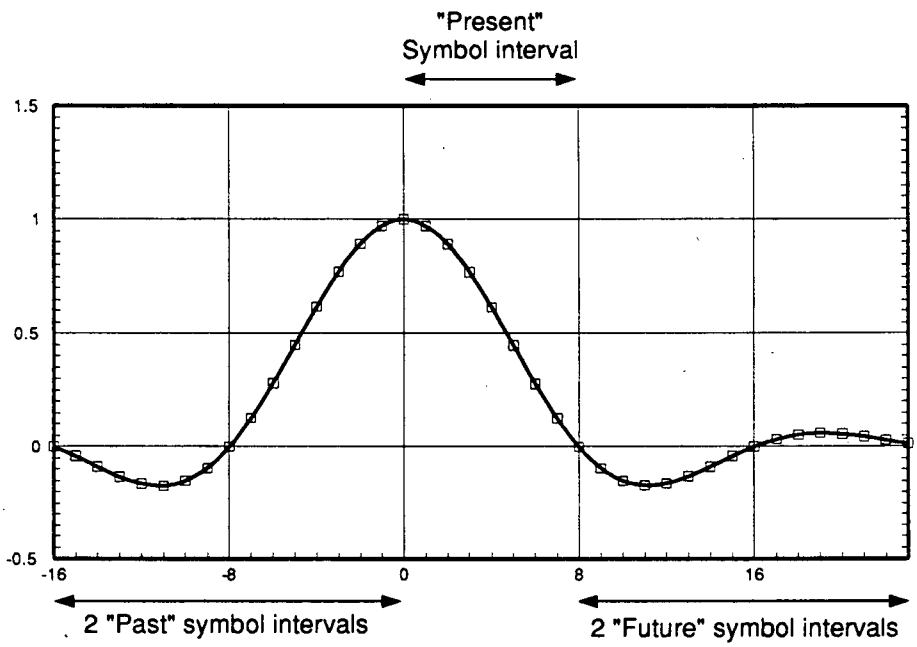

Fig. 4.6. Example pulse with J=2, 8 samples/symbol and $\alpha = 0.35$.

plot in Fig. 4.6 clearly shows the 5 symbol intervals for J=2, each one holding 8 samples.

An example demonstrating the derivation of the pulse samples for all symbol combinations resulting from the parameters in Table 4.2.1, is shown in Fig. 4.7. In this figure, each cluster of 5 symbol intervals corresponds to a 2–bit symbol input. This input determines the pulse amplitude and polarity. The result of the sum of the 5 samples at each sampling instant is the number which is tabulated in the EPROM for each channel. The index of this result in the EPROM is determined by the J symbols in the past ("Past Bus"), the J symbols in the future ("Future Bus") and the signal from the $\pi/4$–shift DQPSK signal space currently being transmitted. Note that the actual sample values saved in the EPROMs are integers from 0 to 255, resulting from re-normalization and truncation (or rounding-up) of the floating point values. A C-language program used to generate the binary files for the I- and Q-channel EPROM for any value of the roll-off factor α, the truncation factor J and any number of samples/symbol can be found in Appendix C. It should also be pointed out, that the full α Nyquist raised cosine filter response was used to produce the pulse samples used by the $\pi/4$–shift DQPSK baseband generator. On the receiver side, a simple Butterworth filter was used, with a high enough cutoff frequency as not to distort the transmitted signal. This method of including the full filter at the transmitter is not at all optimum (see Chapter

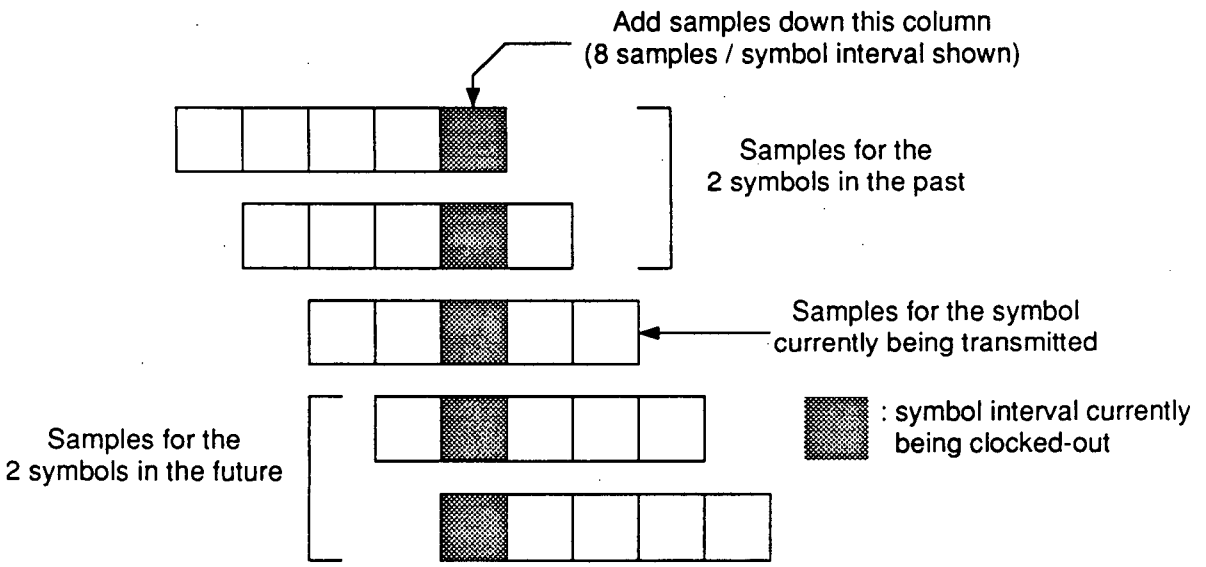

Fig. 4.7. Derivation of the pulse samples for J=2.

maximum signal to noise ratio at the output of the receive filter, but greatly simplifies the design with relatively small trade-off in BER performance.

- The **Timing Generator** provides all the necessary timing signals, including a data rate clock used to clock-out the data bits from the information source and a symbol- and bit-SYNC used at the receiver end. It should be pointed out that the symbol timing recovery circuit needed at the receiver of a real-life modem was omitted, the reason being that symbol synchronization was beyond the research of this thesis. An external clock option was also implemented, so that a variable bit rate system can be implemented. In this case the supplied clock must have a frequency F = (Number of samples / symbol) × (Desired Bit Rate).
- The analog output section incorporates two **8–bit D/A converters**, one for each channel, and two **line drivers**. Each line driver includes:

  a. a simple 3–pole Butterworth filter which smooths out the "staircase"-like output from the D/A's by removing undesirable high frequencies.

  b. a high current driver since the outputs drive 50 Ω loads. The loads are driven through 50 Ω precision trimmers so that accurate matching, necessary for minimum inter-symbol-interference (ISI), can be performed.

4.3. RF Modulator/Demodulator (MODEM) and Channel

Following Fig. 4.1, a more detailed block diagram of the RF Modulator/Demodulator (MODEM) as well as the channel, appears in Fig. 4.8.

The carrier frequency employed, as indicated on the block diagram, is 1.5 MHz. The reason for choosing this relatively low carrier frequency is the considerable amount of problems inherent to designs involving carrier frequencies in the VHF/UHF bands. The frequency chosen greatly simplifies the RF design of both the modulator and demodulator, as well as the RF section of the channel model, without compromising in any way the accuracy of the experimental

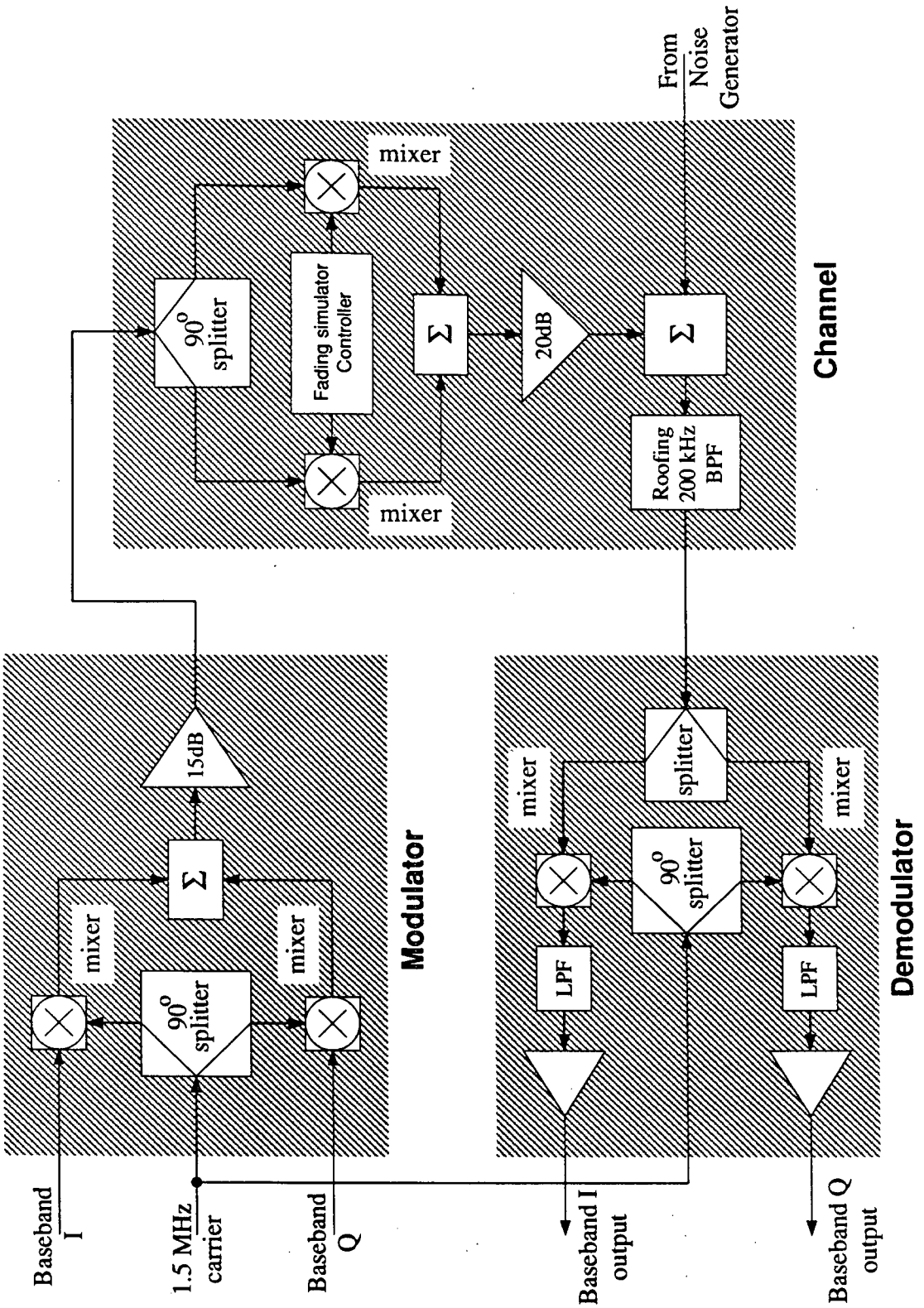

Fig. 4.8. Functional block diagram of the MODEM and the RF channel.

measurements. The choice of carrier frequency was also limited by the frequency coverage of the Gaussian white noise generator used, and the roofing BPF filter available. The generator coverage was specified by the manufacturer to be in the 6 kHz to 25 MHz band. This relatively wideband noise must be limited by using a roofing band-pass filter before it is added onto the faded signal. The BPF employed is centered around the carrier frequency of 1.5 MHz and has a 3 dB bandwidth of 200 kHz.

The modulator was implemented using a 90° phase splitter which provides the inphase and quadrature components of the modulated carrier, and two mixers. The mixer outputs are then added by means of a signal combiner, to form the RF modulated signal. A series of amplifier blocks were used to boost the power output from the modulator, since the relatively high overall conversion loss – approximately 20dB down from the 7dBm Local Oscillator (LO) input of the modulating mixer – results to a considerably weak signal. The same layout was used for the design of the RF channel module, the only difference being the baseband I and Q inputs, which in this case are generated from the fading simulator controller presented in [56]. The demodulator was implemented as described in the theoretical derivation (see Fig. 2.3), i.e., the same carrier used for the modulator, is used to coherently downconvert the received signal to baseband. The same type of 90° phase splitter used in the modulator, is also used here to provide inphase and quadrature components of the carrier. In a real-life modem, a noncoherent demodulator would have to be implemented at the RF level and not in baseband, as was the case for our experimental testbed. Two well known noncoherent receiver designs are a) RF differential detector and b) RF limiter/discriminator.

- The RF differential detector implementation uses delay lines in order to produce a version of the incoming signal, delayed by T seconds, which is then multiplied with the non-delayed signal. The disadvantage of this method is the delay line used, which a) is generally difficult to design and b) will work only for one transmission rate, i.e., only at $R = 1/T$.

- The RF limiter/discriminator noncoherent detector, relies on an FM discriminator which provides the first derivative of the carrier phase (i.e., the instantaneous frequency). Using this as input, an integrate-and-dump filter provides the phase change for each symbol period. This design is far more flexible than the RF differential detector, since it can operate on any transmission rate desired, without modification. Furthermore, since it is much easier to implement, it is in general, the preferred design.

Schematic circuit diagrams for the blocks shown in Fig. 4.8 are included in Appendix B.

4.4. The Digital Signal Processor (DSP) – based Receiver

The heart of the receiver was implemented using a digital signal processor (DSP) chip. The main advantage presented by a DSP based design over an all-hardware implementation is the great versatility in terms of developing efficient receiving/decoding algorithms. The disadvantage of this approach is the processing time trade-off which prohibits the use of such processors in high speed digital modems running complex and computationally intensive algorithms. However, in a final design, a software/hardware hybrid approach using a few dedicated VLSI integrated circuits can remove this processing time constraint.

The DSP development platform used is a Personal Computer (PC) plug-in board, using the Texas Instruments TMS320C30 digital signal processor chip. Software development tools running on the host PC provide assembler, C compiler, linker and utilities for loading and running application software on the DSP board. A somewhat more detailed functional block diagram for the DSP-based digital receiver is depicted in Fig. 4.9.

The analog front-end provides for two filtered inputs. The onboard filters are 4^{th} order Butterworth with unity gain, while their cutoff frequency is determined by a plug-in resistor pack [57]. A/D conversions are triggered by using the board's external triggering option. The

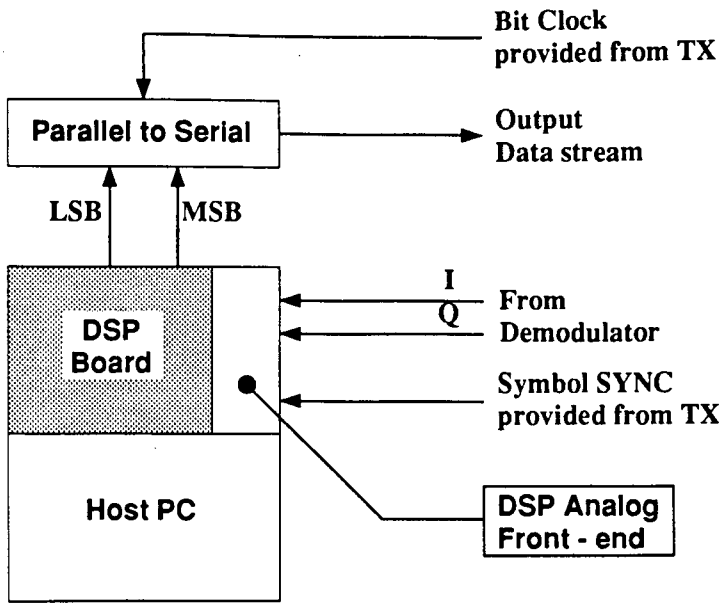

Fig. 4.9. Functional block diagram of the DSP-based digital receiver.

The receiver software is divided in two distinct blocks, namely the *kernel* and the *decoding routine*. The kernel, written in assembly language, performs hardware-specific initialization and establishes the interrupt-service routine triggered by the **Symbol SYNC** signal. This interrupt routine, when triggered by the symbol timing signal, reads the input samples and passes them on to the decoding routine. After decoding is done, it writes out to the digital I/O port the symbol returned from the decoding routine (2 bits for $\pi/4$–shift DQPSK), the bits of which are then clocked-out serially. The decoding routine is an external code module which can be written in assembly or in C. In this case the latter was chosen in order to speed up development time, by making use of the same decoding routines used in the software simulation of the system. However, the C compiler supplied by the chip manufacturer provides assembly output so that the code can be further optimized for speed, if this is desirable.

4.5. Conclusions

This chapter dealt with the design and implementation of a prototype $\pi/4$–shift DQPSK system. Our discussion included detailed description of the following system modules: $\pi/4$–shift DQPSK baseband generator, RF modulator and demodulator and a DSP-based receiver.

5. Experimental Set-up and Measurements

5.1. Introduction

This section describes the experimental set up used to evaluate the prototype $\pi/4$–shift DQPSK system. It also presents the obtained experimental BER performance evaluation results of the implemented receiver systems which are derived in Chapters 2 and 3. The chapter organization is as follows. After this introduction, in Section 5.2, the experimental set up is described. Section 5.3 presents numerous experimental signal measurements. In Section 5.4, the experimental BER performance evaluation measurements can be found. Finally, Section 5.5 contains the conclusions of the chapter.

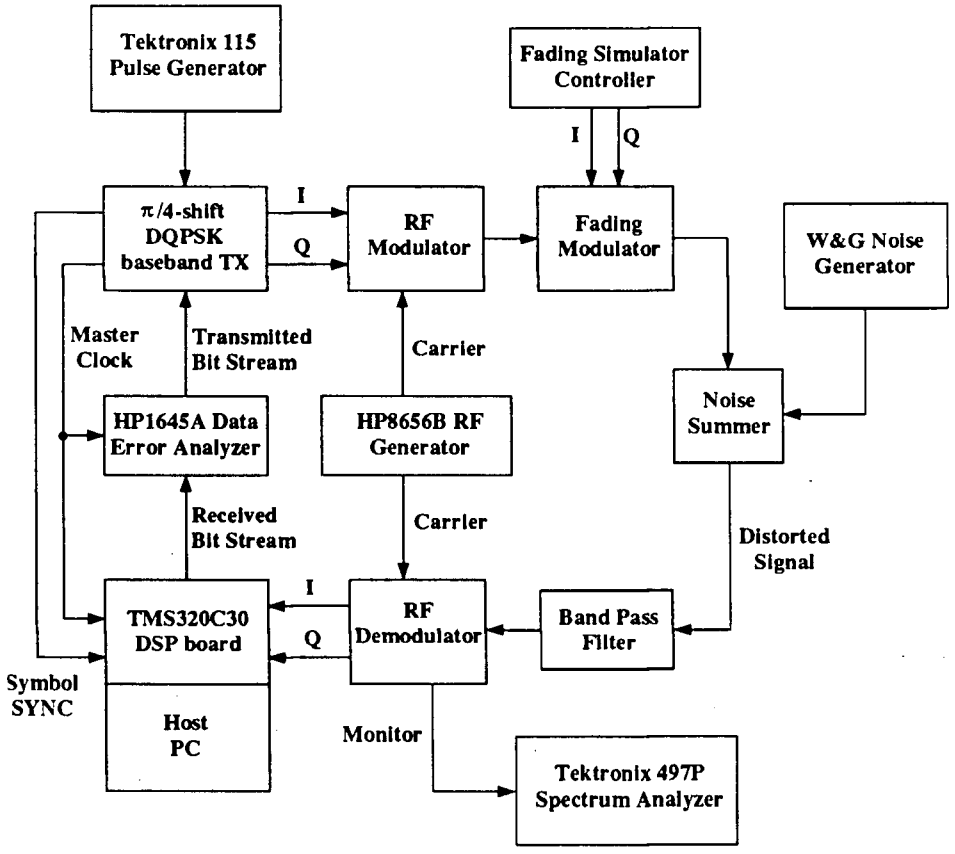

Fig. 5.1. Functional block diagram of the experimental layout.

5.2. Experimental Set-up

The block diagram of the experimental testbed used for system evaluation is depicted in Fig. 5.1. In addition to the test equipment shown, a Philips PM3055, 50 MHz oscilloscope was used to monitor the baseband signal waveforms. The Pulse Generator shown is also optional, since the $\pi/4$–shift DQPSK baseband generator has Master Clock generation circuitry onboard. However, the onboard clock was fixed to 200 kBaud, whereas the external timing generator allowed tests at lower Baudrates. This capability proved to be very useful when testing the real-time processing capabilities of the DSP processor used, in conjunction with the computational load presented by the proposed algorithm. Two photographs of the complete experimental set up can be found in Fig. 5.3.

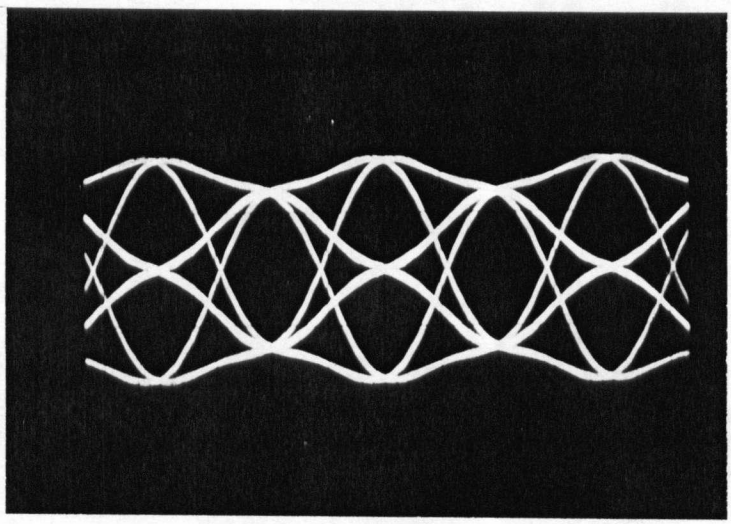

Fig. 5.2. I-channel eye-diagram at modulator input; $\alpha = 1.0$.

5.3. Signal Measurements

The I-channel eye-diagram[11] at the input of the modulator, using a Nyquist roll-off factor of $\alpha = 1.0$, appears in Fig. 5.2. The very small amount of ISI introduced at the sampling instants, is due to pulse truncation used at the $\pi/4$–shift DQPSK baseband generator. As α decreases,

[11] From now on, in this chapter, reference to eye-diagrams will denote the I-channel eye-diagram.

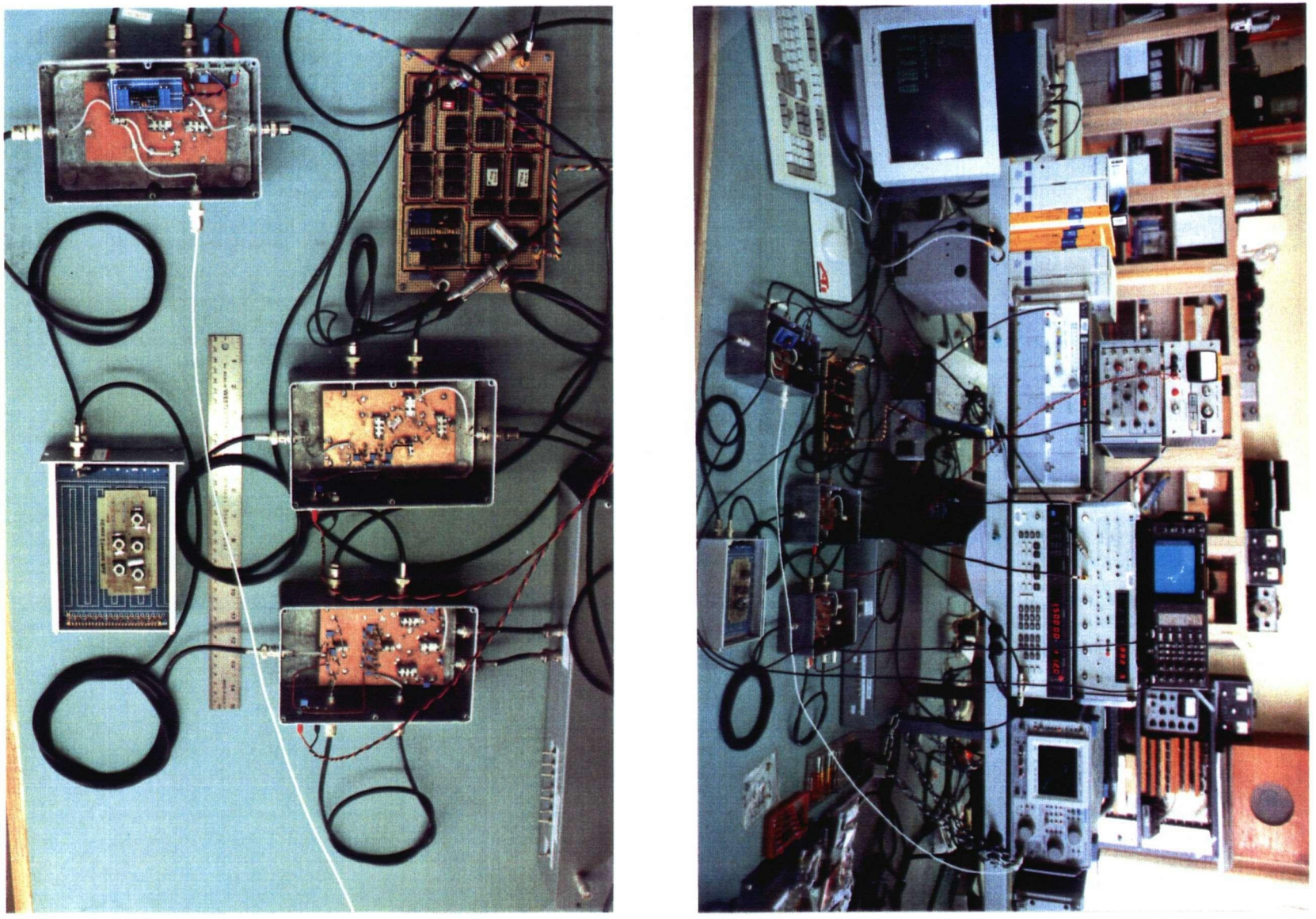

Fig. 5.3. Photograph of the complete experimental set up, in the Communications Research Laboratory of the Department of Electrical Engineering at the University of British Columbia.

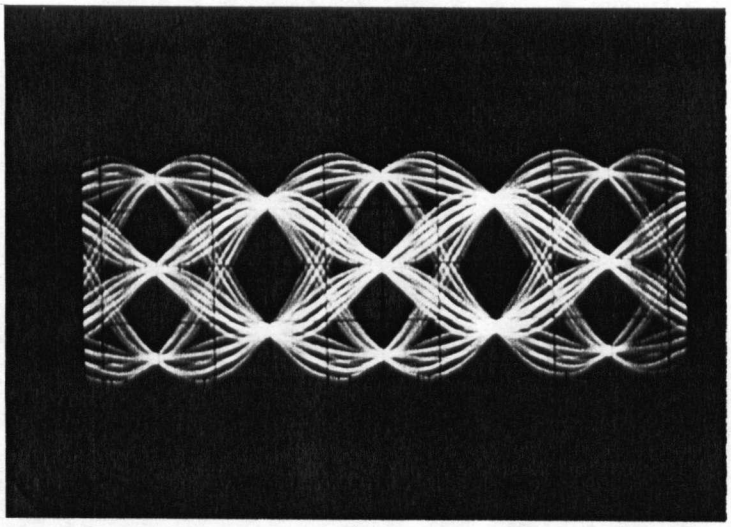

Fig. 5.4. I-channel eye diagram at modulator input; $\alpha = 0.5$.

the amplitude of the Nyquist pulse tails will increase [2]. As a result, the ISI produced by the implemented pulse truncation synthesizing technique, is expected also to increase. This is evident in Fig. 5.4, where the eye-diagram at the modulator input, with $\alpha = 0.5$ is given. The eye-diagram at the demodulator output without any channel interference, for $\alpha = 1.0$, appears in Fig. 5.5. When we compare it with 5.2, the slight degradation introduced by the modulation/demodulation process is evident. The equivalent eye-diagram for $\alpha = 0.5$ is shown in Fig. 5.6.

The phase symmetry of the signal space is also distorted by the non-ideal modulator and demodulator circuitry. Fig. 5.7 shows the signal space at the modulator input while Fig. 5.8 shows the signal space at the demodulator output, both for $\alpha = 1.0$. The modulated and demodulated signal space for $\alpha = 0.5$, appear in Figures 5.9 and 5.10, respectively. This signal space distortion is mainly a result of the phase unbalance in the 90^{o} splitters used at the modulator and demodulator. For instance, the maximum phase unbalance specification for the components used is 3^{o} [58]. The second factor seriously affecting the signal constellation at the demodulator output, is the power driving the local oscillator (LO) inputs of the mixers used.

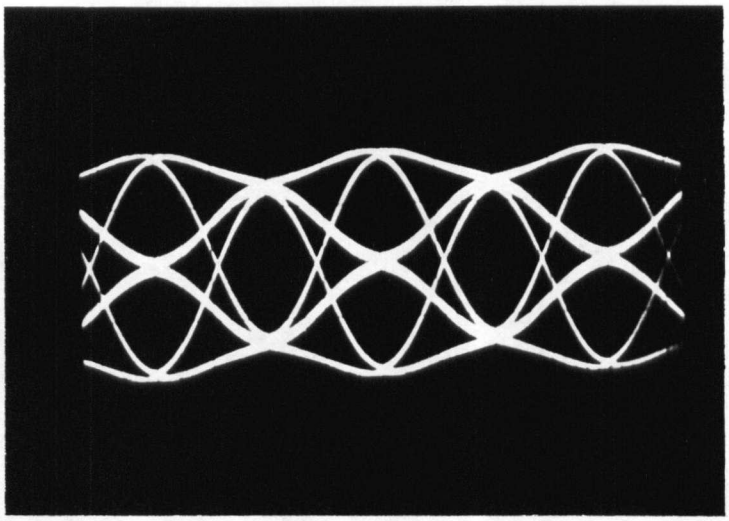

Fig. 5.5. I-channel eye diagram at demodulator output; $\alpha = 1.0$.

Any deviation greater than 1.5 dB from the specified 7 dBm LO drive, was found to distort the signal space geometry considerably.

The spectrum of the transmitted signal gives one more indication of the limitations inherent to the pulse synthesis technique. The spectrum for $\alpha = 1.0$ is illustrated in Fig. 5.11, and that for $\alpha = 0.5$ in Fig. 5.12. The Baudrate for both measurements was fixed to 100 kBaud. The spectrum corresponding to $\alpha = 0.5$ shows considerably more spurious energy around the

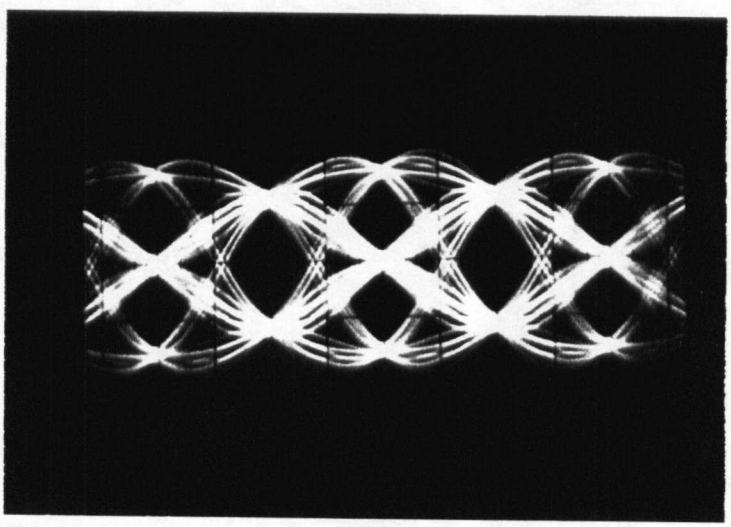

Fig. 5.6. I-channel eye diagram at demodulator output; $\alpha = 0.5$.

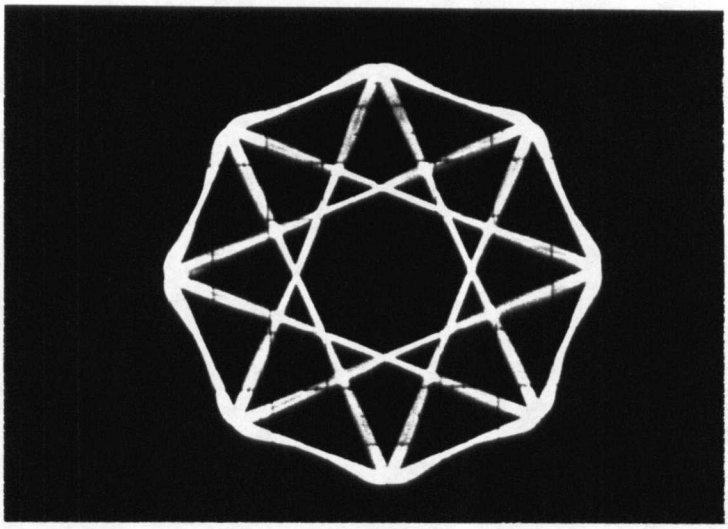

Fig. 5.7. Modulated signal space diagram; $\alpha = 1.0$.

main "lobe", even when compared to the theoretically wider spectrum for the $\alpha = 1.0$ case. However, close to the carrier frequency, the bandwidth reduction when using the lower value for α is evident. The spurious energy distorting the spectrum shape, will increase as the value of α decreases and at the same time the truncation limit J (see Table 4.2.1) remains constant. If small values of the Nyquist roll-off factor are to be used efficiently, the number of "past" and "future" symbols considered (see Chapter 4) will have to be increased, as the amplitude of

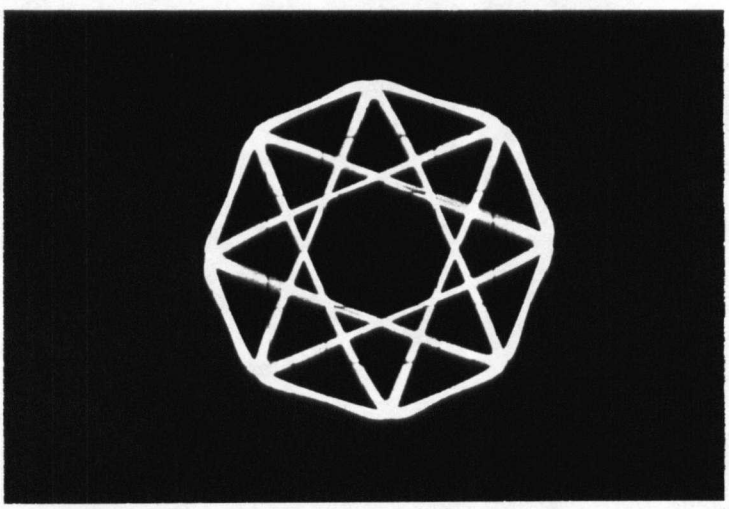

Fig. 5.8. Demodulated signal space diagram; $\alpha = 1.0$.

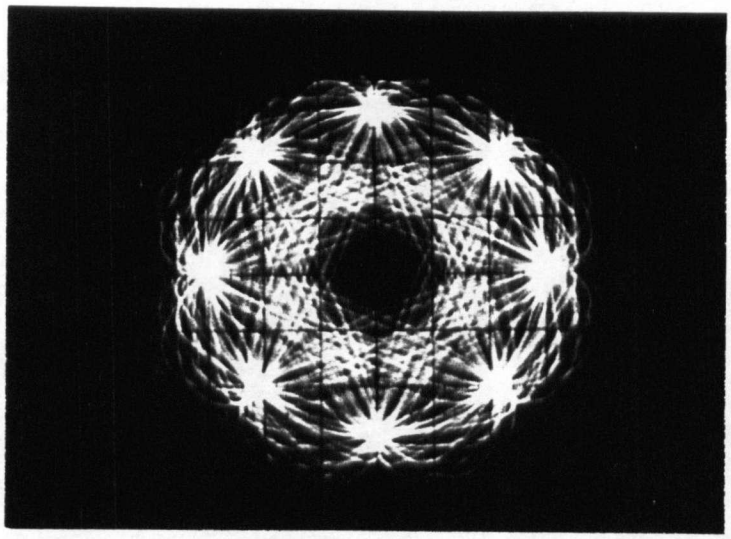

Fig. 5.9. Modulated signal space diagram; $\alpha = 0.5$.

the Nyquist pulse tails increases, for decreasing values of α. The spectrum of the received signal, for $\alpha = 1.0$, with AWGN present is illustrated in Fig. 5.13, while the corresponding eye-diagram at the demodulator output is shown in Fig. 5.14. The spectrum and corresponding eye-diagram for the case when $\alpha = 0.5$ are depicted in Fig. 5.15 and 5.16, respectively. Note the eye closure caused by the noise in both Figures 5.14 and 5.16.

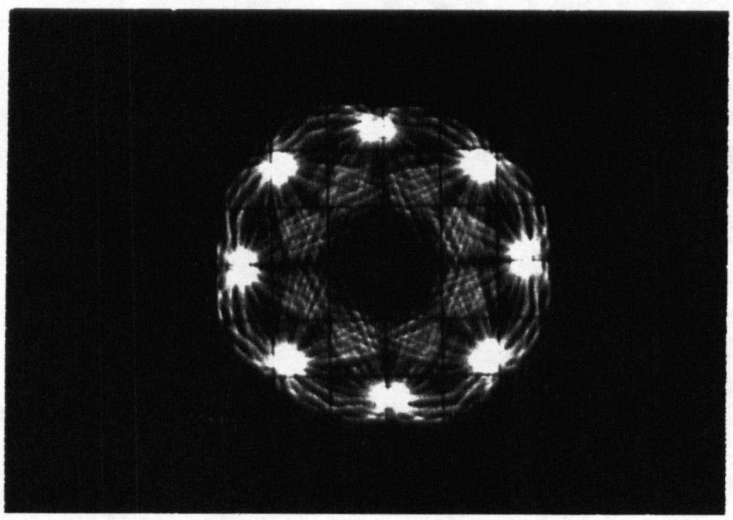

Fig. 5.10. Demodulated signal space diagram; $\alpha = 0.5$.

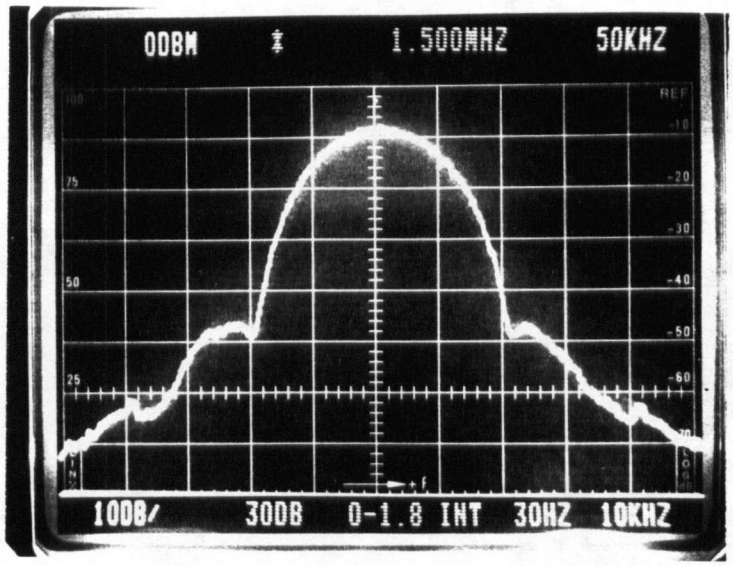

Fig. 5.11. The spectrum of the transmitted $\pi/4$–shift DQPSK signal; $\alpha = 1.0$.

Finally, the spectrum of the faded carrier with the maximum Doppler frequency B_F set equal to 126 Hz (the maximum B_F for the fading simulator controller used [56]), is illustrated in Fig. 5.17.

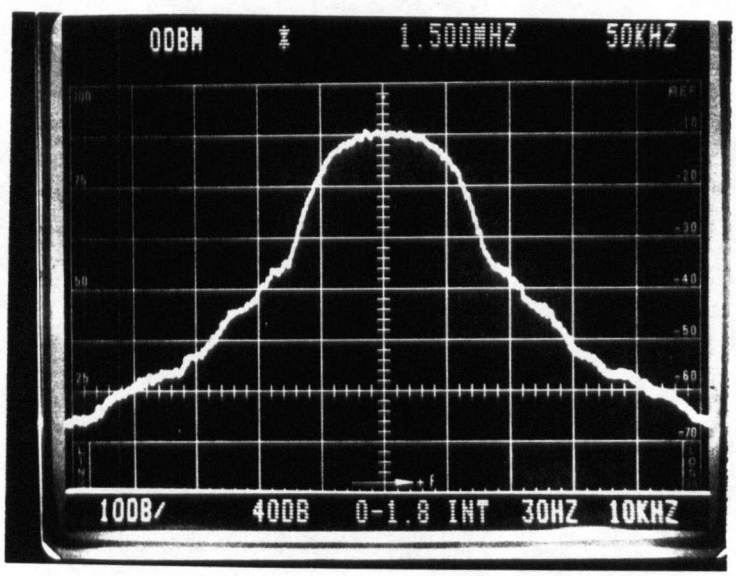

Fig. 5.12. The spectrum of the transmitted $\pi/4$–shift DQPSK signal; $\alpha = 0.5$.

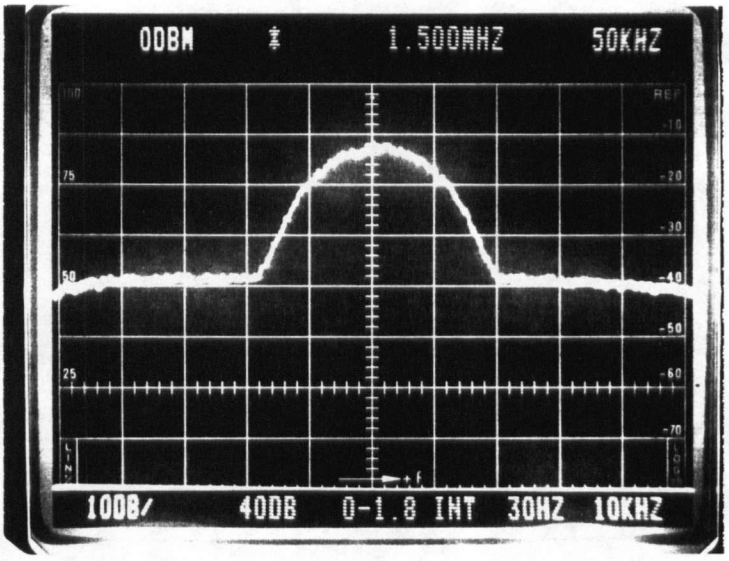

Fig. 5.13. The spectrum of $\pi/4$–shift DQPSK in AWGN; $\alpha = 1.0$.

5.4. BER Performance Evaluation Measurements

Measured BER performance results were obtained from the prototype $\pi/4$–shift DPQSK system, employing two types of receivers, a conventional differential detector receiver (see Eq. 3.20) and a multiple differential receiver based on the detection algorithm of Eq. 2.34.

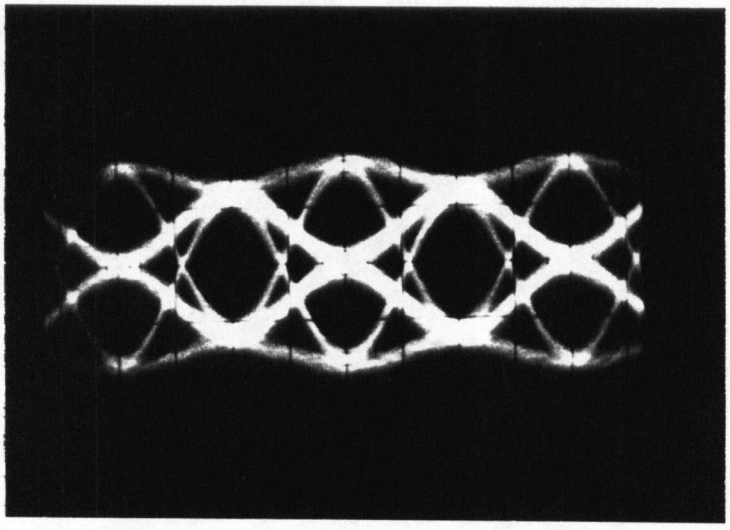

Fig. 5.14. I-channel eye diagram at demodulator output with AWGN present; $\alpha = 1.0$.

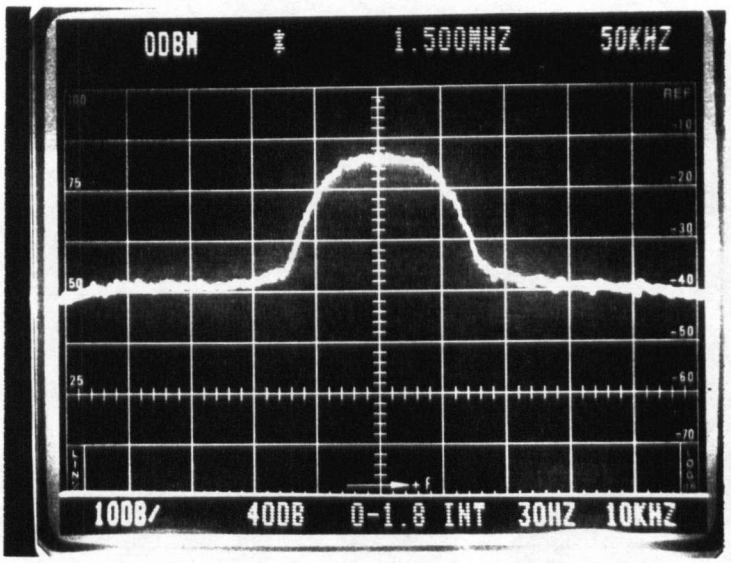

Fig. 5.15. The spectrum of $\pi/4$–shift DQPSK in AWGN; $\alpha = 0.5$.

Measurements performed with the conventional differential detector in an AWGN channel, exhibited a small deviation (approximately 1.5–2 dB at a BER of 10^{-4}) from the theoretically expected performance. This deviation is due to the following factors.

- The imperfect pulse-synthesizing technique employed by the $\pi/4$–shift DPQSK baseband generator, which, as it has been demonstrated already (see Fig. 5.5 and 5.6), introduces

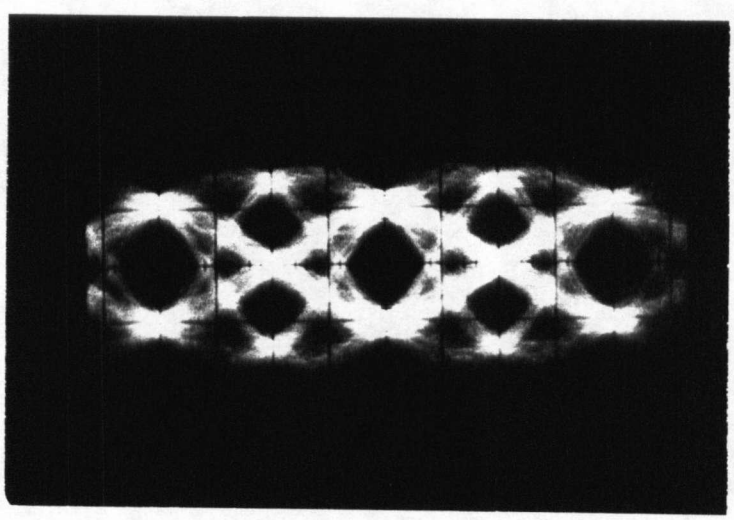

Fig. 5.16. I-channel eye diagram at demodulator output with AWGN present; $\alpha = 0.5$.

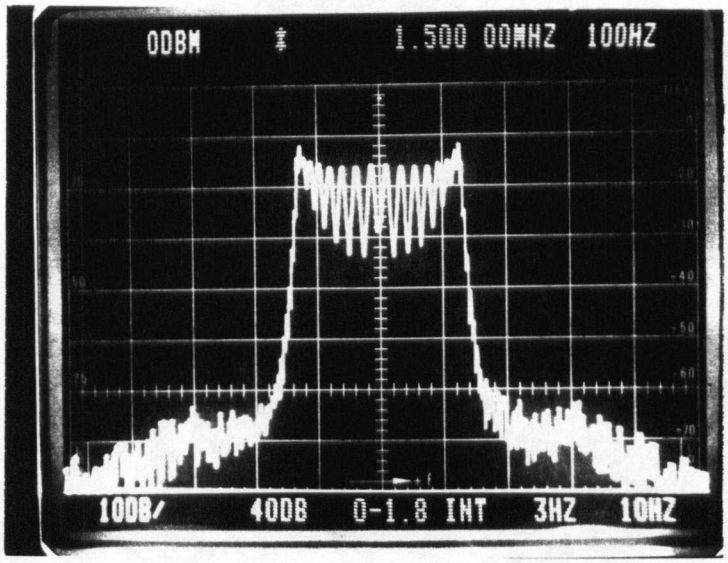

Fig. 5.17. The spectrum of the faded carrier with maximum Doppler frequency set to $B_F = 126$ Hz.

ISI at the sampling instant.

- ☐ The non-ideal signal-space at the demodulator output, due to imperfect RF components. A noticeable deviation from ideal quadrature can be observed in Fig. 5.8 and 5.10.
- ☐ The way in which filtering has been realized in hardware. In the computer simulations, $\sqrt{\alpha}$ Nyquist filters are realized for both the transmitter output and the receiver input. In hardware, however, the full α Nyquist filter is implemented at the $\pi/4$–shift DPQSK baseband generator, while a simple first order Butterworth filter is used at the mixer outputs in the demodulator.

BER measurements for the conventional differential detector in an AWGN and Rayleigh fading channel, for three values of the B_FT product, are presented together with the corresponding computer simulation results, in Fig. 5.18. The close agreement between the experimental and the computer simulated BER results is evident.

Finally, in Fig. 5.19, the measured BER performance of the $z = 1$ and $z = 2$ reduced complexity receiver, operating in AWGN and Rayleigh fading with $B_FT = 0.125$, are presented. For comparison purposes, the equivalent computer simulated results are also included. It is

evident from the BER results, that there is more than an order of magnitude reduction of the error floor.

The deviations observed in the experimental measurements presented in Figs. 5.18 and 5.19, are attributed primarily to the DSP analog input subsystem. More specifically, the input voltage range of the A/D input on the DSP board, for a full range operation of the onboard A/D converters, is specified to be +/-3 Volts [57]. However, the faded inphase and quadrature signal at the demodulator output, present considerable amplitude fluctuation, such that frequent signal peeks above +3 Volts or below –3 Volts are clipped. From the measurements in the figures presented, it can be observed that the discrepancies are more severe when the multiple differential detector receiver is used. This is attributed to the memory inherent to this detection algorithm.

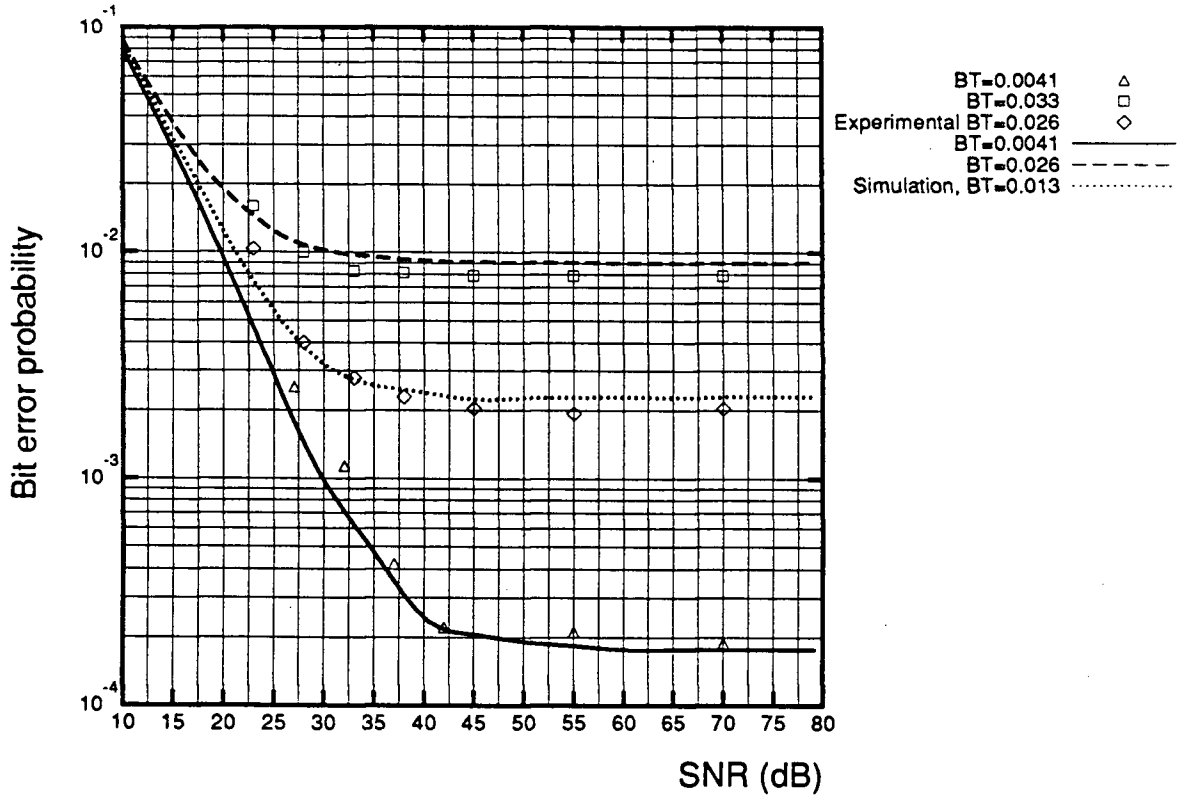

Fig. 5.18. BER of the differential detector receiver in AWGN and Rayleigh fading with $B_F T$ =0.013, 0.026 and 0.0041

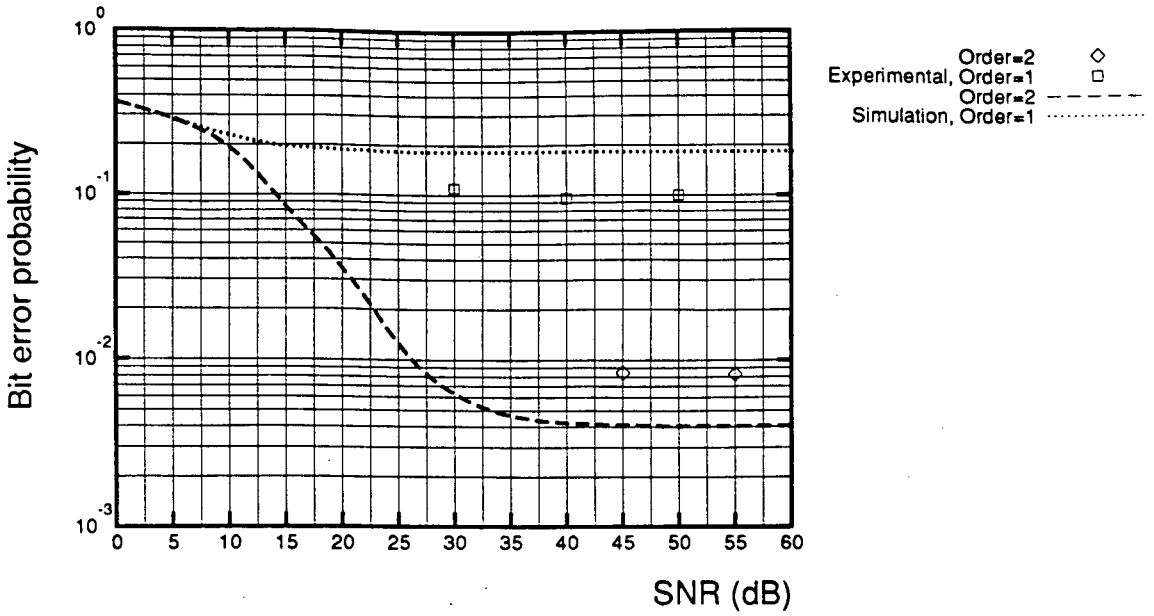

Fig. 5.19. BER of the multiple differential detector receiver in AWGN and Rayleigh fading with $B_F T = 0.125$.

Finally, some comments with reference to the processing speed of the prototype $\pi/4$–shift DPQSK system are in order. The limitation of how fast a symbol decision is made, depends upon the speed of the DSP, and the complexity of the algorithm used to make that decision. For the TMS320C30 used in our prototype system, the conventional differential detector would achieve a maximum speed of about 100 kb/s. On the other hand, the receiver with $z = 1$ would achieve approximately 2.4 kb/s, whereas the receiver with $z = 2$, 400 b/s. It should be noted that the above bit rates were achieved without any program code optimization, since the detection routines were written in the C programming language. If assembly language is used instead, it is roughly estimated that the maximum processing speed would increase by at least a factor of three.

5.5. Conclusions

The proper operation of the prototype $\pi/4$–shift DPQSK system designed and implemented in hardware/software, was verified through measurements performed on the baseband inphase and quadrature signals, as well as on the RF spectrum. BER performance data, obtained for

both a conventional differential detector and the proposed receivers, in combined AWGN and flat Rayleigh fading channel conditions, demonstrated a very good match of experimental and computer simulation results, verifying the effectiveness of the proposed technique.

6. Conclusions and Suggestions for Future Research

6.1. Conclusions

In this thesis, the problem of optimal detection of both coded and uncoded, differentially encoded or not, PSK and QAM signals in frequency nonselective Rayleigh or Ricean channels, was treated. A theoretical derivation of the maximum likelihood sequence detector for PSK and QAM signals transmitted over a fading channel, was presented. It was shown that the detector's structure can be realized as a combination of envelope, multiple differential and coherent detectors. In addition to the optimal detection algorithm, several reduced complexity algorithms were also proposed. The BER performance for these reduced complexity algorithms employing various digital modulation schemes, including coded and uncoded $\pi/4$–shift DPQSK, QPSK, $\pi/4$–shift DQAM and 8–QAM, was obtained by means of computer simulation. Finally, a hardware/software implementation of a prototype $\pi/4$–shift DPQSK modem helped verify experimentally the effectiveness of the proposed receivers.

6.2. Suggestions for Future Research

6.2.1. Further Modem Development

The prototype $\pi/4$–shift DPQSK modem designed during the course of this thesis, could be developed further, in several ways such as

- ☐ Increasing its processing speed.
- ☐ Incorporating multi-amplitude signals.
- ☐ Reducing the amount of hardware required, by using LSI/VLSI techniques.

An ultimate goal, of course, would be to commercialize the product.

6.2.2. Symbol Timing Synchronization

Throughout this thesis, it was assumed that the receiver had access to a perfect symbol timing signal. However, in practice this does not happen. Consequently, is will be very useful to investigate methods which can be employed to obtain symbol synchronization.

6.2.3. Frequency Selective Fading

Another problem which could be adopted for future research is to obtain optimal sequential receiver structures for a frequency selective fading channel.

6.2.4. CPM Signals

Finally, extension of the receiver structures presented in this thesis, in order to include continuous phase modulation (CPM) signals, would be an other interesting research topic.

Bibliography

[1] W. C. Y. Lee, *Mobile Communications Engineering*. McGraw-Hill Book Company, 1982.

[2] J. G. Proakis, *Digital Communications*. McGraw-Hill Book Company, second ed., 1989.

[3] Entire issue, "Portable and mobile communications," *IEEE J. Sel. Areas Comm.*, vol. SAC-7, Jan. 1989.

[4] Entire issue, "Special issue on fading and multipath channel communications," *IEEE J. Sel. Areas Comm.*, vol. SAC-7, Feb. 1987.

[5] W.C.Jakes, Jr., (Editor), *Microwave Mobile Communications*. New York: Wiley, 1974.

[6] L. J. Mason, "Error probability evaluation for systems employing differential detection in a ricean fast fading environment and Gaussian noise," *IEEE Trans. Comm.*, vol. COM-35, pp. 39–46, January 1987.

[7] M. Schwartz, W. R. Bennet, and S. Stein, *Communications Systems and Techniques*. New York: McGraw-Hill, 1966.

[8] A. Papoulis, *Probability, Random Variables and Stochastic Processes*. New York: McGraw-Hill Book Company, second ed., 1984.

[9] T. S. Rappaport, S. Y. Seidel, and R. Singh, "900-mhz multipath propagation measurements for U.S. digital cellular radiotelephone," *IEEE Trans. Veh. Tech.*, pp. 132–139, May 1990.

[10] D. K. Feher, *Digital Communications: Satellite/Earth Station Engineering*. Prentice Hall Inc., 1983.

[11] S. Haykin, *Digital Communications*. J. Wiley & Sons, 1988.

[12] Electronic Industry Association / Telecommunication Industry Association (EIA/TIA), "Cellular Systems: Dual Mode Mobile Station - Base Station Compatibility Standard," January 1990. Standard IS-54, Project Number 2215.

[13] K. Raith and J. Uddenfeldt, "Capacity of digital cellular TDMA systems," *IEEE Trans. Veh. Tech.*, pp. 323–332, May 1991.

[14] K. Feher, "MODEMS for emerging digital cellular-mobile radio systems," *IEEE Trans. Veh. Tech.*, pp. 355–365, May 1991.

[15] Y. Akaiwa and Y. Nagata, "Highly efficient digital mobile communications with a linear modulation method," *IEEE J. Sel. Areas Comm.*, vol. SAC-5, pp. 890–895, June 1987.

[16] S. B. Weinstein, "Telecommunications in the coming decades," *IEEE Spectrum*, pp. 62–67, Nov. 1987.

[17] D. Divsalar and M. K. Simon, "Trellis coded modulation for 4800-9600 bits/s transmission over a fading mobile satellite channel," *IEEE J. Select. Areas Comm.*, vol. SAC-5, pp. 162–175, Feb. 1987.

[18] M. K. Simon and D. Divsalar, "The performance of trellis coded multilevel DPSK on a fading mobile satellite channel," *IEEE Trans. Veh. Tech.*, vol. VT-37, pp. 78–91, May 1988.

[19] F. Edbauer, "Performance of interleaved trellis-coded differential 8-PSK modulation over fading channels," *IEEE J. Select. Areas Comm.*, vol. SAC-7, pp. 1340–1346, Dec. 1989.

[20] M. L. Moher and J. H. Lodge, "TCMP - A modulation and coding strategy for Ricean fading channels," *IEEE J. Select. Areas Comm.*, vol. SAC-7, pp. 1347–1355, Dec. 1989.

[21] D. Makrakis and P. T. Mathiopoulos, "Prediction/Cancellation techniques for fading broadcasting channels - Part I: PSK signals," *IEEE Trans. Broadcasting*, vol. BC-36, pp. 146–155, June 1990.

[22] D. Makrakis and P. T. Mathiopoulos, "Prediction/Cancellation techniques for fading broadcasting channels - Part II: CPM signals," *IEEE Trans. Broadcasting*, vol. BC-36, pp. 156–161, June 1990.

[23] F. Davarian, "Mobile digital communications via tone calibration," *IEEE Trans. Veh. Tech.*, vol. VT-36, pp. 56–61, May 1987.

[24] M. K. Simon, "Dual-pilot tone callibration technique," *IEEE Trans. Veh. Tech.*, vol. VT-35, pp. 63–70, May 1986.

[25] R. Srinivasan, "Feedback communications over fading channels," *IEEE Trans. Comm.*, vol. COM-29, pp. 50–57, Jan. 1981.

[26] S. Sampei and T. Sunara, "Rayleigh fading compensation method for 16 QAM in digital land mobile radio channels," in *the Proceedings of the 39th Vehicular Technology Conference*, (San Francisco, USA), pp. 640–646, May 1989.

[27] A. A. H. Meyr and G. Ascheid, "A new method of phase synchronization and automatic gain control of linearly modulated signals on frequency-flat fading channels," *IEEE Trans. Comm.*, vol. COM-39, pp. 25–29, Jan. 1991.

[28] P. Y. Kam and C. H. Teh, "Reception of PSK signals over fading channels via quadrature amplitude estimation," *IEEE Trans. Comm.*, vol. COM-31, pp. 1024–1027, Aug. 1983.

[29] P. Y. Kam and C. H. Teh, "An adaptive receiver with memory for slowly fading channels," *IEEE Trans. Comm.*, vol. COM-32, pp. 654–659, June 1984.

[30] R. Haeb and H. Meyr, "A systematic approach to carrier recovery and detection of digitally phase modulated signals on fading channels," *IEEE Trans. Comm.*, vol. COM-37, pp. 748–754, July 1989.

[31] S. M. Elnoubi, "Analysis of GMSK with differential detection in land mobile radio channels," *IEEE Trans. Veh. Tech.*, vol. VT-35, pp. 162–167, Nov. 1987.

[32] M. K. Simon and C. C. Wang, "Differential detection of Gaussian MSK in a mobile environment," *IEEE Trans. Veh. Tech.*, vol. VT-33, pp. 307–320, Nov. 1984.

[33] D. Makrakis et al., "A sequential decoder for differential detection of trellis coded PSK signals," in *the Proceedings of ICC '88*, (Philadelphia, USA), pp. 1433–1438, June 1988.

[34] M. K. Simon and D. Divsalar, "Doppler-corrected differential detection of MPSK," *IEEE Trans. Comm.*, vol. COM-37, pp. 99–109, Feb. 1989.

[35] S. Samejima, K. Enomoto, and Y. Watanable, "Differential PSK system with nonredundant error correction," *IEEE J. Select. Areas Comm.*, vol. SAC-1, pp. 74–81, Jan. 1983.

[36] M. Hirono, T. Miki, and K. Murota, "Multilevel decision method for band-limited digital FM with limiter-discriminator detection," *IEEE Trans. Veh. Tech.*, vol. VT-33, pp. 114–122, Feb. 1984.

[37] M. K. Simon and C. C. Wang, "Differential versus limiter-discriminator detection of narrow-band FM," *IEEE Trans. Comm.*, vol. COM-31, pp. 1227–1234, Nov. 1983.

[38] J. H. Lodge, M. L. Moher, and S. N. Crozier, "A comparison of data modulation techniques for land mobile satellite channels," *IEEE Trans. Veh. Tech.*, vol. VT-36, pp. 28–35, Feb. 1987.

[39] D. Divsalar and M. K. Simon, "Multiple-symbol differential detection of MPSK," *IEEE Trans. Comm.*, vol. COM-38, pp. 300–308, March 1990.

[40] G. Ungerboeck, "Channel coding with multilevel/phase signals," *IEEE Trans. Inform. Theory*, vol. IT-28, pp. 1188–1192, November 1986.

[41] D. R. Hummels and F. W. Ratcliffe, "Calculation of error probability for MSK and OQPSK systems operating in a fading multipath environment," *IEEE Trans. Veh. Tech.*, vol. VT-30, pp. 112–120, Aug. 1981.

[42] P. A. Bello, "Aeronautical channel characterization," *IEEE Trans. Comm.*, vol. COM-21, pp. 548–563, May 1973.

[43] S. G. Wilson, R. W. Sutton, and E. H. Schroeder, "Differential phase-shift keying performance of L-band aeronautical satellite channels: Test results and a coding evaluation," *IEEE Trans. Comm.*, vol. COM-24, pp. 374–380, Mar. 1976.

[44] Y. Miyagaki, N. Morinaga, and T. Namekawa, "Double symbol error rates of M-ary DPSK in a satellite-aircraft multipath channel," *IEEE Trans. Comm.*, vol. COM-31, pp. 1285–1289, Dec. 1983.

[45] B. D. Anderson and J. B. Moore, *Optimal Filtering*. Englewood Cliffs, NJ: Prectice-Hall, 197.

[46] D. G. Messerschmitt, "A tool for structured functional simulation," *IEEE J. Sel. Areas Comm.*, vol. SAC-2, pp. 137–147, Jan. 1984.

[47] SUN microsystems, *SunOS Reference Manual, Release 4.0, Section 3: C Library Functions, pp. 836-837*, Oct 1987.

[48] R. W. Lucky, J. Salz, and E. J. Weldon, Jr., *Principles of Data Communication.* McGraw-Hill Book Company, 1968.

[49] W. H. Press, B. P. Flannery, S. A. Teukolsky, and T. Vetterling, *Numerical Recipes in C, The Art of Scientific Computing*. Cambridge University Press, 1988.

[50] C.-L. Liu and K. Feher, "Noncoherent detection of pi/4-qpsk systems in a cci-awgn combined interference environment," in *the Proceedings of the 39th Vehicular Technology Conference*, pp. 83–94, May 1989.

[51] S. D. Conte and C. de Boor, *Elementary Numerical Analysis, An Algorithmic Approach.* McGraw-Hill Book Company, third ed., 1981.

[52] M. C. Jeruchim, "Techniques for estimating the bit error rate in the simulation of digital communication systems," *IEEE J. Sel. Areas Comm.*, vol. SAC-2, pp. 153–170, Jan. 1984.

[53] Y. Yamao, S. Saito, H. Suzuki, and T. Nojima, "Performance of pi/4-qpsk transmission for digital mobile radio applications," in *the Proceedings of GLOBECOM '89*, pp. 443–447, November 1989.

[54] C.-L. Liu and K. Feher, "Performance of non-coherent pi/4-qpsk in a frequency-selective fast rayleigh fading channel," in *the Proceedings of SUPERCOM/ICC 90, Atlanta GA*, pp. 335.7.1–335.7.5, April 1990.

[55] C. A. Siller, W. Debus, and T. L. Osborne, "Spectral shaping and digital synthesis of an M-ary time series," *IEEE Comm. Mag.*, pp. 15–24, Feb. 1989.

[56] E. Casas and C. Leung, "A simple digital fading simulator for mobile radio," *IEEE Trans. Veh. Tech.*, pp. 205–212, Aug. 1990.

[57] SPECTRUM Signal Processing Inc., *The TMS320C30 System Board Technical Reference Manual, Issue 1.0*, May 1990.

[58] Mini-Circuits, *RF/IF signal processing guide*. SF-89/90.

Appendix A. Theoretical Derivations

A.1. Derivation of Equation 2.18.

For the reader's convenience, we rewrite Eq. 2.15

$$e_k^I = f_k^I + n_k^I = \frac{\mathrm{Re}\left(y_k c_k^* e^{-j\rho}\right)}{|c_k|^2} \; ; \quad e_k^Q = f_k^Q + n_k^Q = \frac{\mathrm{Im}\left(y_k c_k^* e^{-j\rho}\right)}{|c_k|^2} \; . \tag{A.1}$$

The autocorrelation matrix terms are then given by

$$R_e\left[\overline{C}(\overline{a}), (k-i)T\right] = E\left\{e_k^I e_i^I\right\} = E\left\{e_k^Q e_i^Q\right\} \; . \tag{A.2}$$

Since fading and white Gaussian noise are assumed to be independent, substituting Eq. A.1 into the above equation, we obtain:

$$R_e\left[\overline{C}(\overline{a}), (k-i)T\right] = R_f(k-i) + E\left\{n_e^I(k) n_e^I(i)\right\} \; . \tag{A.3}$$

By using Eq. 2.16 and 2.17, i.e.,

$$n_e^I(k) = \frac{n_s(kT)\mathrm{Re}\left(c_k^* e^{-j\rho}\right) + n_c(kT)\mathrm{Im}\left(c_k^* e^{-j\rho}\right)}{|c_k|^2} \tag{A.4}$$

and

$$n_e^Q(k) = \frac{n_s(kT)\mathrm{Im}\left(c_k^* e^{-j\rho}\right) - n_c(kT)\mathrm{Re}\left(c_k^* e^{-j\rho}\right)}{|c_k|^2} \; . \tag{A.5}$$

and substituting in the $E\{n_e^I(k) n_e^I(i)\}$ term of Eq. A.3, we get

$$E\left\{n_e^I(k) n_e^I(i)\right\} = E\left\{\left[\frac{n_s(kT)\mathrm{Re}\left(c_k^* e^{-j\rho}\right)}{|c_k|^2} + \frac{n_c(kT)\mathrm{Im}\left(c_k^* e^{-j\rho}\right)}{|c_k|^2}\right]\left[\frac{n_s(iT)\mathrm{Re}\left(c_i^* e^{-j\rho}\right)}{|c_i|^2} + \frac{n_c(iT)\mathrm{Im}\left(c_i^* e^{-j\rho}\right)}{|c_i|^2}\right]\right\} . \tag{A.6}$$

Since $n_c(kT)$ and $n_s(kT)$ are uncorrelated, the expected value of all cross-product terms is zero. Hence, from the remaining terms

$$E\left\{n_e^I(k) n_e^I(i)\right\} = E\left\{\frac{n_s(kT)\mathrm{Re}\left(c_k^* e^{-j\rho}\right) n_s(iT)\mathrm{Re}\left(c_i^* e^{-j\rho}\right)}{|c_k|^2 |c_i|^2} + \frac{n_c(kT)\mathrm{Im}\left(c_k^* e^{-j\rho}\right) n_c(iT)\mathrm{Im}\left(c_i^* e^{-j\rho}\right)}{|c_k|^2 |c_i|^2}\right\} . \tag{A.7}$$

Since the power of the Gaussian noise at the output of the receive filter $H_R(f)$ is equal to

$$\sigma_G^2 = \frac{N_0}{2T_s} \tag{A.8}$$

Equation A.7 becomes

$$\sigma_G^2 \delta(k-i) E\left\{ \frac{\mathrm{Re}(c_k^* c_i)}{|c_k|^2 |c_i|^2} \right\} \tag{A.9}$$

where $\delta(\cdot)$ is the Kronecker delta function, nonzero only for $k = i$. Combining Eq. A.3 and A.9 we get

$$E\left\{e_k^I e_i^I\right\} = E\left\{e_k^Q e_i^Q\right\} = R_f(k-i) + \frac{\sigma_G^2 \delta(k-i)}{|c_k|^2} \ . \tag{A.10}$$

which is Eq. 2.18.

A.2. Derivation of Equation 2.27.

The general form of the metric as presented in Eq. 2.23, is given by the function

$$\frac{1}{2}\sum_{k=1}^{L} \frac{1}{\sigma_k^2} \left\{ \begin{array}{c} \left[\frac{\mathrm{Re}\{y_k c_k^* e^{-j\rho}\}}{|c_k|^2} - \sum_{i=1}^{k} p_{k,i} \frac{\mathrm{Re}\{y_{k-i} c_{k-i}^* e^{-j\rho}\}}{|c_{k-i}|^2} - \overline{f^I}\left(1 - \sum_{i=1}^{k} p_{k,i}\right) \right]^2 + \\ \left[\frac{\mathrm{Im}\{y_k c_k^* e^{-j\rho}\}}{|c_k|^2} - \sum_{i=1}^{k} p_{k,i} \frac{\mathrm{Im}\{y_{k-i} c_{k-i}^* e^{-j\rho}\}}{|c_{k-i}|^2} \right]^2 \end{array} \right\} \tag{A.11}$$

For simplification of the symbolism, the dependence of the prediction coefficients and the MMSPE on the transmitted sequence, has been dropped. By defining $p_{k,0} = -1 \ \forall k, \ 0 \le k \le L$, the above equation becomes

$$\frac{1}{2}\sum_{k=1}^{L} \frac{1}{\sigma_k^2} \left\{ \begin{array}{c} \left[- \sum_{i=0}^{k} p_{k,i} \frac{\mathrm{Re}\{y_{k-i} c_{k-i}^* e^{-j\rho}\}}{|c_{k-i}|^2} - \overline{f^I} \sum_{i=0}^{k} p_{k,i} \right]^2 + \\ \left[- \sum_{i=0}^{k} p_{k,i} \frac{\mathrm{Im}\{y_{k-i} c_{k-i}^* e^{-j\rho}\}}{|c_{k-i}|^2} \right]^2 \end{array} \right\} \tag{A.12}$$

The first squared term in Eq. A.12 can be expanded as

$$\left[- \sum_{i=0}^{k} \frac{\mathrm{Re}\{y_k c_k^* e^{-j\rho}\}}{|c_k|^2} - \overline{f^I} \sum_{i=0}^{k} p_{k,i} \right]^2 =$$

$$\left(\overline{f^I} \sum_{i=0}^{k} p_{k,i} \right)^2 + 2\overline{f^I} \sum_{l=0}^{k} p_{k,l} \sum_{i=0}^{k} p_{k,i} \frac{\mathrm{Re}\{y_{k-i} c_{k-i}^* e^{-j\rho}\}}{|c_k|^2} + \left(\sum_{i=0}^{k} p_{k,i} \frac{\mathrm{Re}\{y_{k-i} c_{k-i}^* e^{-j\rho}\}}{|c_k|^2} \right)^2 . \tag{A.13}$$

The third term of Eq. A.13 can be combined with the second squared term within the brackets of Eq. A.12 to yield the following

$$\left[\sum_{i=0}^{k} p_{k,i}\frac{\mathrm{Re}\{y_{k-i}c_{k-i}^{*}e^{-j\rho}\}}{|c_{k-i}|^{2}}\right]^{2}+\left[\sum_{i=0}^{k} p_{k,i}\frac{\mathrm{Im}\{y_{k-i}c_{k-i}^{*}e^{-j\rho}\}}{|c_{k-i}|^{2}}\right]^{2}=$$
$$\sum_{i=0}^{k} p_{k,i}^{2}\frac{\left(\mathrm{Re}\{y_{k-i}c_{k-i}^{*}e^{-j\rho}\}\right)^{2}}{|c_{k-i}|^{4}}+\sum_{i=0}^{k}\sum_{\substack{l=0\\ i\neq l}}^{k} p_{k,i}p_{k,l}\frac{\mathrm{Re}\{y_{k-i}c_{k-i}^{*}e^{-j\rho}\}\mathrm{Re}\{y_{k-l}c_{k-l}^{*}e^{-j\rho}\}}{|c_{k-i}|^{2}|c_{k-l}|^{2}}+$$
$$\sum_{i=0}^{k} p_{k,i}^{2}\frac{\left(\mathrm{Im}\{y_{k-i}c_{k-i}^{*}e^{-j\rho}\}\right)^{2}}{|c_{k-i}|^{4}}+\sum_{i=0}^{k}\sum_{\substack{l=0\\ i\neq l}}^{k} p_{k,i}p_{k,l}\frac{\mathrm{Im}\{y_{k-i}c_{k-i}^{*}e^{-j\rho}\}\mathrm{Im}\{y_{k-l}c_{k-l}^{*}e^{-j\rho}\}}{|c_{k-i}|^{2}|c_{k-l}|^{2}}. \tag{A.14}$$

The first and third term of Eq. A.14, can be combined to yield

$$\sum_{i=0}^{k} p_{k,i}^{2}\frac{\left|y_{k-i}c_{k-i}^{*}e^{-j\rho}\right|^{2}}{|c_{k-i}|^{4}}=\sum_{i=0}^{k} p_{k,i}^{2}\frac{|y_{k-i}|^{2}}{|c_{k-i}|^{2}} \tag{A.15}$$

while the addition of the second and fourth term, by using the identity $\mathrm{Re}(AB^{*}) = \mathrm{Re}(A)\mathrm{Re}(B)+\mathrm{Im}(A)\mathrm{Im}(B)$, leads to the expression

$$\sum_{i=0}^{k}\sum_{\substack{l=0\\ i\neq l}}^{k} p_{k,i}p_{k,l}\frac{\mathrm{Re}\{y_{k-i}c_{k-i}^{*}e^{-j\rho}y_{k-l}^{*}c_{k-l}e^{j\rho}\}}{|c_{k-i}|^{2}|c_{k-l}|^{2}}=$$
$$\sum_{i=0}^{k}\sum_{\substack{l=0\\ i\neq l}}^{k} p_{k,i}p_{k,l}\frac{\mathrm{Re}\{y_{k-i}y_{k-l}^{*}\}\mathrm{Re}\{c_{k-i}c_{k-l}^{*}\}+\mathrm{Im}\{y_{k-i}y_{k-l}^{*}\}\mathrm{Im}\{c_{k-i}c_{k-l}^{*}\}}{|c_{k-i}|^{2}|c_{k-l}|^{2}}. \tag{A.16}$$

By combining the intermediate results, Eq. A.12 can be rewritten as

$$\frac{1}{2}\sum_{k=1}^{L}\frac{1}{\sigma_{k}^{2}}\left\{\begin{array}{l}\left(\overline{f^{I}}\sum_{i=0}^{k} p_{k,i}\right)^{2}+2\overline{f^{I}}\sum_{i=0}^{k} p_{k,i}\sum_{l=0}^{k} p_{k,l}\frac{\mathrm{Re}\{y_{k-i}c_{k-l}^{*}e^{-j\rho}\}}{|c_{k-l}|^{2}}+\sum_{i=0}^{k} p_{k,i}^{2}\frac{|y_{k-i}|^{2}}{|c_{k-i}|^{2}}+\\ \sum_{i=0}^{k}\sum_{\substack{l=0\\ i\neq l}}^{k} p_{k,i}p_{k,l}\frac{\mathrm{Re}\{y_{k-i}y_{k-l}^{*}\}\mathrm{Re}\{c_{k-i}c_{k-l}^{*}\}+\mathrm{Im}\{y_{k-i}y_{k-l}^{*}\}\mathrm{Im}\{c_{k-i}c_{k-l}^{*}\}}{|c_{k-i}|^{2}|c_{k-l}|^{2}}\end{array}\right\}. \tag{A.17}$$

Equation A.17 can be simplified further and for this purpose it is split up to four terms

$$\mathbf{T_1} = \sum_{k=1}^{L} \frac{1}{\sigma_k^2} \sum_{i=0}^{k} \sum_{\substack{l=0 \\ i \neq l}}^{k} p_{k,i} p_{k,l} \frac{\mathrm{Re}\{y_{k-i} y_{k-l}^*\}\mathrm{Re}\{c_{k-i} c_{k-l}^*\} + \mathrm{Im}\{y_{k-i} y_{k-l}^*\}\mathrm{Im}\{c_{k-i} c_{k-l}^*\}}{|c_{k-i}|^2 |c_{k-l}|^2}$$

$$\mathbf{T_2} = \sum_{k=1}^{L} \frac{1}{\sigma_k^2} \sum_{i=0}^{k} p_{k,i}^2 \frac{|y_{k-i}|^2}{|c_{k-i}|^2}$$

$$\mathbf{T_3} = \sum_{k=1}^{L} \frac{1}{\sigma_k^2} 2\overline{f^I} \sum_{j=0}^{k} p_{k,j} \sum_{i=0}^{k} p_{k,i} \frac{\mathrm{Re}\{y_{k-i} c_{k-i}^* e^{-j\rho}\}}{|c_{k-i}|^2}$$

$$\mathbf{T_4} = \sum_{k=1}^{L} \frac{1}{\sigma_k^2} \left(\overline{f^I} \sum_{i=0}^{k} p_{k,i} \right)^2 . \tag{A.18}$$

The 1/2 factor was dropped since it is only a scaling factor. Observing term $\mathbf{T_1}$, it is clear that (i, l) combinations appear in pairs that can be lumped together if the following identity is used

$$\begin{aligned} &\mathrm{Re}(A)\mathrm{Re}(B) + \mathrm{Im}(A)\mathrm{Im}(B) + \mathrm{Re}(A^*)\mathrm{Re}(B^*) + \mathrm{Im}(A^*)\mathrm{Im}(B^*) = \\ &= 2\{\mathrm{Re}(A)\mathrm{Re}(B) + \mathrm{Im}(A)\mathrm{Im}(B)\} . \end{aligned} \tag{A.19}$$

This transforms $\mathbf{T_1}$ to

$$\mathbf{T_1} = \sum_{k=1}^{L} \frac{2}{\sigma_k^2} \sum_{i=0}^{k} \sum_{j=i+1}^{k} p_{k,i} p_{k,l} \frac{\mathrm{Re}\left\{y_{k-i} y_{k-j}^*\right\}\mathrm{Re}\left\{c_{k-i} c_{k-j}^*\right\} + \mathrm{Im}\left\{y_{k-i} y_{k-j}^*\right\}\mathrm{Im}\left\{c_{k-i} c_{k-j}^*\right\}}{|c_{k-i}|^2 |c_{k-j}|^2} . \tag{A.20}$$

By writing out in more detail the sum in the expression for $\mathbf{T_1}$, it is fairly clear to see that the individual terms can be grouped in a different way, that is, with respect to combinations of

the form $(y_k y_{k-i}^*)$. By rewriting $\mathbf{T_1}$ as[12]

$$\mathbf{T_1} = \sum_{k=1}^{L} \frac{2}{\sigma_k^2} \sum_{i=1}^{k} \sum_{j=i+1}^{k} p_{k,i} p_{k,l} \frac{\mathrm{Re}\{y_{k-i} y_{k-j}^*\}\mathrm{Re}\{c_{k-i} c_{k-j}^*\} + \mathrm{Im}\{y_{k-i} y_{k-j}^*\}\mathrm{Im}\{c_{k-i} c_{k-j}^*\}}{|c_{k-i}|^2 |c_{k-j}|^2} =$$

$$= \frac{2}{\sigma_1^2}\{p_{10} p_{11} \mathfrak{P}_{10}\}$$

$$+ \frac{2}{\sigma_2^2}\{p_{20} p_{21} \mathfrak{P}_{21} + p_{20} p_{21} \mathfrak{P}_{20} + p_{21} p_{22} \mathfrak{P}_{10}\}$$

$$+ \frac{2}{\sigma_3^2}\{p_{30} p_{31} \mathfrak{P}_{32} + p_{30} p_{32} \mathfrak{P}_{31} + p_{30} p_{33} \mathfrak{P}_{30} + p_{31} p_{32} \mathfrak{P}_{21} + p_{31} p_{33} \mathfrak{P}_{20} + p_{32} p_{33} \mathfrak{P}_{10}\} \tag{A.21}$$

$$\vdots$$

$$+ \frac{2}{\sigma_L^2} \left\{ \begin{array}{c} (p_{L0} p_{L1} \mathfrak{P}_{L,L-1} + \cdots + p_{L0} p_{LL} \mathfrak{P}_{L0}) \\ +(p_{L1} p_{L2} \mathfrak{P}_{L-1,L-2} + \cdots + p_{L1} p_{LL} \mathfrak{P}_{L-2,0}) \\ \vdots \\ +(p_{L,L-1} p_{L,L} \mathfrak{P}_{10}) \end{array} \right\}$$

with

$$\mathfrak{P}_{ij} = \frac{\mathrm{Re}\left(y_i y_j^*\right)\mathrm{Re}\left(c_i c_j^*\right) + \mathrm{Im}\left(y_i y_j^*\right)\mathrm{Im}\left(c_i c_j^*\right)}{|c_i|^2 |c_j|^2} \tag{A.22}$$

and grouping with respect to the $\mathfrak{P}_{ij}$ terms, the expression for $\mathbf{T_1}$ becomes

$$\mathbf{T_1} = 2 \sum_{k=1}^{L} \sum_{i=1}^{k} \frac{\mathrm{Re}\{y_k y_{k-i}^*\}\mathrm{Re}\{c_k c_{k-i}^*\} + \mathrm{Im}\{y_k y_{k-i}^*\}\mathrm{Im}\{c_k c_{k-i}^*\}}{|c_k|^2 |c_{k-i}|^2} \sum_{j=0}^{L-k} \frac{p_{k+j,j} p_{k+j,i+j}}{\sigma_{k+j}^2} . \tag{A.23}$$

The same type of term re-grouping can be applied to the expressions for $\mathbf{T_2}$ and $\mathbf{T_3}$. Expanding the expression for $\mathbf{T_2}$, we obtain

$$\mathbf{T_2} = \sum_{k=1}^{L} \frac{1}{\sigma_k^2} \sum_{i=0}^{k} p_{k,i}^2 \frac{|y_{k-i}|^2}{|c_{k-i}|^2} =$$

$$\frac{1}{\sigma_1^2}\left\{ p_{10}^2 \frac{|y_1|^2}{|c_1|^2} + p_{11}^2 \frac{|y_0|^2}{|c_0|^2} \right\}$$

$$+ \frac{1}{\sigma_2^2}\left\{ p_{20}^2 \frac{|y_2|^2}{|c_2|^2} + p_{21}^2 \frac{|y_1|^2}{|c_1|^2} + p_{22}^2 \frac{|y_0|^2}{|c_0|^2} \right\} \tag{A.24}$$

$$+ \frac{1}{\sigma_3^2}\left\{ p_{30}^2 \frac{|y_3|^2}{|c_3|^2} + p_{31}^2 \frac{|y_2|^2}{|c_2|^2} + p_{32}^2 \frac{|y_1|^2}{|c_1|^2} + p_{33}^2 \frac{|y_0|^2}{|c_0|^2} \right\}$$

$$\vdots$$

$$+ \frac{1}{\sigma_L^2}\left\{ p_{L0}^2 \frac{|y_L|^2}{|c_L|^2} + p_{L1}^2 \frac{|y_{L-1}|^2}{|c_{L-1}|^2} + \cdots + p_{LL}^2 \frac{|y_0|^2}{|c_0|^2} \right\}$$

[12] From this point and on, commas between subscripts will be omitted whenever appropriate, for clarity purposes.

which becomes the following, when grouping with respect to the $|y_i|^2/|c_i|^2$ terms, is applied:

$$\mathbf{T_2} = \sum_{k=1}^{L} \frac{|y_k|^2}{|c_k|^2} \sum_{i=0}^{L-k} \frac{p_{k+i,i}^2}{\sigma_{k+i}^2} \,. \tag{A.25}$$

For $\mathbf{T_3}$, expanding yields

$$\begin{aligned}
\mathbf{T_3} &= \sum_{k=1}^{L} \frac{2\overline{fI}}{\sigma_k^2} \sum_{j=0}^{k} p_{k,j} \sum_{i=0}^{k} p_{k,i} \frac{\mathrm{Re}\{y_{k-i} c_{k-i}^* e^{-j\rho}\}}{|c_{k-i}|^2} = \\
&= \frac{1}{\sigma_1^2}\Big\{\Big(p_{10}\Omega_1 + p_{11}\Omega_0\Big)(p_{10}+p_{11})\Big\} \\
&+ \frac{1}{\sigma_2^2}\Big\{\Big(p_{20}\Omega_2 + p_{21}\Omega_1 + +p_{20}\Omega_0\Big)(p_{20}+p_{21}+p_{22})\Big\} \\
&+ \frac{1}{\sigma_3^2}\Big\{\Big(p_{30}\Omega_3 + p_{31}\Omega_2 + p_{32}\Omega_1 + p_{33}\Omega_0\Big)(p_{30}+p_{31}+p_{32}+p_{33})\Big\} \\
&\vdots \\
&+ \frac{1}{\sigma_L^2}\Big\{\Big(p_{L0}\Omega_L + p_{L1}\Omega_{L-1} + \cdots + p_{LL}\Omega_0\Big)(p_{L0}+p_{L1}+\cdots+p_{LL})\Big\}
\end{aligned} \tag{A.26}$$

where

$$\Omega_i = \frac{\mathrm{Re}(y_i c_i^* e^{-j\rho})}{|c_i|^2} \tag{A.27}$$

and grouping with respect to the Ω_i terms, results to the final expression for $\mathbf{T_3}$, which is the following

$$\mathbf{T_3} = 2\overline{fI} \sum_{k=1}^{L} \frac{\mathrm{Re}(y_k c_k^* e^{-j\rho})}{|c_k|^2} \sum_{i=0}^{L-k} \frac{p_{k+i,i}}{\sigma_{k+i}^2} \sum_{j=0}^{k+i} p_{k+i,j} \,. \tag{A.28}$$

The fourth term, namely $\mathbf{T_4}$, does not depend on the information sequence transmitted and therefore it can be eliminated from the metric calculation process. Combining terms $\mathbf{T_1}$, $\mathbf{T_2}$ and $\mathbf{T_3}$, we arrive at Eq. 2.27.

A.3. Derivation of Equation 2.28.

The incremental metrics for the recursive implementation of the algorithm, can be obtained by inspection, from the expanded forms of $\mathbf{T_1}$ through $\mathbf{T_3}$. From every line in Eq. A.21, A.24 and A.26, only the terms for which, the second digit of the prediction coefficient subscript is

not greater than the maximum prediction order, are kept. The first digit is changed for all to the maximum prediction order. This essentially corresponds to having a *sliding prediction window* of size $z+1$. Furthermore, the MMSPE used is always σ_z^2. For example, for a maximum prediction order of $z=2$, the expanded form of the sum for $\mathbf{T_2}$ is modified as

$$\begin{aligned}
&\frac{1}{\sigma_2^2}\left\{p_{20}^2\frac{|y_3|^2}{|c_3|^2}+p_{21}^2\frac{|y_2|^2}{|c_2|^2}+p_{22}^2\frac{|y_1|^2}{|c_1|^2}\right\}\\
&+\frac{1}{\sigma_2^2}\left\{p_{20}^2\frac{|y_4|^2}{|c_4|^2}+p_{21}^2\frac{|y_3|^2}{|c_3|^2}+p_{22}^2\frac{|y_2|^2}{|c_2|^2}\right\}\\
&+\frac{1}{\sigma_2^2}\left\{p_{20}^2\frac{|y_5|^2}{|c_5|^2}+p_{21}^2\frac{|y_4|^2}{|c_4|^2}+p_{22}^2\frac{|y_3|^2}{|c_3|^2}\right\}\\
&\vdots\\
&+\frac{1}{\sigma_2^2}\left\{p_{20}^2\frac{|y_L|^2}{|c_L|^2}+p_{21}^2\frac{|y_{L-1}|^2}{|c_{L-1}|^2}+p_{22}^2\frac{|y_{L-2}|^2}{|c_{L-2}|^2}\right\}.
\end{aligned} \tag{A.29}$$

Notice that each term in Eq. A.29 includes the $z+1$ most recent signal samples only, and no terms for samples before y_3, since the algorithm is assumed to have been initialized by z samples prior to normal operation. By inspection, it is not difficult to realize that the incremental metric for $\mathbf{T_2}$, i.e., $\Delta\mathbf{T_2}$, is

$$\Delta\mathbf{T_2}=\frac{1}{\sigma_z^2}\frac{|y_k|^2}{|c_k|^2}\sum_{i=0}^{m}p_{z,i}^2 \tag{A.30}$$

where

$$m=\begin{cases} z, & k\le L-z\\ L-k, & k>L-z\,. \end{cases} \tag{A.31}$$

Similar observations lead to the incremental forms for $\mathbf{T_1}$ and $\mathbf{T_3}$, i.e., $\Delta\mathbf{T_1}$ and $\Delta\mathbf{T_3}$ respectively:

$$\begin{aligned}
\Delta\mathbf{T_1}&=\sum_{i=1}^{z}\frac{\mathrm{Re}(y_k y_{k-i}^*)\mathrm{Re}(c_k c_{k-i}^*)+\mathrm{Im}(y_k y_{k-i}^*)\mathrm{Im}(c_k c_{k-i}^*)}{|c_k|^2|c_{k-i}|^2}\sum_{j=0}^{z-i}\frac{p_{z,i}p_{z,i+j}}{\sigma_z^2}\\
\Delta\mathbf{T_3}&=2\overline{f^I}\frac{\mathrm{Re}(y_k c_k^* e^{-j\rho})}{|c_k|^2}\sum_{i=0}^{m}\frac{p_{z,i}}{\sigma_z^2}\sum_{j=0}^{z}p_{z,j}\,.
\end{aligned} \tag{A.32}$$

The summation limit m given by Eq. A.31, applies only to transmission of information blocks having a finite length L. However, for sequential decoders performing metric computation after every new sample input, m is always equal to z. Finally, by combining the expressions for all incremental terms, we get the complete incremental metric

$$\Delta\Xi^{F}_{(\overline{y},\overline{C}(\overline{a}),\rho)} = 2\sum_{i=1}^{z} \frac{\mathrm{Re}(y_k y^*_{k-i})\mathrm{Re}(c_k c^*_{k-i}) + \mathrm{Im}(y_k y^*_{k-i})\mathrm{Im}(c_k c^*_{k-i})}{|c_k|^2 |c_{k-i}|^2} \mathrm{B}_{z,i}\left[\overline{C}(\overline{a})\right] + \\ + \frac{|y_k|^2}{|c_k|^2}\mathbf{\Gamma}_{z,k}\left[\overline{C}(\overline{a})\right] + \frac{\mathrm{Re}(y_k c^*_k e^{-j\rho})}{|c_k|^2}\mathbf{\Delta}_{z,k}\left[\overline{C}(\overline{a})\right] \tag{A.33}$$

with

$$\mathbf{B}_{z,i} = \sum_{j=0}^{z-i} \frac{p_{z,i}\left[\overline{C}(\overline{a})\right] p_{z,i+j}\left[\overline{C}(\overline{a})\right]}{\sigma_z^2\left[\overline{C}(\overline{a})\right]}$$

$$\mathbf{\Gamma}_{z,i} = \frac{1}{\sigma_z^2\left[\overline{C}(\overline{a})\right]} \sum_{j=0}^{m} p_{z,j}^2\left[\overline{C}(\overline{a})\right] \tag{A.34}$$

$$\mathbf{\Delta}_{z,i} = \frac{2\overline{f}^I}{\sigma_z^2\left[\overline{C}(\overline{a})\right]} \sum_{j=0}^{m} p_{z,j}\left[\overline{C}(\overline{a})\right] \sum_{l=0}^{z} p_{z,l}\left[\overline{C}(\overline{a})\right]$$

and $m = \begin{cases} z, & k \le L - z \\ L - k, & k > L - z \end{cases}$.

A.4. Derivation of Equation 3.11.

Following [5], it can be assumed that the diffusive behavior of the land-mobile radio channel is adequately modelled by the following function:

$$s'(t) = R(t) A_i \cos\left(\omega_c t - \phi_i - \theta(t)\right) \tag{A.35}$$

where $s'(t)$ represents the received signal, $R(t)$ the Rayleigh faded carrier envelope, A_i an information amplitude signal, ω_c the carrier radian frequency, ϕ_i the information bearing phase and $\theta(t)$ the random phase due to fading. This phase $\theta(t)$ is assumed to be uniformly distributed in [-π,π). Using trigonometric identities, $s'(t)$ can be manipulated as follows

$$\begin{aligned} s'(t) &= R(t) A_i [\cos\theta(t)\cos\left(\omega_c t - \phi_i\right) + \sin\theta(t)\sin\left(\omega_c t - \phi_i\right)] \\ &= A_i \left[f^I(t)\cos\left(\omega_c t - \phi_i\right) + f^Q(t)\sin\left(\omega_c t - \phi_i\right) \right] \end{aligned} \tag{A.36}$$

where $f^I(t) = R(t)\cos\theta(t)$ and $f^Q(t) = R(t)\sin\theta(t)$. Furthermore

$$\begin{aligned} s'(t) &= A_i\{(f^I(t)\cos\omega_c t\cos\phi_i + f^I(t)\sin\omega_c t\sin\phi_i) + (f^Q(t)\sin\omega_c t\cos\phi_i - f^Q(t)\cos\omega_c t\sin\phi_i)\} \\ &= A_i\{(f^I(t)\cos\phi_i - f^Q(t)\sin\phi_i)\cos\omega_c t + (f^I(t)\sin\phi_i + f^Q(t)\cos\phi_i)\sin\omega_c t\} \ . \end{aligned} \tag{A.37}$$

The baseband equivalent of $s'(t)$ is [2]

$$\begin{aligned} u'(t) &= A_i\Big[\Big(f^I(t)\cos\phi_i - f^Q(t)\sin\phi_i\Big) + j\Big(f^I(t)\sin\phi_i + f^Q(t)\cos\phi_i\Big)\Big] \\ &= \Big(f^I(t) + jf^Q(t)\Big)A_i(\cos\phi_i + j\sin\phi_i) \quad . \end{aligned} \tag{A.38}$$

But the term $A_i(\cos\phi_i + j\sin\phi_i)$ is the baseband equivalent of the modulated carrier while $f^I(t) + jf^Q(t)$ is the complex fading process generated by filtering with identical fading filters two independent Gaussian noise sources (see Fig. 3.9).

A.5. Derivation of Equation 3.15.

Assuming that an envelope (amplitude) limiter normalizes the signal amplitude to one, we would like to derive an expression for the derivative of the carrier phase $\phi(t)$, as a function of the inphase $(x(t))$ and quadrature $(y(t))$ signals.

Since $\tan[\phi(t)] = y(t)/x(t)$, taking the first derivative we get

$$\frac{\partial}{\partial t}\tan[\phi(t)] = \frac{1}{x^2(t)}\left[x(t)\frac{\partial y(t)}{\partial t} - y(t)\frac{\partial x(t)}{\partial t}\right] . \tag{A.39}$$

From the above equation, and since

$$\frac{\partial}{\partial t}\tan[\phi(t)] = \sec^2[\phi(t)]\frac{\partial\phi(t)}{\partial t} = \frac{1}{x^2(t)}\frac{\partial\phi(t)}{\partial t} \tag{A.40}$$

Eq. 3.15 follows.